Melting temperatures of the noble gases from ab-initio Monte Carlo simulations

A thesis presented in partial fulfilment of the
requirements for the degree of

Doctor of Philosophy
in
Physics

at
Massey University, Albany
New Zealand

Odile R. Smits

2019

Abstract

This thesis describes simulations to determine the melting temperatures of the noble gases based on first-principles ab-initio methods.
The melting temperatures of bulk krypton, xenon, radon and oganesson are determined using parallel-tempering Monte Carlo with the interaction potential approximated by two- and three-body contributions. The employed interaction potentials are obtained from relativistic coupled cluster theory including spin-orbit coupling and are the most accurate ab-initio potentials to this date. These potentials are fitted to computationally efficient functions utilized to calculate the interaction energy during the Monte Carlo melting simulation. Two different techniques of obtaining the melting temperature are presented.
First, the melting temperature is studied by simulating finite clusters in a canonical ensemble. The melting temperature is then deducted from extrapolation of the finite cluster results to the bulk.
Second, the melting temperature is determined by direct sampling of the bulk using cells with periodic boundary conditions in the isobaric-isothermal ensemble. Upon correction for superheating, an excellent agreement to the melting temperatures obtained from cluster simulations is obtained.
The numerically determined melting temperatures of krypton and xenon are in close agreement with available experimental data. That is, for krypton a melting temperature of 109.5 K and 111.7 K is obtained for cluster and periodic simulations respectively, which is approximately 5 Kelvin lower than the corresponding experimental value of 115.78 K. The melting point of xenon is determined to be 156.1 K and 161.6 K respectively, which compares to the experimental value of 161.40 K. The long debated value of the radon melting temperature of 202 K is confirmed by our simulations (200 K for both techniques). And finally, the melting point of oganesson is determined to be 330 K and therefore surprisingly high compared to the other rare gases. This implies that oganesson is a solid at room temperature.
Furthermore, an analytical formula to compute the temperature of the solid-liquid phase transition based on the analytically expressed bulk modulus and interaction potential is presented, and the superheating correction factor is evaluated.

Acknowledgements

First and foremost, I thank my supervisor Peter for his expert advice, encouraging words and fruitful discussions. It was a pleasure to work with you and I am grateful for the knowledge you have taught me and the many opportunities that were created.

I would also like to thank my co-supervisor Elke for her support during my Ph.D studies and the interesting discussions we had.

I thank my colleagues Luke, Lukas, Morten, Paul, Peter, Jan, Steffi, Krista, Edison, Antony and Ray. Paul, I enjoyed our collaboration on the study of the heavy elements and I thank you for your patience when explaining the concepts of ab-initio calculations. The ab-initio calculations you performed, provide the first building block of the study on the melting temperatures of the noble gases. Without you, this work would not have been possible. Morten, Peter and Jan, I am so happy you started surfing and I am looking forward to the 'work meetings' we will have in Te Arai. Luke and Anthony, thank you for the many fun and interesting conversations.

I am forever grateful to my dear parents, Henkie and Paula. I am incredibly lucky to have parents like you, who give me endless support and always show interest in the research I carry out. You both have encouraged me to become a scientist and although I am not a 'boekenpakster' I think some days I am quite close.

And last but not least, I would like to thank the guy with the biggest heart, Steve, who has been there for me day and night and who has supported and cared for me in a thousand different ways.

Contents

List of Figures

List of Tables

1. Introduction

The recent successful synthesis of the heaviest member of the noble gases, oganesson, has caused a spark of interest in the chemical and physical studies of superheavy elements. The group to which it belongs, the noble gases, are found in the far right row of the periodic table, and each of these atoms have a completely filled outer shell of valence electrons. As a result, the noble gases are the least chemically reactive of all the elements and are found in their gaseous state at ambient conditions. Nonetheless, their small, but non-negligible induced dipole moments gives rise to small dispersive type of interactions and upon cooling (or under pressure), these elements make the transition to the liquid and finally the solid phase.

Experimentally, the melting and boiling temperatures have been obtained for helium, neon, argon, krypton, xenon and radon, which are depicted in Fig. 1.1, with in blue the melting and in red the boiling temperatures. Besides the increase in melting and boiling temperature with atomic number, it is also noticeable that the melting and boiling temperatures are very close together. Whereas for the lighter noble gases the melting temperature can relatively easy be obtained by experiment, measurements on the melting temperature of radon were experimentally very challenging as radon is highly radioactive and thus measurements were therefore only done in the early years after its discovery [1].

Oganesson joined the periodic table in 2002 [3–6] together with a group of other exotic superheavy elements. As each of these are very short lived in the second to microsecond range, it is experimentally not possible to predict the bulk physical properties of these elements, and one fully relies on numerical methods to learn more about these interesting elements. Yet, there are some hints that oganesson could be solid at room temperature. For example a simple extrapolation of the melting curves predicts a melting temperature close to room temperature and an increase in chemical activity is predicted due to the relativistic increase in polarizability with respect to radon [7]. This motivated us to study the melting point of oganesson by numerical methods, a formidable task as both relativistic and electron correlation effects need to be considered.

The solid to liquid transition is the most common phase transition which everybody experiences in daily life, yet the intrinsic mechanism that leads to melting is still not well understood. Melting is a first order phase transformation and is known to occur at a temperature at which the Gibbs free

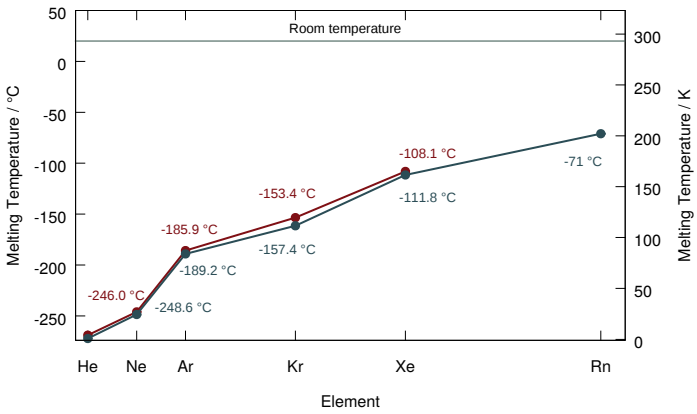

Figure 1.1.: All experimentally known melting (blue) and boiling (red) temperatures [2] of the noble gases in the Group 18 of the Periodic Table.

energies of the solid and the liquid states are equal. Besides, the solid and liquid phase or the transition between the two can be recognized by a range of different characteristics. The solid is rigid and topologically long-range ordered whereas the liquid is fluid and topologically long-range disordered, see Fig. 1.2. Furthermore, the solid to liquid transition can be recognized by a sudden increase in volume, entropy, pressure, inner energy, and an increase in the specific heat. Yet phenomena such as disorder, melting in clusters and rearrangements in structures in clusters, superheating and supercooling are little understood at the microscopic level.

Statistical physics aims to understand the behavior of systems composed of many interacting particles at the macroscopic level, and can be used as an effective tool to understand the nature of melting. However, due to the complexity of the system, it is not possible to describe the system analytically, and thus must be studied by means of numerical approaches instead. Determining the melting point of noble gases using ab-initio methods is a difficult task and to obtain an accurate value of the melting temperature one has three major important tasks to fulfill. First, the system's interaction needs to be computed up to high accuracy. Secondly, the thermodynamics that describes the system of interest needs to be known, and third, the properties of the system need to be obtained by the method of choice (algorithm). The most popular simulation methods today are molecular dynamics (MD) [8] and Monte Carlo (MC) [9] simulations, both of which rely on an accurate description of the interatomic interactions.

The Monte Carlo method allows efficient computation of high-dimensional integrals which would be too complex to solve analytically and aims to reproduce the statistical behavior of a system at the thermodynamic equilibrium.

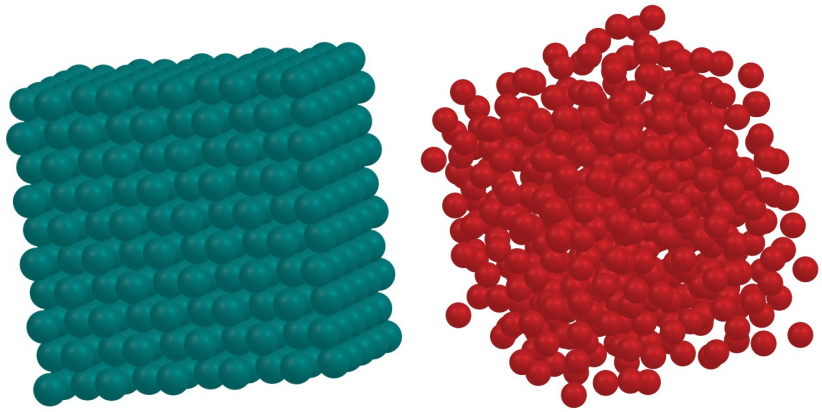

Figure 1.2.: (Left) a solid with long-range order, (right) a disordered liquid

To that purpose, configurations are randomly generated with the appropriate probability distribution. These configurations are then used to compute the statistical properties of the system, such as the inner energy, pressure and volume. Molecular Dynamics is different in the sense that it calculates the time dependent behavior of a molecular or atomic system, which would be an obvious advantage if one is interested in the time evolution of the system. However, Molecular Dynamics needs rather long simulation times to obtain averages of statistical properties accurately.

The accurate description of the electronic structure is for most atoms and molecules the principal source of errors since the electronic interactions cannot be treated without approximations for relativistic and electron correlation effects. The interaction potential of the noble gases is perhaps special in this sense as a many-body expansion of the total interaction energy into molecular fragments converges relatively fast, and the overall interaction of the ensemble can be approximated by two- and three-body forces only making the group of rare gases excellent candidates for MC simulations.

Earlier work on the melting of the noble gases neon and argon using MC techniques has been carried out by Pahl et al. [10–12] and an unprecedented accuracy of 1 K was obtained for the melting points. The melting of the noble gases argon, krypton and xenon was studied by Bochetti et al. [13], where the interaction was approximated by the two-parameter Lennard Jones potential. The determined melting points were systematically too high in comparison to the experimental results, hinting that a more accurate treatment of the interaction-potential is necessary. The melting of argon by MC techniques has also been studied at high pressure challenging existing experimental data [14]. In this thesis, we will extend this line of research to study the solid-liquid phase transition of the heaviest noble gases in the Periodic Table.

For this, we have to include relativistic effects which become increasingly

more important for the heavier elements (Z^2 scaling with nuclear charge) of the periodic table. Such effects are expected to have significant contributions to the interaction potential of both radon and oganesson, especially for the latter where the valence p-shell is split by 10 eV due to spin-orbit coupling [15]. A theory based on Einstein's theory of relativity is thus required to predict the properties of these elements that cannot be recovered within a non-relativistic formalism. For this reason, interaction potentials for oganesson are developed at different levels of relativistic treatment such that the contributions of relativistic effects to the melting temperature can be studied for the first time.

Outline

The first part of this thesis, chapters 2-5, concentrates on the methodology for computing the required ab-initio interaction potentials of the noble gases. The necessary electronic structure methods are discussed in chapter 2 followed by a brief overview of approximate relativistic Hamiltonians presented in chapter 3. A concise overview of different properties of basis sets is given in chapter 4. Finally, in chapter 5, the exact method for calculating the interaction energy of the rare gas dimers and trimers is given. The second part of this thesis concerns the functions that describe the interaction potential to be used during the Monte Carlo simulations. Analytical functions describing the two- and three-body potentials is the subject of chapter 6. Chapter 7 gives details on the fitting method and resulting parameters for the potentials are listed. The derived spectroscopic constants of the two-body potential are given in chapter 8. In the third part of the thesis, the melting phenomena is discussed. The thermodynamics of melting is reviewed in chapter 9. Different aspects of the Parallel Tempering Monte Carlo algorithm are thoroughly explained in chapter 10. The results of the Monte Carlo simulations are presented in the fourth part of this thesis. Chapter 11 presents the melting temperatures and densities of the noble gases obtained from the Monte Carlo simulations. The final part of this thesis addressess two interesting analytical findings. First, in chapter 12 melting of the Lennard-Jones potential (in reduced units) is examined which are helpful to evaluate the analytical results. A linear relation between the cohesive energy and the melting temperatures as well as the formula for the melting temperature as a function of the analytically expressed bulk modulus and interaction potential are derived in chapter 13. Chapter 14 addresses the superheating correction term. A derivation of this factor starting from the entropy difference between the solid and the liquid phase is given. A brief summary and outlook to future developments are provided in chapter 15.

Part I.

Ab-initio Potentials

2. Solving the Electronic-Motion Problem

In the following sections, the electronic Schrödinger equation is introduced and a brief description of computational methods that solve this equation is given. Solving the electronic Schrödinger equation in an ab-initio fashion leads to the (multi-reference)) Hartree-Fock (HF) method as a starting point after which post-Hartree-Fock methods for dynamic electron correlation such as Configurational Interaction (CI) and Coupled Cluster (CC) are introduced. This will help the reader to understand the accuracy of the ab-initio potentials developed here for the noble gases. For detailed mathematical information about these methods, the reader is referred to the standard textbooks on theoretical and computational chemistry [16–19].

2.1. Born-Oppenheimer Perturbative Approach

Within the quantum-mechanical framework the density of states is described by a wave function $\Psi(R, r, t)$, where R symbolizes all N_{nuc} nuclear coordinates (N vectors of the nuclear coordinates $\boldsymbol{R}_i, i = 1, ..., N_{nuc}$) and r all N_{elec} electron coordinates (including spin). In the non-relativistic case Ψ is a solution to the spin-independent time-dependent Schrödinger equation

$$H(R, r, t)\Psi(R, r, t) = i\hbar\frac{\partial}{\partial t}\Psi(R, r, t) \tag{2.1}$$

H is the many-particle Hamiltonian that will be specified below. For states of which the probability distribution does not vary with time one obtains the stationary form of Eq. (2.1)

$$H(R_N, r)\Psi(R, r) = E\Psi(R, r) \tag{2.2}$$

The square of the wave function is interpreted as the probability density and $E = \langle\Psi| H |\Psi\rangle$ is identified as the total energy of the physical system for a normalized Ψ. The many-particle Hamiltonian consists of kinetic T and

potential V terms working on both the electrons and nuclei (in SI units)

$$\begin{aligned} H =& T_e + T_n + V_{ee} + V_{en} + V_{nn} \\ =& -\frac{\hbar^2}{2m_e}\sum_{i}^{N_{elec}} \nabla_i^2 - \frac{\hbar^2}{2}\sum_{A}^{N_{nuc}} \frac{\nabla_A^2}{m_A} \\ &+ \frac{1}{2}\sum_{i\neq j}^{N_{elec}} \frac{e^2}{4\pi\epsilon_0 r_{ij}} - \sum_{i}^{N_{elec}}\sum_{A}^{N_{nuc}} \frac{e^2 Z_A}{4\pi\epsilon_0 r_{iA}} + \frac{1}{2}\sum_{A\neq B}^{N_{nuc}} \frac{e^2 Z_A Z_B}{4\pi\epsilon_0 R_{AB}} \end{aligned} \tag{2.3}$$

In the above equation, m_e and m_A are the mass of the electrons e and nuclei A respectively, Z_A is the nuclear charge (atomic number) of the nucleus A. ∇_i^2 and ∇_A^2 are the Laplacian operators of the electron and nuclei respectively. The distance between the ith electron and Ath nucleus $r_{iA} = |\boldsymbol{r}_{iA}|$, the distance between the ith electron and jth electron $r_{ij} = |\boldsymbol{r}_{ij}|$ and the distance between the Ath nuclei and Bth nuclei $R_{AB} = |\boldsymbol{R}_{AB}|$. Since nuclei are much heavier than electrons (proton-to-electron mass ratio is 1836.15), the nuclei move significantly slower than the electrons. Hence, as an approximation, one can consider the electrons in a molecule to be moving in the field of fixed nuclei. This is called the Born-Oppenheimer approximation (or the clamped nucleus approximation in the extreme where nuclear masses are taken to infinity). Within this approximation the kinetic energy of the nuclei can be neglected and the repulsion between the nuclei can be considered to be constant. The remaining terms in Eq (2.3) are part of the resulting electronic Hamiltonian

$$H_e = T_e + V_{ee} + V_{en} \tag{2.4}$$

such that we have (changing to atomic units)

$$\left[-\frac{1}{2}\sum_{i} \nabla_i^2 + \sum_{i\neq j}^{N_{elec}} \frac{1}{r_{ij}} - \sum_{i}^{N_{elec}}\sum_{A}^{N_{nuc}} \frac{Z_A}{r_{iA}} \right] \Psi(\boldsymbol{r}) = E_{el}\Psi(\boldsymbol{r}) \tag{2.5}$$

The wave function of the Schrödinger equation, $\Psi(\boldsymbol{r})$, can not be solved exactly for systems containing more than one particle. An approximate wave function, $\Phi(\boldsymbol{r})$ may be generated from a linear combination of functions, $f_j(\phi_1 \ldots \phi_n)$, functions containing single-electron wave functions ϕ_i called orbitals

$$\Phi(\boldsymbol{r}) = \sum_{j=1} a_j f_j(\phi_1 \ldots \phi_n) \tag{2.6}$$

Since the electronic wave function must fulfill Fermi-Dirac statistics for exchanging particles (the Pauli antisymmetry principle in the one-particle picture), an anti-symmetrized product of orbitals resulting in a Slater determinant represents the most simple approximation if a single determinant is

chosen

$$f(\phi_1, \phi_2, ..., \phi_N) = \begin{vmatrix} \phi_1(\boldsymbol{x}_1) & \phi_2(\boldsymbol{x}_1) & \dots & \phi_N(\boldsymbol{x}_1) \\ \phi_1(\boldsymbol{x}_2) & \phi_2(\boldsymbol{x}_2) & \dots & \phi_N(\boldsymbol{x}_2) \\ \vdots & \vdots & \ddots & \vdots \\ \phi_1(\boldsymbol{x}_N) & \phi_2(\boldsymbol{x}_N) & \dots & \phi_N(\boldsymbol{x}_N) \end{vmatrix} \tag{2.7}$$

Here, the ϕ_i denote the one-electron spin-orbitals and $\boldsymbol{x}_i = \{\boldsymbol{r}_i, \sigma_i\}$ are spatial ($\boldsymbol{r}_i$) and spin (σ_i) coordinates of the electrons. In this formulation each electron is associated with every orbital and the individual orbitals are chosen to be orthogonal, $\langle \phi_i | \phi_j \rangle = \delta_{ij}$.

The orbitals of the trial wave function can then be optimized to resemble the exact wave function as close as possible using the Ritz-Rayleigh variational principle for semi-bound operators, which results in the Hartree-Fock equations,

$$E_{HF} = \frac{\langle \Phi | \, H_{el} \, | \Phi \rangle}{\langle \Phi | \Phi \rangle} \geq E_{\text{exact}} = \frac{\langle \Psi | \, H_{el} \, | \Psi \rangle}{\langle \Psi | \Psi \rangle} \tag{2.8}$$

By varying the parameters of the wave functions ϕ_i the energy expectation value can be minimized.

2.2. Hartree-Fock

Variationally optimizing the HF energy. Eq. (2.8) leads to the Hartree-Fock equations,

$$f(\boldsymbol{x}_i)\phi_k(\boldsymbol{x}_i) = \epsilon_k \phi_k(\boldsymbol{x}_i) \tag{2.9}$$

$f(\boldsymbol{x}_i)$ denotes the Fock operator, $\phi_k(\boldsymbol{x}_i)$ are the orbital eigenfunctions and ϵ_i the eigenvalues of the orbitals The Fock operator is given by

$$f(\boldsymbol{x}_i) = h(\boldsymbol{x}_i) + \sum_{j}^{N_{elec}} \left[J_j(\boldsymbol{x}_i) - K_j(\boldsymbol{x}_i) \right] \tag{2.10}$$

The first term in the square brackets is called the Coulomb term, the interaction due to the electric repulsion of an electron in spin orbital $\phi(\boldsymbol{x}_i)$ with the average charge distribution of the other electrons

$$J_l(\boldsymbol{x}_i)\phi_k(\boldsymbol{x}_i) = \int d\boldsymbol{x}_j \phi_l(\boldsymbol{x}_j) \frac{1}{r_{ij}} \phi_l(\boldsymbol{x}_j)\phi_k(\boldsymbol{x}_i) \tag{2.11}$$

The second term in the square brackets exchanges spin orbitals ϕ_i and ϕ_j and is therefore called the exchange term. The exchange operator is defined as

$$K_l(\boldsymbol{x}_i)\phi_k(\boldsymbol{x}_i) = \left[\int d\boldsymbol{x}_j \phi_l(\boldsymbol{x}_j) \frac{1}{r_{ij}} \phi_k(\boldsymbol{x}_j) \right] \phi_l(\boldsymbol{x}_i) \tag{2.12}$$

Since the Fock $f(\boldsymbol{x})$ operator depends on the orbitals, the HF equation must be solved iteratively; i.e. starting from a set of trial wave functions the HF equations are solved and the coefficients of the trial wave functions are varied until self consistency is achieved.
As the orbitals ϕ_i are in general molecular orbitals, they are conveniently expressed as a Linear Combinations of Atomic Orbitals $\phi = \sum_j c_i j \chi_j$ (LCAO-MO theory). In such a basis-set expansion, the Hartree Fock equation takes the form of the Roothaan-Hall equation, during which the coefficients c_{ij} are optimized. The solution of the Roothaan-Hall equation yields M molecular orbitals if there are M one-electron basis functions, which leads to $2M$ spin orbitals for a closed shell state as the molecular orbitals are multiplied by spin state $\alpha(\omega)$ or $\beta(\sigma)$. For an n-electron system, the determinant $|\Phi_0\rangle$ is formed from the n orbitals with the lowest energy eigenvalues ϵ_i and the remaining number of spin orbitals with higher energies are the virtual or unoccupied spin orbitals. According to this principle, excited determinants such as the singly excited determinant $|\Phi_m^r\rangle$ can be constructed, where the spin orbital ϕ_m is replaced by ϕ_r. There are many efficient algorithms dealing with closed- and open-shell systems at the (multi-reference) Hartree-Fock level implemented in many computational program packages, and the reader is referred to standard textbooks [18, 19].

2.3. Correlation Energy and Configurational Interaction

The Hartree-Fock determinant for the ground state of a molecule does not account for all the energy contributions. The difference between the true eigenvalue of the Schrödinger equation and the Hartree-Fock energy, called the correlation energy, is given by

$$E_{corr} = E_{\text{exact}} - E_{HF} \tag{2.13}$$

For many-electron systems $E_{corr} << E_{HF}$, but is important for energy differences encountered in almost all properties. The method of Configuration-interaction (CI) expansion can be used to obtain the electron correlation energy. The idea is to represent the exact wave function as a linear combination of N-electron trial functions, that include both lowest energy orbitals as well as the virtual orbitals, and use the variational method to minimize the total energy. This wave function is expressed as a linear combination of Slater determinants which are constructed from a set of all possible Hartree-Fock orbitals

that were obtained upon diagonalization of the Roothaan-Hall equation.

$$\begin{aligned}\Phi_{el}^{FCI} =& C_0\Phi_0 + \sum_{m}^{occ}\sum_{r}^{vir} C_m^r\Phi_m^r \\ &+ \sum_{m<n}^{occ}\sum_{r<s}^{vir} C_{mn}^{rs}\Phi_{mn}^{rs} + \sum_{m<n<o}^{occ}\sum_{r<s<t}^{vir} C_{mno}^{rst}\Phi_{mno}^{rst} + \dots \end{aligned} \tag{2.14}$$

here Φ_0 indicates the Hartree-Fock Slater determinant. Φ_m^r denote the single excitation Slater determinants which are generated by substituting one of the ground states orbitals m with and excited orbital r. Similarly, Φ_{mn}^{rs} and Φ_{mno}^{rst} are double and triple excited states respectively.
The expansion coefficients $C = \{C_0, C_m^r, C_{mr}^{rs}, ...\}$ are determined by a variational optimization of the expectation value of the electronic energy. This expansion of the electronic wave function is called the configuration-interaction expansion. When taking into account all possible determinants, the CI method recovers 100% of the electron correlation energy (full CI). However, given some arbitrary set of $2M$ one-electron spin orbitals $\binom{2M}{N}$ different N-electronic Slater determinants can be constructed, this means that there is an factorial growth of the number of determinants with the size of the basis set and therefore one must usually truncate the trial function and only use a fraction of all possible N-electronic functions. Hence the truncated version only recovers part of the correlation energy. Another problem of the CI method is that truncated forms of the CI are not size consistent, nor size extensive (see Helgaker for a definition [16]). As a result the truncated CI recovers less and less electron correlation as the systems grow larger. Therefore the interaction energy of the noble gases is computed according to an alternative method, the Coupled-Cluster method, originally developed for nuclear shell structure calculations. This is discussed in the following section.

2.4. The Coupled-Cluster Method

Coupled-Cluster is a method for which the exact many-body wave function Ψ is expressed in terms of the Hartree-Fock wave function times an exponential excitation operator

$$\Psi_{CC} = e^T\Phi_0 \tag{2.15}$$

where Φ_0 is the ground-state HF wave function. The exponential excitation operator (called cluster operator) is understood in terms of a Taylor series

$$e^T = 1 + T + \frac{1}{2!}T^2 + \frac{1}{3!}T^3 + ... \tag{2.16}$$

where T, the cluster operator, is the sum of excitation operators T_k that transfers k electrons from occupied orbitals to vacant orbitals in all possible ways.

$$T = T_1 + T_2 + ... + T_N \tag{2.17}$$

Here, for example, T_1 transfers 1 electron to the vacant orbital and T_2 transfers 2 electrons to the vacant orbitals

$$T_1\Phi_0 = \sum_{m}^{occ}\sum_{r}^{vir} t_m^r \Phi_m^r \tag{2.18}$$

$$T_2\Phi_0 = \sum_{m<n}^{occ}\sum_{r<s}^{vir} t_{mn}^{rs} \Phi_{mn}^{rs} \tag{2.19}$$

The expansion coefficients t are understood in a similar way to the coefficients C in Eq. (2.14). By combining Eq. (2.17) and Eq. (2.16)

$$e^T = 1 + T_1 + \left(T_2 + \frac{1}{2}T_1^2\right) + \left(T_3 + T_2T_1 + \frac{1}{6}T_1^3\right) + \dots \tag{2.20}$$

The first term generates the reference HF determinant and the second term the single excited determinants. The terms in the first parenthesis generates doubly excited states, where T_2 is termed connected and T_1^2 is a disconnected term. By this expansion higher order excitations are created by lower order terms and therefore the cluster operator T_N can be truncated while remaining accurate. This is also the reason why the CC method is, in contrast to the CI method, size consistent.
Variationally determining the correlation energy as

$$E_{CC}^{var} = \frac{\langle\Psi_{CC}|H|\Psi_{CC}\rangle}{\langle\Psi_{CC}|\Psi_{CC}\rangle} = \frac{\langle e^T\Phi_0|H|e^T\Phi_0\rangle}{\langle e^T\Phi_0|e^T\Phi_0\rangle} \tag{2.21}$$

is not convenient, because upon expansion of the exponential operator this expression leads to a series of non-vanishing terms and terminates at T_N. Therefore the correlation energy is obtained from the Schrödinger equation in combination with the coupled-cluster wave function.

$$He^T\Phi_0 = E_{CC}e^T\Phi_0 \tag{2.22}$$

The projection coupled-cluster equations are obtained by projecting on the left with the HF wavefunction Φ_0 or excited determinants μ

$$\langle\Phi_0|He^T|\Phi_0\rangle = E_{CC} \tag{2.23}$$

$$\langle\mu|He^T|\Phi_0\rangle = E_{CC}\,\langle\mu|e^T|\Phi_0\rangle \tag{2.24}$$

These are the projected coupled-cluster equations and lead to a set of amplitudes of which the coefficients must be solved self consistently. The first equation gives the coupled-cluster energy E_{CC}

$$E_{CC} = E_0 + \sum_{i}^{occ}\sum_{r}^{vir} t_i^r \langle\Psi_0|H|\Psi_i^r\rangle + \sum_{i<j}^{occ}\sum_{r<s}^{vir} \left(t_{ij}^{rs} + t_i^r t_j^s + t_i^s t_j^r\right) \left\langle\Psi_0\middle|H\middle|\Psi_{ij}^{rs}\right\rangle \tag{2.25}$$

$$= E_0 + \sum_{i<j}^{occ}\sum_{r<s}^{vir} \left(t_{ij}^{rs} + t_i^r t_j^s + t_i^s t_j^r\right)\left(\langle\phi_i\phi_j|\phi_r\phi_s\rangle - \langle\phi_i\phi_j|\phi_s\phi_r\rangle\right) \tag{2.26}$$

where $\sum_i^{occ}\sum_r^{vir} t_i^r \langle\Psi_0|H|\Psi_i^r\rangle = 0$ because of Brillouin's theorem.
Higher order amplitudes are obtained by projecting Eq. (2.22) on the left with excited determinants $\phi_{mn}^{rs}, \phi_{mno}^{rst}$ or higher order excited determinants.

CCSD As stated above the cluster operator T_N can be truncated while remaining accurate, since higher excitations are generated from the lower order excitation operators. The lowest level of truncation is Coupled Cluster Doubles (CCD), which includes only the T_2 operator (Coupled Cluster Singles, CCS, gives zero electron correlation as the matrix element of the Hamiltonian between the ground state and a single excited determinant must be zero according to Brillouin's theorem). The CCSD method only includes single- and double-excitations operators, $T_k = T_1 + T_2$. The coupled-cluster singles and doubles was derived algebraically and numerically compared to CI calculations for H_2O and BeH_2 by Purvis and Barlett [20]. It was demonstrated that CCSD accounts for 98.7 % of the correlation energy.
Also including the triple and then quadruple excitations operators in the cluster operator, T_3 and T_4, leads to the CCSDT and CCSDTQ methods respectively. These are more expensive computationally as coupled-cluster scales exponentially with system size N as $\mathcal{O}(N^{2+2s})$ for up to and including s-fold excitations (i.e. s=4 for CCSDTQ and s=1 for HF).

CCSD(T) Triple excitations can be treated perturbatively by truncating the excitation operator T_N in Eq. (2.22) up to third order, $T = 1 + T_1 + T_2 + T_3$, but by only projecting the Schrödinger equation on the space of singly and doubly excited determinants. This perturbative treatment goes by the name CCSD(T) [21] and this method will be adapted to calculate higher order excitation corrections for the noble gases.

3. Relativity

The nuclear degrees of freedom are treated non-relativistically in quantum chemistry owing to the fact that the motion of the nuclei is very slow compared to the speed of light c. In contrast, for the moving electrons this does no longer hold as these can move with a significant fraction of the speed of light. This can easily be understood from the de Broglie relation $m\lambda v = h$, where short wavelengths (high energies) imply high speeds for the electrons. The electrons in the inner shells close to the nucleus experience an almost unscreened nuclear charge and therefore move fastest. As relativistic effects scale approximately like $(Z\alpha)^2$, the heavier elements with higher nuclear charge experience larger relativistic effects. These relativistic effects become increasingly more important for the heaviest elements in the periodic table and will have especially large influence on the interaction between radon and oganesson atoms. This may come as a surprise as velocities in valence shells are small according to the de Broglie relation, but counter-intuitively are surprisingly large even for electrons in valence shells as subtle quantum mechanical direct and indirect shell structure effects are at work [22–25]. In the computation of the ab-initio interaction potentials for the rare gases, relativistic effects are introduced through a specific choice of a relativistic Hamiltonian. Here a brief overview on the relativistic treatment (extension of the Schrödinger equation) of the electronic structure in atoms or molecules is given. [16, 17, 19, 26]

3.1. Relativistic Hamiltonian

The Schrödinger equation does not describe relativistic effects. The spin does not appear in this equation, and space and time coordinates are not treated on the same footing, i.e. the time derivative is only of first order whilst the derivative with respect to space is of second order. This means that the obtained wave function and resulting properties are not invariant under Lorentz transformations, which mix the time and space variables. To obtain a Lorentz invariant relativistic Hamiltonian formalism, one may start from the relativistically corrected expression for the total energy of the system

$$E^2 = p^2c^2 + m^2c^4 \tag{3.1}$$

By the replacement of E and p by quantum mechanical operators $i\hbar\frac{\partial}{\partial t}$ and $-i\hbar\nabla$, the (one-particle) Schrödinger equation becomes

$$-\hbar^2\frac{\partial^2\Psi(\boldsymbol{r},t)}{\partial t^2} = (-\hbar^2c^2\nabla^2 + m^2c^4)\Psi(\boldsymbol{r},t) \tag{3.2}$$

This expression known as the Klein-Gordon equation has a number of problems. The above expression, which describes a spin zero particle, leads to a probability density which is not positive definite, and is quadratic in the time derivative. Even if we take the square root of this expression we are faced with a Hamiltonian containing operators in a square root which are understood by its Taylor expansion, leading to a series of unbound differential operators. To maintain the linear time derivative, Dirac proposed to write the equation as

$$i\hbar\frac{\partial\Psi(\boldsymbol{r},t)}{\partial t} = [c\boldsymbol{\alpha}\cdot\boldsymbol{p} + \beta mc^2]\Psi(\boldsymbol{r},t) \tag{3.3}$$

$\boldsymbol{\alpha}$ and $\boldsymbol{\beta}$ must obey the relationships

$$\boldsymbol{\alpha}_i\boldsymbol{\alpha}_j + \boldsymbol{\alpha}_j\boldsymbol{\alpha}_i = 2\delta_{ij}\mathbf{1} \tag{3.4}$$

$$\boldsymbol{\alpha}_i\boldsymbol{\alpha} + \boldsymbol{\beta}\boldsymbol{\alpha}_i = 0 \tag{3.5}$$

$$\boldsymbol{\alpha}_i^2 = \boldsymbol{\beta}^2 = \mathbf{1} \tag{3.6}$$

The (irreducible) solution requires that $\boldsymbol{\alpha}$ and β are 4×4 matrices, $c\boldsymbol{\alpha}\boldsymbol{p}$ is the relativistic velocity operator and $\boldsymbol{\alpha}$ can be written in terms of the three Pauli 2×2 spin matrices (in standard notation) leading to the following quantities

$$\boldsymbol{\alpha}_{x,y,z} = \begin{pmatrix} 0 & \boldsymbol{\sigma}_{x,y,z} \\ \boldsymbol{\sigma}_{x,y,z} & 0 \end{pmatrix} \tag{3.7}$$

$$\boldsymbol{\beta} = \begin{pmatrix} \boldsymbol{I} & 0 \\ 0 & -\boldsymbol{I} \end{pmatrix} \quad \text{with} \quad \boldsymbol{I} = \begin{pmatrix} 1 & 0 \\ 0 & 1 \end{pmatrix} \tag{3.8}$$

$$\boldsymbol{\sigma}_x = \begin{pmatrix} 0 & 1 \\ 1 & 0 \end{pmatrix} \quad \boldsymbol{\sigma}_y = \begin{pmatrix} 0 & -i \\ i & 0 \end{pmatrix} \quad \boldsymbol{\sigma}_z = \begin{pmatrix} 1 & 0 \\ 0 & -1 \end{pmatrix} \tag{3.9}$$

The Dirac equation carries four components. Loosely speaking, two of which are assigned to particles (the electron and its anti-particle, the positron) and the two other degrees of freedom are understood as being related to the intrinsic magnetic moment (spin). Hence, fermionic spin is naturally described by the Dirac equation. Dirac-Hartree-Fock calculations are about a factor of 64 more expensive than non-relativistic Hartree-Fock calculations with an similar basis set.

As $\boldsymbol{\alpha}$ and $\boldsymbol{\beta}$ are block matrices, the Dirac equation can be written in matrix form with the wavefunction (bi-spinor) containing the large and small component (the terminology comes from the fact that the large component

contributes most to the one-particle density for an electron at not too high nuclear charge).

$$\begin{pmatrix} mc^2 & c\boldsymbol{\sigma}\cdot\boldsymbol{p} \\ c\boldsymbol{\sigma}\cdot\boldsymbol{p} & -mc^2 \end{pmatrix} \begin{pmatrix} \Psi_L \\ \Psi_S \end{pmatrix} = E \begin{pmatrix} \Psi_L \\ \Psi_S \end{pmatrix} \tag{3.10}$$

$$\boldsymbol{\Psi} = \begin{pmatrix} \psi_1 \\ \psi_2 \\ \psi_3 \\ \psi_4 \end{pmatrix} = \begin{pmatrix} \Psi_L \\ \Psi_S \end{pmatrix} \tag{3.11}$$

In the non-relativistic limit ($c \to \infty$) the small component disappears, and when the momentum goes to zero the large components disappears. In a Coulomb potential this shifts the continuum to the non-relativistic limit.

In a bound state, i.e. when the electron is confined by the Coulomb potential V of the nucleus, in its time independent form and in absence of a magnetic field the Dirac equation takes the form

$$\left[c\boldsymbol{\alpha}\cdot\boldsymbol{p} + \beta mc^2 + V\right]\boldsymbol{\Psi} = E\boldsymbol{\Psi} \tag{3.12}$$

$$\begin{pmatrix} V & c\boldsymbol{\sigma}\cdot\boldsymbol{p} \\ c\boldsymbol{\sigma}\cdot\boldsymbol{p} & V - 2mc^2 \end{pmatrix} \begin{pmatrix} \Psi_L \\ \Psi_S \end{pmatrix} = E \begin{pmatrix} \Psi_L \\ \Psi_S \end{pmatrix} \tag{3.13}$$

Here we changed conveniently the metric by shifting the total energy by $-mc^2$. By rearranging this equation the large component satisfies

$$\frac{1}{2m}(\boldsymbol{\sigma}\cdot\boldsymbol{p})\mathcal{K}(\boldsymbol{\sigma}\cdot\boldsymbol{p}) + (V - E)]\Psi_L = 0 \tag{3.14}$$

with

$$\mathcal{K} = \left(1 + \frac{E - V}{2mc^2}\right)^{-1} \frac{\boldsymbol{\sigma}\cdot\boldsymbol{p}}{2mc} \tag{3.15}$$

In the non-relativistic limit , $\mathcal{K} = 1$, and the Schrödinger equation is recovered. On the other hand, relativistic corrections are obtained by expanding $\mathcal{K}$

$$\mathcal{K} = \left(1 + \frac{E - V}{2mc^2}\right)^{-1} \approx 1 - \frac{E - V}{2mc^2} + ... \tag{3.16}$$

the so-called Pauli equation can be obtained when inserting the first-order expansion term in Eq. (3.14). Using the identity

$$(\boldsymbol{\sigma}\cdot\boldsymbol{A})(\boldsymbol{\sigma}\cdot\boldsymbol{B}) = \boldsymbol{A}\cdot\boldsymbol{B} = i\sigma\cdot(\boldsymbol{A}\times\boldsymbol{A}) \tag{3.17}$$

the one-particle relativistic expression is obtained

$$\left(\frac{p^2}{2m} + V(\vec{r}) - \frac{p^4}{8m^3c^2} + \frac{Z\boldsymbol{s}\cdot\boldsymbol{l}}{2m^2c^2r^3} + \frac{Z\pi\delta(\boldsymbol{r})}{2m^2c^2}\right)\Psi_L(\boldsymbol{r}) = E\Psi_L(\boldsymbol{r}) \tag{3.18}$$

where the first two terms are the non-relativistic kinetic and potential energy operators, the p^4 term is the mass velocity operator, this term describes the dependence of the electron mass on the velocity. The next term is the spin-orbit term where $\boldsymbol{s}$ is the electron spin operator and $\boldsymbol{l} = (\boldsymbol{r} \times \boldsymbol{p})$ is the angular momentum operator. This term describes the interaction of the spin of the electron with the magnetic field generated by the movement of (another) electron.
The last term is the Darwin term, also called Zitterbewegung, which describes the fact that it is not possible to know the exact position of the electron. Instead the electron is said to be approximately within a radius of λ_0, where λ_0 is the Compton wavelength. Both the mass velocity and Darwin corrections are scalar relativistic corrections and can be solved by a one-component treatment of the Hamiltonian, which is computationally not more expensive than variationally solving the non-relativistic Hamiltonian. However, these operators are not used anymore and are more of historical importance (e.g. the mass velocity operator is not bound from below). The spin-orbit term is a two-component expression and the corresponding Hamiltonian need to be treated by more advanced techniques.

Relativistic Electron-Electron Interaction The classical description of the interaction potential between two charges q_1 and q_2 is described by the Coulomb term

$$V(r_{12}) = \frac{q_1 q_2}{r_{12}} \tag{3.19}$$

An expression which treats the electron-electron interaction correctly to order $\mathcal{O}(c^{-2})$ can be derived in a purely classical context instead of a more rigorous quantum electrodynamic treatment. The relativistic two-particle potential is derived starting from the interaction between two electrons moving at different speeds in different direction derived from the Lorentz gauge. In this approximation the frequency of the exchange photon is neglected which yields the so-called frequency-independent Coulomb-Breit interaction

$$V_{ee}^{Coulomb-Breit}(r_{12}) = \frac{1}{r_{12}} - \frac{1}{r_{12}}\left[\boldsymbol{\alpha}_1 \cdot \boldsymbol{\alpha}_2 - \frac{(\boldsymbol{\alpha}_1 \times \boldsymbol{r}_{12})(\boldsymbol{\alpha}_2 \times \boldsymbol{r}_{12})}{2r_{12}^2}\right] \tag{3.20}$$

which can also be written as

$$V_{ee}^{Coulomb-Breit}(r_{12}) = \frac{1}{r_{12}} - \frac{1}{2r_{12}}\left[\boldsymbol{\alpha}_1 \cdot \boldsymbol{\alpha}_2 + \frac{(\boldsymbol{\alpha}_1 \cdot \boldsymbol{r}_{12})(\boldsymbol{\alpha}_2 \cdot \boldsymbol{r}_{12})}{r_{12}^2}\right] \tag{3.21}$$

The first term in this expression is the Coulomb term, which accounts for the classical charge-charge interaction and the term in the square brackets is called the Breit interaction. The first term in the Breit Hamiltonian is known as the Gaunt term representing the current-current interaction, and the second term is the gauge term.

The Dirac-Coulomb-Breit Hamiltonian is computationally more demanding for molecular applications as it requires new two-electron integrals between the large and small components.

Spin-Orbit interaction The fourth term in Eq. (3.18) and the Breit term are spin-dependent terms and give rise to various forms of spin-orbit coupling, which describe the coupling between the spin of the electron with its motion in a potential. The fourth term in Eq. (3.18) describes the spin-same-orbit (SO) interaction: the interaction of the electron spin with the magnetic field generated by its own orbital angular momentum. Decomposition of the Gaunt term shows that there are also other types of spin-orbit coupling, such as the spin-other-orbit (SOO) interaction, which describes the interaction of an electron spin with the magnetic field generated by the movement of another electron. A transformation of the Breit interaction into the two-component form, for example by a Foldy-Wouthuysen transformation, results in order-by-order terms of spin-spin, orbit-orbit and spin-orbit coupling terms.

3.2. Two-Component Transformation Techniques

In the Dirac equation, the small and the large component of the wavefunction appear separately in the bi-spinor, but they are coupled through the Dirac operator. Except for the free-particle case, one cannot decouple them into two independent differential equations. Even for the free particle case one obtains an infinite sum of relativistic perturbation operator in increasing orders of c^{-1}. It is, however, possible to perform step-by-step unitary transformations aiming at the remaining coupling operators between the small and large component to give successively smaller corrections for the total energy. Such transformations eliminate the negative energy from the positive energy states and for special choices of the unitary transformations can lead to operators which are bound from below and do not contain essential singularities. This corresponds to block-diagonalizing the Hamiltonian into an upper and lower block using as unitary transformation, such that we move from a four-component (Dirac) to a two-component (Schrödinger) picture.

$$H'_D = U H_D U^\dagger = \begin{pmatrix} h^{++} & 0 \\ 0 & h^{--} \end{pmatrix} \tag{3.22}$$

This way the positive electronic energy states are described by the h^{++} operator, while the negative (positronic) energy states are described by the h^{--} operator. This unitary transformation can be obtained in one step if a matrix representation of the Fock operator is available. In that case the h^{++} operator is called the eXact 2-Component (X2C) matrix. Using matrix algebra, the X2C method reproduces exactly the positive-energy spectrum

of the parent four-component Hamiltonian [27]. To minimize the error, the X2C-molecular mean field (mmf) was proposed by Sikkema et al. [28], which threats the SO and SOO coupling exact at the mean-field level.

In contrast to the X2C method, which relies on matrix algebra, the matrix can also be diagonalized by a perturbative treatment. The latter has historically appeared earlier then the X2C decomposition method as block-diagonalizing the Dirac description by matrix algebra was not yet solved. Multiple procedures to diagonalize the Dirac-Hamiltonian by a perturbative treatment have been developed, such as the Zeroth Order Regular Approximation (ZORA) Hamiltonian [29, 30], the Foldy-Wouthuysen (FW) transformation [31] (which gives the unitary transformation that diagonalizes the Dirac Hamiltonian for a free particle) and the Douglas-Kroll-Hess (DKH) method [32–34].
In case of a free particle ($V = 0$), the Free Particle Foldy-Wouthuysen (FPFW) transformation is given by

$$U_{FPFW} = \frac{c\beta(\boldsymbol{\sigma}\cdot\boldsymbol{p}) + mc^2 + E}{\sqrt{2E(mc^2+E)}} = \begin{pmatrix} X & XR \\ -XR & X \end{pmatrix} \tag{3.23}$$

with

$$X = \left(\frac{E+mc^2}{2E}\right)^{1/2} \quad \text{and} \quad R = \frac{c(\boldsymbol{\sigma}\cdot\boldsymbol{p})}{E+mc^2} \tag{3.24}$$

The Douglas-Kroll-Hess transformation is a regular transformation given by

$$U_{DKHn} = \sqrt{1+{W_n}^2} + W_n \tag{3.25}$$

which leads to regular operators and a variationally stable procedure. Within the DKH method the unitary transformation is written as a sequence of unitary transformations

$$U_{DKH} = \ldots U_{DKH2} U_{DKH1} U_{FPFW} \tag{3.26}$$

such that the DKH Hamiltonian becomes

$$H_{DKH} = \ldots U_{DKH1} U_{FPFW} H_D {U^\dagger}_{FPFW} {U^\dagger}_{DKH1} \ldots \tag{3.27}$$

The first-order DKH approximation is obtained by transforming the matrix with the FPFW transformation. When applying this transformation to the non-free particle Hamiltonian, the transformed Dirac operator will not be a diagonal matrix and the upper left part of the matrix is then used for the calculation and the off-diagonal terms define the U_{DKH1} operator. This operator will then be used for the DKH2 approximation. In second order we have the closed form

$$H_{DK2} = \sum_i h_{DK2}(i) + \sum_{i<j} g_{DK2}(i,j) \tag{3.28}$$

with

$$h_{DK2}(i) = E_i + A_i[V(i) + R_i V(i) R_i]A_i - W(i)E_i W(i) + \frac{1}{2}\{W(i)^2, E_i\} \tag{3.29}$$

with

$$E_i \equiv E_p = c\sqrt{\boldsymbol{p}_i^2 + c^2}, \quad A_i \equiv A_p = \sqrt{\frac{E_i + c^2}{2E_i}}, \quad R_i \equiv R_{\boldsymbol{p}} = \frac{c\boldsymbol{p}_i}{E_i + c^2} \tag{3.30}$$

and

$$g_{DK2}(i,j) = A_i A_j \left[\frac{1}{r_{ij}} + R_i \frac{1}{r_{ij}} R_i + R_j \frac{1}{r_{ij}} R_i + R_i R_j \frac{1}{r_{ij}} R_i R_j\right] A_i A_j \tag{3.31}$$

the anti-hermitian parameter $W(i)$ has a more complex form and we refer to ref. [17]. This operator is bound from below, contains no essential singularities and has been very popular in applications of relativistic electronic structure theory after B. Hess introduced it into molecular program packages [17].

4. Basis Sets

In this chapter a concise overview is given of some of the properties of basis sets which are relevant for the ab-initio calculations that were used for constructing the two- and three-body potentials of the heavy noble gases. For more information the reader is referred to the books [16, 17, 19].

One-Particle Expansion of the Many-Electron Wavefunction The many-electron wave function Ψ can be expanded into a linear combination of one-particle functions (called orbitals). For a molecule, it is convenient to expand these orbitals into a set of atom-centered basis functions χ_j where most of the electron density lies. These basis functions are of the following general form

$$\phi = \sum_{j=1}^{M} c_{jk}\chi_j \tag{4.1}$$

As a solution of the hydrogenic Schrödinger equation, the single electron wave function is of the form

$$\chi_{nlm}(r,\theta,\varphi) = NR_{nl}(r)Y_{lm}(\theta,\varphi) \tag{4.2}$$

where N is the normalization constant, $R_{nl}(r)$ are the radial functions, $Y_{lm}(\theta,\varphi)$ the spherical harmonics that describe the angular dependence of the orbitals, and n, l, m the corresponding quantum numbers. Slater type orbitals (STO) originate from the exact solutions to the hydrogenic atom

$$\chi_{\zeta,n,l,m}(r,\theta,\varphi) = NY_{l,m}(\theta,\varphi)r^{n-1}e^{-\zeta r} \tag{4.3}$$

STOs accurately describe the cusp in the core region and the exponential decay at long range, but for a multi-electron system do not have analytical solutions for three- or four-centered two-electron integrals and are difficult to treat. This makes working with STOs cumbersome and computationally very demanding. Gaussian type orbitals (GTO) (in spherical S or cartesian C form) are computationally far more efficient

$$\chi^{\mathrm{S}}_{\zeta,n,l,m}(r,\theta,\varphi) = NY_{lm}(\theta,\psi)r^{2n-2-l}e^{-\alpha r^2} \tag{4.4}$$

$$\chi^{\mathrm{C}}_{\zeta,l_x,l_y,l_z}(x,y,z) = N'x^{l_x}y^{l_y}z^{l_z}e^{-\alpha r^2} \tag{4.5}$$

and are therefore the preferred choice in the quantum chemistry community. The sum of l_x, l_y and l_z determines the type of orbital, i.e. $l = l_x + l_y + l_z = 1$

describes an s orbital, $l = 2$ a p orbital etc. The core region of GTOs do not have the correct cusp behavior at the nucleus, but are a continuous function instead of which the derivative is zero. This makes the description of GTOs less accurate in comparison to the STOs, however combined use of multiple GTOs closely approximate the desirable shape of an STO. The exponents, α, of the STO or GTO are usually to be determined by minimizing the Hartree-Fock total energy.

Number of Basis Functions A minimal basis set uses only one basis function χ for each orbital ϕ and was important in early days of quantum chemistry. Minimal basis sets are however not very flexible enough to accurately describe the many-electron wavefunction. Therefore a linear combination of multiple functions is used to represent the correct form of a one-particle function approaching of what is called the Hartree-Fock limit with increasing number of functions. For example, double-zeta (DZ) optimizes the linear combination of two functions, triple-zeta (TZ) makes use of three and quadruple-zeta (QZ) makes use of four functions.

Basis Set Contraction In molecular calculations an orbital is represented as a linear combination of several atom centered GTOs, of which an individual GTO is called a primitive function. After optimizing the exponents α of the primitive Gaussians using iterative Hartree-Fock procedure to minimize the energy, the full set of primitive GTOs can be combined into a smaller set of functions by forming fixed linear combinations. This is called a basis set contraction. At the Hartree-Fock level the atomic orbital coefficients can be used directly to obtain the contraction coefficients for the basis set.

Even-Tempered Basis Sets It can be shown that, upon optimization, the ratio between two consecutive exponents is approximately constant. This implies that the i-th exponent of the progression is characterized by $\alpha_i = ab^i$ where a and b are fixed constants for a given type of function and nuclear charge. Basis sets in which the exponents are constrained to be of this form are referred to as *even-tempered*. Such basis sets can be constructed in a computationally efficient way compared to the optimization of all exponents.

Polarization The Coulomb field produced by the neighboring atoms or molecules causes atoms and molecules to polarize leading to a deformation of the electron density (e.g. the Drude model or dispersive type of interactions). Including basis functions of angular momentum higher than that of the occupied atomic orbitals add flexibility within the basis set, allowing molecular orbitals to be more asymmetric about the nucleus. However, the exponents of the polarization functions cannot be optimized at the Hartree Fock level if the angular momentum is not represented by the core electrons. In such a

case these functions are unoccupied (virtual) and therefore make no contribution to the Hartree-Fock energy. Instead one needs to perform variational calculations with a correlated wave functions, such as CISD or CC, instead.

Augmentation The wavefunction at the tail plays an important role for weak interactions, and especially for the noble gas interactions the basis set augmentation by diffuse functions should be included. The Gaussians that account for such augmentations usually have very small exponents and decay slowly with distance from the nucleus. The wavefuntion of the tail is energetically not very important compared to the large total Hartree-Fock energy of the system, and therefore the exponents of the diffuse functions need be determined by other techniques, e.g. by energy minimization of atomic anions, where only the exponents of the additional diffuse functions are optimized, or from molecular calculations at long range. Alternatively, diffuse functions can be introduced by dividing the smallest exponent in an energy optimized basis set by a suitable scaling factor.

Relativistic Basis Sets Since the parameters of the basis sets are optimized by a variational procedure, the energies depend on the choice of Hamiltonian. Therefore a relativistically corrected Hamiltonian will have a different radial behavior compared to the wave functions obtained from the Schrödinger Hamiltonian. For example, for the Douglass Kroll-Hess (DKH) basis sets the wave functions are obtained using the DKH Hamiltonian. Such basis sets have harder functions as the s-orbitals contract relativistically. The basis sets can be optimized in a one-component scalar relativistic form similar to the non-relativistic case, or for the two- or four-component (e.g. spin-(same-)orbit coupling included). If spin-orbit coupling is included in a $j - j$ coupling scheme, the spherical harmonics also change. If the Dirac Hamiltonian is used, two basis sets are actually required, one for the small and the other one for the large component. These are related by the kinetic balance condition. Other procedure include the Dyall method, which optimizes the atomic occupied orbitals derived from numerical Dirac-Hartree-Fock calculations, while correlating functions are determined at the CISD level [35].

Basis Set Superposition Error and Counterpoise Correction As monomer A approaches monomer B, the dimer energy can be artificially lowered as monomer A utilizes the extra basis functions from monomer B to describe its electron distribution, and vice versa (understood from a Taylor expansion of the basis set at B at center A). This inconsistent treatment of the basis set as the intermolecular distance is varied is the source of the basis set superposition error (BSSE) [36] and can be corrected for by the counterpoise scheme [37]. The uncorrected interaction energy between monomers A and

B is computed as

$$\Delta E_{int}(AB) = E(AB)_{ab} - E(A)_a - E(B)_b \tag{4.6}$$

where the subscripts a and b denote the basis used, the symbol in parentheses denotes the chemical system considered. The amount of which the atoms A and B are artificially stabilized is estimated as

$$\Delta E_{CP} = E(A)_{ab} - E(A)_a + E(B)_{ab} - E(B)_b \tag{4.7}$$

where for $E(A)_{ab}$ the basis set a sits at center A and b at a distance where atom B resides (ghost atom). The counterpoise-corrected energy is then given as $\Delta E_{int} - \Delta E_{CP}$.

Electron Correlation Basis sets for electronic ground states are usually optimized by Hartree-Fock calculations. However, when including electron correlation, the basis set has also to describe the virtual orbital space. In this case the basis set is constructed by first performing Hartree Fock calculations with given primitive Gaussians, after which the given set or sub-set of occupied orbitals is optimized (for example optimizing contraction coefficient and/or exponents) using a correlated method (CISD, CC, etc) leading to so-called correlation consistent basis sets (see below).

The electron correlation energy can be partitioned into core and valence contributions. The valence correlation energy is the correlation energy obtained from calculations where excitations are allowed only from the valence space, core correlation energy arises from excitations out of the core space, and core-valence correlation energy arises from excitations out of the core space coupled with excitations out of the valence space. Since core electrons are least affected by chemical processes, for many processes it is sufficient to correlate the valence electrons only.

Correlation-Consistent Basis Sets Basis sets that are set up according to a correlation consistent (cc) type of contraction scheme constitute of a set of primitive functions (which are not necessarily of the same function type) that contribute to a similar amount of correlation energy [38]. Multiple basis sets may then be constructed such that each basis set contains all correlating orbitals that lower the energy by comparable amounts, in this case the basis sets are called *correlation consistent.*

Two-Point Basis Set Extrapolation Correlation consistent basis sets have the advantage that they converge relatively smooth to the complete basis set (CBS) limit with increasing size and angular momentum included. For example, the error in the cc-pVXZ basis is given by $\Delta E_X \approx AX^{-3}$ [39, 40], where X is the cardial number of the basis set ($X = 2$ for DZ, $X = 3$ for TZ, etc).

The relation between the correlation-consistent energies and the energy in the basis-set limit therefore is

$$E_n = E_{CBS} - AX^{-3} \tag{4.8}$$

An extrapolation scheme can be formulated, which allows to obtain the CBS energy from just two energies produced with correlation consistent basis sets with cardial numbers X and Y. By combined use of the two energies

$$E_{CBS} = E_X + AX^{-3} \quad \text{and} \quad E_{CBS} = E_Y + AY^{-3} \tag{4.9}$$

one can eliminate A and obtain

$$E_{CBS} = \frac{X^3 E_X - Y^3 E_Y}{X^3 - Y^3} \tag{4.10}$$

This is called the two-point extrapolation scheme [16, 41] and will be used for extrapolating the ab-initio potentials of the dimers and trimers of xenon, radon and oganesson to the CBS limit. Other extrapolation schemes have been proposed that use three-parameter extrapolation [42, 43], but are not employed in this thesis.

Explicitly Correlated Methods that employ wave functions that depend explicitly on the interelectronic distance r_{ij} are known as explicitly correlated methods. The basis functions are formed by multiplying an orbital product by a function $f(r_{ij})$ called a correlation factor.

$$f(r_{ij}) = 1 + \frac{1}{2} \sum_{i>j} r_{ij} \tag{4.11}$$

This is a superior method to introduce the Coulomb-cusp behavior, which are otherwise difficult to generate using Gaussian basis sets.

5. Ab-initio Potentials for the Interaction between Xe, Rn and Og Atoms

This chapter provides computational details on the two- and three-body ab-initio potentials for the noble gas interactions. The reader is referred to [44–46] where the interaction potentials for xenon, radon and oganesson are discussed in great detail.

5.1. Two-body Potentials

To construct the pair potential for the noble gas interactions 34 distances were selected in the range from 3.0 to 16.0 Å, with a finer spacing around the expected minimum to guarantee an accurate description around the two-body equilibrium distance. For krypton the two-body potential computed by Jäger et al. [47] is adapted and will not be discussed here.

Scalar relativistic effects for CCSD(T) The Molpro 2015.1 program package [48–51] was used to compute electronic energies at the coupled-cluster level which included excitations from singles, doubles and perturbative triples (CCSD(T)) with all electrons explicitly correlated. The counterpoise correction is utilized to account for basis set superposition errors (BSSE) in which the monomers were calculated in the same subspace of basis functions as used for the dimers including the full set of basis functions in all monomer calculations at the respective positions of the second atom [52].

For **xenon** and **radon** scalar-relativistic effects were considered via a second-order and third-order Douglas-Kroll-Hess approximation (DKH2 and DKH3) for xenon and radon respectively. Augmented (aug), correlation consistent (cc), weighted core-valence triple zeta (wCVTZ), weighted core-valence quadruple zeta (wCVQZ), Douglas-Kroll-Hess (DK) basis sets were utilized for these calculations [53]. These basis sets have the short hand notation aug-cc-pwCVTZ-DK and aug-cc-pwCVQZ-DK .

For **oganesson** a different approach was used for computational efficiency. Here scalar relativistic effects were considered via the spin-free variant of the eXact-2-Component (X2C) scheme as implemented in the program package DIRAC. [54–57] Augmented, correlation consistent, core-valence, Douglas-

Kroll-Hess basis sets, aug-cc-pwCVTZ-NR, aug-cc-pwCVTZ-X2C and aug-cc-pwCVQZ-X2C were generated for these calculations.
For all three elements an extrapolation to the complete basis set (CBS) limit was performed by using a two-point extrapolation scheme, Eq. 4.10, using the TZ and QZ basis sets. The 5Z basis sets were computationally not feasible, therefore we used this scheme rather than a three-point extrapolation.

Correction to the energy from higher excitations Higher excitations of the valence electrons were calculated as correction terms to the 2-body interaction potential. For each correction the lower-level result was subtracted from the higher-level one. The combination of highest number of correlated electrons and most accurate basis set which was feasible for the higher-level calculation were taken. These calculations were performed with the MRCC program package [58–62] interfacing with Molpro 2015.1. In the following, orbitals given in brackets as a subscript are specifying the chosen active space in the electron correlation treatment and the underlying basis set is given after the forward slash.

For **xenon**, full triple corrections, $E^{(2)}_{\Delta T}$, were obtained by subtracting the perturbative triple CCSD(T)-DKH2$_{(4d5s5p)}$ /aug-pwCVTZ-DK contributions from the full triple CCSDT-DKH2$_{(4d5s5p)}$ /aug-pwCVTZ-DK results. In the same way, perturbative quadruples, $E^{(2)}_{\Delta(Q)}$, were computed from the difference between CCSDT(Q)-DKH2$_{(5s5p)}$ /aug-pwCVTZ-DK and CCSDT-DKH2$_{(5s5p)}$ /aug-pwCVTZ-DK energies and full quadruple corrections, $E^{(2)}_{\Delta Q}$, from the difference between CCSDTQ-DKH2$_{(5s5p)}$ /aug-pwCVDZ-DK and CCSDT(Q)-DKH2$_{(5s5p)}$ /aug-pwCVDZ-DK results.

For **radon** full triple corrections were obtained by subtracting the perturbative triple CCSD(T)$_{(5d6s6p)}$ -DKH3/aug-pwCVTZ-DK contributions from the full triple CCSDT$_{(5d6s6p)}$ -DKH3/aug-pwCVTZ-DK results. Perturbative quadruples were computed from the difference between CCSDT(Q)-DKH3$_{(6s6p)}$ /aug-pwCVTZ-DK and CCSDT-DKH3$_{(6s6p)}$ /aug-pwCVTZ-DK energies and full quadruple corrections from the difference between CCSDTQ-DKH3$_{(6s6p)}$ /aug-pwCVDZ-DK and CCSDT(Q)- DKH3$_{(6s6p)}$ /aug-pwCVDZ-DK results.

Finally, for **oganesson** full triple corrections were obtained by subtracting the perturbative triple CCSD(T)$_{(6d7s7p)}$/aug-cc-pwCVTZ-X2C contributions from the full triple CCSDT$_{(6d7s7p)}$/aug-cc-pwCVTZ-X2C results. Perturbative quadruples were computed from the difference between CCSDT(Q)-X2C$_{(7s7p)}$/aug-cc-pwCVTZ-X2C and CCSDT-X2C$_{(7s7p)}$/aug-cc-pwCVTZ-X2C energies and full quadruple corrections came from the difference between CCSDTQ-X2C$_{(7s7p)}$/aug-cc-pwCVDZ-X2C and CCSDT(Q)-X2C$_{(7s7p)}$/aug-cc-pwCVDZ-X2C results. The core-core contributions to the correlation energy are significant due the large number of core orbitals. How-

ever, we have carefully checked for numerical stability of core-core, core-valence and valence-valence contributions to the correlation energy, respectively, to ensure a smooth behavior around the minimum and in the dissociation limit.

Non scalar relativistic contributions To correct for non-scalar relativistic effects (e.g. spin-orbit), the DIRAC-15 program package [63] was used for CCSD(T) calculations [64] together with augmented, core-valence triple- and quadruple-ζ quality basis sets (dyall.acv3z and dyall.acv4z, respectively [35, 65]) and a Gaussian-type finite nucleus. The energies from those two basis sets were used to extrapolate to the CBS. Electrons in the [4d5s5p], [5d6s6p] and [6d7s7p] shells, for xenon, radon and oganesson respectively, were explicitly correlated and virtual orbitals above 30.0 a.u. were not included in the correlation treatment. The Dirac-Coulomb-Gaunt Hamiltonian was used, together with the converged Fock operator defining the transformation into the two-component (X2C-Gaunt) form together with the molecular mean-field approximation for the valence two-electron-interactions as described in detail by Sikkema et al. [66].

For **xenon** the spin-orbit correction term, $E^{(2)}_{\Delta SR-X2C}$, was obtained by taking the energy differences between CCSD(T)-X2C-Gaunt$_{(4d5s5p)}$ /CBS and CCSD(T)-DKH2$_{(4d5s5p)}$ /CBS energies.

Similarly, for **radon** the spin-orbit correction was obtained by taking the energy differences between CCSD(T)-X2C-Gaunt$_{(5d6s6p)}$ /CBS and CCSD(T)-X2C-Spinfree$_{(5d6s6p)}$ /CBS energies.

And for **oganesson**, the spin-orbit correction term was obtained as the energy differences between CCSD(T)-X2C-Gaunt$_{(6d7s7p)}$ /CBS and CCSD(T)-X2C$_{(6d7s7p)}$ /CBS energies.

The total two-body interaction energy is taken as the CCSD energy with added higher order excitation corrections and the spin-orbit contribution and is given by

$$E^{(2)} = E_{CCSD(T)} + E^{(2)}_{\Delta T} + E^{(2)}_{\Delta(Q)} + E^{(2)}_{\Delta Q} + E^{(2)}_{\Delta SR-X2C} \qquad (5.1)$$

5.2. Three-body Potentials

In order to compute non-additive three-body interaction energies again the Molpro 2015.1 program was used and the counterpoise correction was applied for the BSSE. In the following the computational details for the trimer potentials of krypton, xenon, radon and oganesson is discussed in detail.

The non-additive three-body interaction energies for **krypton** was calculated for 14 trimer geometries as equilateral triangles with bond lengths between 3.0 and 7.5 Å. Molpro 2015.1 was used to compute electronic energies

at CCSD(T)-DKH2$_{(4s4p)}$ /aug-cc-pwCVQZ-DK2 level of theory. The corrections from correlating sub-valence electrons was estimated with second-order Møller-Plesset perturbation theory(MP2). The correction was taken as the difference between all-electron MP2-DKH2/aug-cc-pwCVQZ-DK2 and MP2-DKH3$_{(4s4p)}$ /aug-pwCVQZ-DK2 calculations.

The non-additive interaction energy for 300 different **xenon** trimer configurations (with Xe-Xe distances between 2.1 and 7.9 Å) was computed at the CCSD(T)$_{(5s5p)}$ /aug-pwCVQZ-DK level of theory. The corrections from correlating sub-valence electrons was estimated from the difference between all-electron MP2-DKH3/aug-pwCVQZ-DK and MP2-DKH3$_{(5s5p)}$ /aug-pwCVQZ-DK calculations. Following the same method as proposed by Cencek et al. [67], the 300 trimer geometries were then chosen to represent the most important points on the potential energy surface.

The non-additive three-body interaction energies for **radon** was calculated for 38 trimer geometries as equilateral triangles with bond lengths between 2.2 and 16.0 Å and a finer spacing chosen between 2.8 and 4.8 Å. Molpro 2015.1 was used to compute electronic energies at CCSD(T)-DKH3$_{(6s6p)}$ /aug-pwCVQZ-DK level of theory. The corrections from correlating sub-valence electrons was estimated from the difference between all-electron MP2-DKH3/aug-pwCVQZ-DK and MP2-DKH3$_{(6s6p)}$ /aug-pwCVQZ-DK calculations. For radon spin-orbit effects are expected to have a significant contribution and were therefore also included in the three-body potential. The effect of spin-orbit coupling on the three-body potential was computed using DIRAC-15 for a set of 12 radon trimers with bond lengths between 3.3 and 7.0 Å. The correction was obtained from the energy differences between CCSD(T)- X2Cmmf$_{(6s6p)}$ /dyall.acv3z (note, the Gaunt term was not included here due to the high computational costs) and CCSD(T)-X2C-Spinfree$_{(6s6p)}$ /dyall.acv3z levels of theory.

For **oganesson**, the non-additive three-body interaction energies were calculated with the Molpro 2015.1 program package at the non-relativistic and scalar relativistic level, respectively, for 24 Og_3 trimer geometries as equilateral triangles with bond lengths between 3.8 and 16.0 Å and a finer spacing between 3.8 and 4.8 Å. The electronic energies were computed at CCSD(T)$_{(7s7p)}$/aug-cc-pwCVQZ-NR and CCSD(T)$_{(7s7p)}$/aug-cc-pwCVQZ-X2C levels of theory, respectively. For both levels of relativistic effects, the impact from correlating sub-valence electrons was estimated from the difference between all-electron MP2/aug-cc-pwCVQZ and MP2$_{(7s7p)}$/aug-cc-pwCVQZ. The effect of spin-orbit coupling to the three-body potential was estimated by computing the non-additive three-body interaction energies for a selection of 11 Og_3 trimers with bond lengths between 3.3 and 7.0 Å at CCSD(T)-X2C-mmf$_{(7s7p)}$/dyall.acv3z level of theory with DIRAC-15. The spin-orbit correction was obtained from the energy differences between these calculations and scalar relativistic CCSD(T)-X2C-spinfree$_{(7s7p)}$/dyall.acv3z calculations.

Part II.

Functions Describing the Ab-initio Potentials

6. Analytical Functions Describing the Interaction Potential

This chapter provides the functional forms of the two and three-body potentials used in this work in order to fit the many-body decomposition of the potential energy surface derived from accurate ab-initio calculations, and gives an overview of the theoretical motivation for their chosen analytical form. These two- and three-body potentials are fitted to analytical forms such that the interaction energy can be evaluated for all possible configurations that are generated during the Monte Carlo simulation. The functions need to be carefully chosen as they must describe the potential energy surface not only as accurately as possible, but also ought to be computationally efficient.

6.1. Two-body Potentials

For the long and short distance range different type of interactions between the atoms play a dominant role. It is therefore convenient to describe these two regions separately. At short range the repulsive Coulomb and Pauli (exchange) forces are well described by an exponential function. In the case of large separations, where the exchange and overlap effects can be neglected, the two-body dispersive terms, which can be derived with the aid of perturbation theory, become dominant. The following sections describe these two regions, followed by the relevant two-body functions.

6.1.1. Long Range Interaction

Suppose we have a wave function that describes atom A by $\Psi^A(1, 2, .., n_A)$ as a function of the coordinates of its n_A electrons, and by wavefunction $\Psi^B(1', 2', .., n'_B)$ that describes atom B as a function of the coordinates of its n'_B electrons (the primes are used to distinguish the labels of the electrons of molecule B from those of molecule A). This decomposition of a system into subsystems is very common in chemistry, e.g. we can think about σ-π separation in organic aromatic systems, of core-valence separation in pseudopotential theory, or for our purpose here of long-range interactions between two or more subsystems (atoms or molecules). The problem which such a formalism is that Fermi-Dirac statistics demands that the electrons are indistinguishable and the total wavefunction has to be anti-symmetric, i.e.

the wavefunction for the combined AB system should be written as an antisymmetrized product $\mathcal{A}\{\Psi_A\Psi_B\}$. Fortunately, for long-range interactions, where overlap between the two wavefunctions is negligible, corrections coming from the anti-symmetrization are small and can be neglected [68]. The interaction potential V between the subsystems can therefore be treated efficiently as a perturbation, such that the interaction of an N atomic system can be calculated using Reighleigh-Schrödinger perturbation theory.

$$H = H_0 + \lambda V(R_{AB}) \tag{6.1}$$

the unperturbed hamiltonian is $H_0 = H^A + H^B$ and the perturbation consists of the electrostatic interaction, $V(R_{AB})$, between the particles of atom A and atom B.

$$V(R_{AB}) = -\sum_{j=1}^{N_B} \frac{Z_A}{r_{Aj}} - \sum_{i=1}^{N_A} \frac{Z_B}{r_{Bi}} \tag{6.2}$$

$$+ \sum_{i=1}^{N_A}\sum_{j=1}^{N_B} \frac{1}{r_{ij}} + \frac{Z_A Z_B}{R_{AB}} \tag{6.3}$$

where the index i numbers the electron of atom A, j numbers the electrons of atom B and Z_A and Z_B the nuclear charge of atom A and atom B respectively. R_{AB}, r_{Aj}, r_{ij} denote the distance between the two atoms A and B, the distance from atom A to electron j and the distance between electrons i and j, respectively.

For the second order interaction energy $E^{(2)}(R_{AB})$ one finds

$$E^{(2)}(R_{AB}) = \sum_P \frac{\langle\Psi_0|V(R_{AB})|\Psi_P\rangle\langle\Psi_P|V(R_{AB})|\Psi_0\rangle}{E_P^{(0)} - E^{(0)}} \tag{6.4}$$

where the wave function $|\Psi_P\rangle$ for the total unperturbed two body system has the form

$$|\Psi_P\rangle = |p_A\rangle|p_B\rangle \tag{6.5}$$

with $|p\rangle$ the wavefunction of the individual atom p . The non-degenerate ground state $|\Psi_0\rangle$is represented by

$$|\Psi_0\rangle = |0_A\rangle|0_B\rangle \tag{6.6}$$

The difficulty in evaluating the second order interaction to the energy arises from the dependence of the potential on $1/r_{ij}$, the inverse distance between two electrons, which makes an expansion in a series of R^{-n}, where R is the distance between the two nuclei, difficult. The interaction energy $V(R_{AB})$ can be re-expressed with aid of the bipolar expansion. After such an expansion the potential is given in terms of dipoles, quadruples and higher-order terms, centered on the two nuclei.

One starts by expressing the potential around a single atoms as

$$\phi = \sum_i \frac{q_i}{|\mathbf{R} - \mathbf{r}_i|} \tag{6.7}$$

where q_i is a point charge situated at the points $\mathbf{r}_i$ with respect to an origin within it. At an outside point, a distance R from the origin the charge distribution will produce the above potential. When expanding the potential of the single atom as a Taylor series around R the potential is given in terms of monopoles

$$q = \sum_i q_i \tag{6.8}$$

dipoles

$$\mathbf{p} = \sum_i q_i \mathbf{r}_i \tag{6.9}$$

quadrupoles

$$\overleftrightarrow{\mathbf{Q}} = \sum_i q_i \mathbf{r}_i \otimes \mathbf{r}_i, \quad \text{e.g.} \quad Q_{12} = \sum_i q_i x_i y_i \qquad \text{etc.} \tag{6.10}$$

and higher order terms. Details of this expansion is given by [69]. The potential between two neutral atoms

$$V = \sum_{i \in A} \sum_{j \in B} \frac{q_j q_i}{|\mathbf{R} + \mathbf{r}_j - \mathbf{r}_i|} \tag{6.11}$$

can now be expressed as a sum of coupling terms between the multipole moments that describe the two charge distributions. It can be shown that the multipole expansion of the second-order interaction energy between a pair of neutral atoms gives rise to an induced potential energy

$$E^{(2)}(R) = -\frac{C_6}{R^6} - \frac{C_8}{R^8} - \frac{C_{10}}{R^{10}} - ... \tag{6.12}$$

where C_n are van der Waals or dispersion coefficients, given by

$$C_6 = C_{AB}(1,1) \tag{6.13}$$

$$C_8 = C_{AB}(1,2) + C_{AB}(2,1) \tag{6.14}$$

$$C_{10} = C_{AB}(1,3) + C_{AB}(2,2) + C_{AB}(3,1) \tag{6.15}$$

Here $C_{AB}(1,1)$ accounts for the dipole-dipole interaction, $C_{AB}(1,2)$, for the dipole-quadrupole interaction, $C_{AB}(2,2)$, for the quadrupole-quadrupole interaction and $C_{AB}(1,3)$ accounts for the dipole-octupole interaction. These constants are directly related to the imaginary-frequency polarizabilities through the Casimir-Polder relation [70]

$$C_{AB}(l_1, l_2) = \frac{(2l_1 + 2l_2)!}{4(2l_1)!(2l_2)!}\left(\frac{2}{\phi}\right) \int_0^\infty \alpha_{l_1}^A(i\omega)\alpha_{l_2}^B(i\omega)d\omega \tag{6.16}$$

6.1.2. Short-Range Interaction

At short interatomic distances perturbation theory can not be applied due to strong electron overlap. Attributed to Coulomb and Pauli (exchange) forces, the two-body interaction becomes purely repulsive at short range. The obtained repulsive part of the ab-initio potential energy can, for example, be fitted to a simple exponential function, called the Born-Mayer term [71],

$$E_{BM}^{(2)}(R) = Be^{-\alpha R} \tag{6.17}$$

where B and α are adjustable parameters. More sophisticated short-range functions are discussed below.

6.1.3. Functional Forms of the Two-body Interaction

Over the years many functional forms for dimer potentials have been developed (for a review on this topic see ref.[72]). Here we will present, for our purpose, the most important potentials currently in use. While the Lennard-Jones and the Morse potential are most widely used because of its mathematical simplicity and computationally efficient form, the Extended Aziz potential is one of the most accurate potential forms currently available, but is heavily parametrized. The recently proposed Extended Lennard-Jones potential [73] is perhaps the best compromise between computational efficiency and high accuracy, which forms the basis for our Monte-Carlo simulations.

The Lennard-Jones Potential

For the rare gas dimers the most commonly used functional form for the interaction potential is the Lennard Jones (6-12) potential

$$E(R) = \epsilon\left[\left(\frac{R_m}{R}\right)^{12} - 2\left(\frac{R_m}{R}\right)^{6}\right] \tag{6.18}$$

where ϵ and R_m are fitting parameters that are directly extracted from the (calculated or experimental) well depth and the equilibrium distance (location of the minimum). Alternatively the Lennard-Jones potential can be written as

$$E(R) = 4\epsilon\left[\left(\frac{\sigma}{R}\right)^{12} - \left(\frac{\sigma}{R}\right)^{6}\right] \tag{6.19}$$

where $\sigma = R_m 2^{-1/6}$ is the finite distance at which the potential is zero. At large separations ($R \gg \sigma$) the inverse sixth power component is the dominant attractive term and represents the dipole-dipole interaction within the classical Drude [74] or London dispersion model. At small separation, ($R \ll \sigma$), the inverse 12th power component is the dominant term, leading to a strong repulsive force.

This potential is a special case of the function introduced by Mie in 1903 [75], (also proposed by Simon and Simson [76]),

$$E(R) = \frac{A}{R^n} - \frac{B}{R^m} \tag{6.20}$$

who was the first person to describe the interaction potential by both an attractive as a repulsive term. Wang [77] was the first to demonstrate that the interaction between two hydrogen atoms resembled that of two interacting dipoles with the attractive force at large distances varying inversely with the seventh power of the distance (consequently the potential of the attractive field is of the form R^{-6}). Eq. (6.19) was however named after Lennard-Jones [78] [79] who used a modified form of perturbation theory to simplify the calculation of the van der Waals fields of two atoms. The importance of the R^{-6} dispersion term was realized by Lennard-Jones [80] only after London's paper appeared in 1930 [81]. In the same year Hasse used a specially adapted variational procedure to study the long range interaction between hydrogen atoms and between helium atoms, and predicted the dipole polarizability of helium to reasonable accuracy [82]. For the part of Eq. (6.19) describing the repulsive Pauli forces it was difficult to compare experiment to theoretical findings, although it was known that they fell of rapidly (as $e^{\alpha r}/r$). Therefore, the choice of 12 as an index of repulsion was one of mathematical convenience, however any number within 14 ± 5 gave equally good agreement with the experimental data available at the time. [80]

The (Extended) Aziz potential

Because of its mathematical simplicity, the Lennard-Jones potential is the most widely used potential function in many physical and chemical applications. However, the accuracy of the potential is rather limited. Due to the limited number of parameters, there is not enough flexibility to describe the potential precisely. The Aziz potential was initially suggested by Ahlrichs [83] in 1977, who combined information from ab-initio Hartree Fock calculations, which describe the short range repulsive forces, with an empirical estimate of the long range attractive terms, leading to an accurate description of the potential for short dimer distances as well as for the dispersive region. In order to give a good description for the intermediate region, the individual long range dispersion coefficients are multiplied by a damping function. This approach carried the name Hartree Fock Dispersion (HFD).

$$E(R) = \epsilon(A\exp(-\alpha x) - \left(\frac{C_6}{x^6} + \frac{C_8}{x^8} + \frac{C_{10}}{x^{10}}\right)F(x)) \tag{6.21}$$

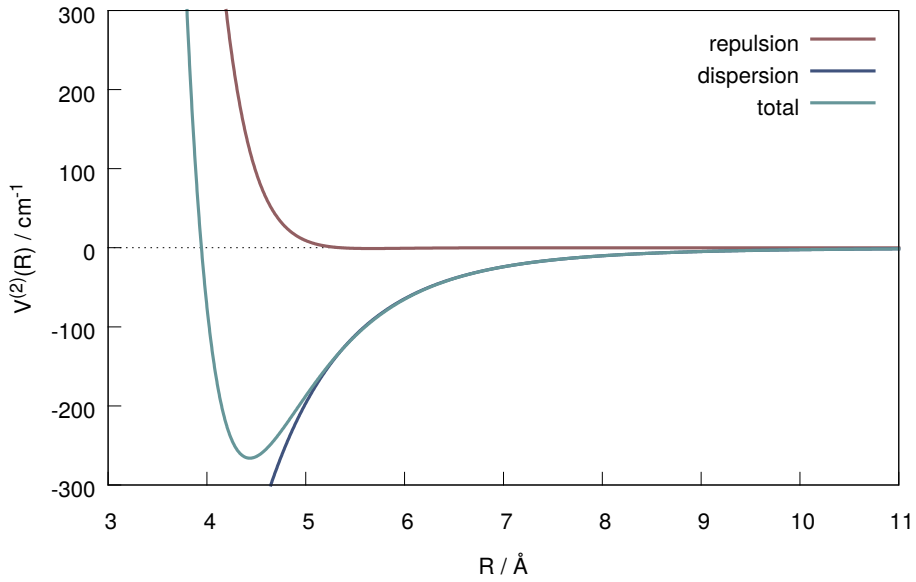

Figure 6.1.: The repulsive and attractive parts of the Extended Aziz potential energy for the radon dimer

with a chosen damping function

$$F(x) = exp - \left[\left(\frac{D}{x} - 1\right)^2\right] \qquad \text{if } x < D \tag{6.22}$$

$$= 1 \qquad \text{if } x \geq D \tag{6.23}$$

and $x = R/r_m$. The HFD potential was later adapted and modified by Aziz to describe intermolecular interaction for argon [84] and helium [85]. Aziz modified the potential such that the repulsive component had one additional parameter which gives a more accurate description to the short range behavior. Meanwhile improved damping functions were formulated by Tang and Toennies. These damping functions in combination with an higher order polynomial is nowadays often employed to accurately fit two-body potentials [86] [87]

$$E_{EA}(R) = (a + bR)e^{-A_1R+A_2R^2+A_{-1}/R+A_{-2}/R^2} + \sum_{n=3}^{8} f_{2n}(R)\frac{C_{2n}}{R^{2n}} \tag{6.24}$$

where A, B, C, D, E, α, b and the asymptotic dispersion coefficients C_n are fit parameters. $f_{2n}(x)$ is the universal Tang-Toennies damping function, which is given in the following section.

The Tang Toennies Damping Function

The boundary conditions for the damping function $f_{2n}(x)$ in the expression

$$E^{(2)}(R) = E_{SCF}(R) + \sum_{n=3}^{8} f_{2n}(R)\frac{C_{2n}}{R^{2n}} \tag{6.25}$$

is chosen such that it approaches unity in the dissociation limit $R \to \infty$, i.e. the dispersion potential becomes the dominant term. In the limit of $R \to 0$ the damping function goes to zero such that the (extended) Born-Mayer function is the dominating term.
In order to find a damping function that satisfies such a behavior, we make use of an alternative description of the dispersive region as formulated by Tang and Toennies [88]. They introduced an additive exponential term taking care of overlap effects that become important in the intermediate range,

$$E^{(2)}_{pol.disp}(R) = E_{SCF}(R) - \sum_{n>3}^{\infty} g_{2n}(R)\frac{C_{2n}}{R^{2n}} + M(b^2 - 2b/R)e^{-bR} \tag{6.26}$$

Here g_{2n} is not a damping function per se, instead this function equals one except for the smallest term serving to cut off the series to avoid asymptotic divergence [89]. Both g_{2n} and the third term dampen the dispersion series in the vicinity of the potential well. Finally, a solution to the damping function is obtained by equating the last two terms in Eq. 6.26 with the damped dispersion series (6.25) whcih can be substituted in Eq. (6.25).

$$-\sum_{n>3}^{n'} \frac{C_{2n}}{R^{2n}} + M(b^2 - 2b/R)e^{-bR} = -\sum_{n>3}^{\infty} f_{2n}(R)\frac{C_{2n}}{R^{2n}} \tag{6.27}$$

where n' denotes the larges value of n in Eq 6.26, for which $g_{2n} = 1$. Solving this equation with the boundary conditions

$$f_{2n}(R) \to 1, R \to \infty \tag{6.28}$$

$$f_{2n}(R) \to 0, R \to 0 \tag{6.29}$$

leads to an universal expression for the individual coefficients of the damping functions.

$$f_{2n}(R) = 1 - \left[\sum_{k=0}^{2n} \frac{(bR)^k}{k!}\right] e^{-bR} \tag{6.30}$$

The Extended Lennard Jones Potential

Although incredibly accurate, for numerical purposses the Extended Aziz potential can often be computationally too demanding. Schwerdtfeger et al. [73]

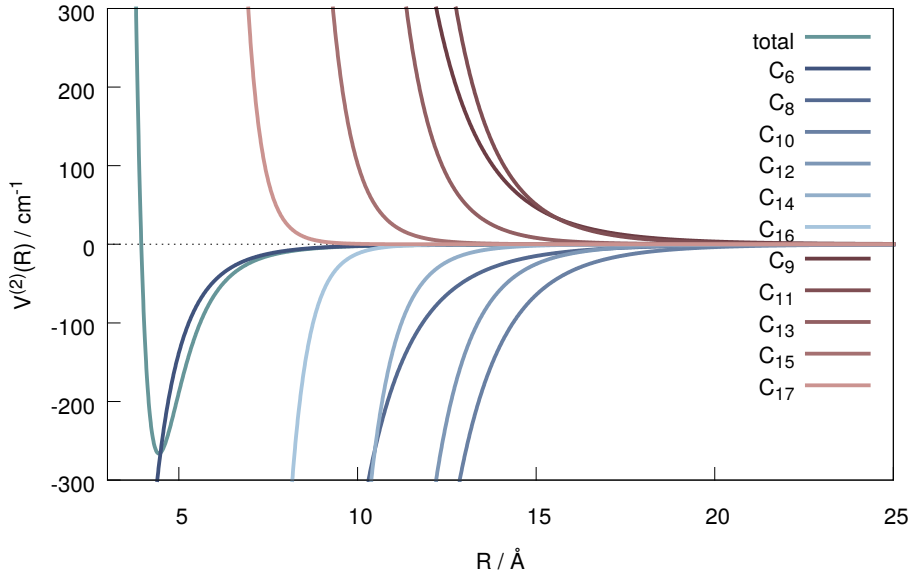

Figure 6.2.: Individual contributions for the ELJ potential to the total interaction potential energy for the radon dimer.

therefore proposed to fit the data points to an inverse power series (extended Lennard-Jones potential) which is computationally more efficient, but also capable of giving a very accurate description to the computed two body potential,

$$E^{(2)}(R) = \sum_{n=6} \frac{C_n}{R^n} \tag{6.31}$$

The advantage of this relatively simple potential is that it is nearly as accurate as the Extended Aziz potential, while it performs computationally as efficient as the Lennard-Jones potential. Note that in general the coefficients C_n do not correspond to the well-known van der Waals coefficients describing the long-range behavior of two interacting systems as the short range repulsion is automatically built in. However, often the C_6 coefficient is chosen to closely resemble the dispersion coefficient. Fig. 6.2 shows the individual contributions of the ELJ terms for radon.

6.2. Three-body Potentials

6.2.1. Long Range Interactions

The contributions to the long-range interaction for three interacting atoms A, B and C can be found from the third-order term of the non-degenerate Rayleigh-Schrödinger perturbation expansion, $E^{(3)}(R_{ABC})$, which is given by [90]

$$E^{(3)}(R_{ABC}) = \sum_P \sum_{P'} \frac{\langle \Psi_0 | V(R_{ABC}) | \Psi_P \rangle \langle \Psi_P | V(R_{ABC}) | \Psi_{P'} \rangle \langle \Psi_{P'} | V(R_{ABC}) | \Psi_0 \rangle}{\Delta E_p \Delta E_{p'}} \tag{6.32}$$

where ΔE_p is the excitation energy from the ground to the excited state Ψ_P. Since the atomic forces are described by Coulomb interactions, the potential energy V is pairwise additive

$$V(R_{ABC}) = V(R_{AB}) + V(R_{BC}) + V(R_{CA}) \tag{6.33}$$

When substituting Eq. (6.33) into the the general expression for the third order dispersion, Eq. (6.32), one finds that the third order correction to the ground-state energy of the system can be decomposed into an additive and a non-additive contribution.

$$E^{(3)} = E_2^{(3)} + E_3^{(3)} \tag{6.34}$$

The first contribution consists of the three terms ($|\Psi_P\rangle = |P\rangle$)

$$E_2^{(3)} = \langle 0_A 0_B | V(R_{AB}) | p_A p_B \rangle \langle p_A p_B | V(R_{AB}) | p_A p_B \rangle \tag{6.35}$$

$$\langle p_A p_B | V(R_{AB}) | 0_A 0_B \rangle + \cdots \tag{6.36}$$

where $\cdots$ denotes the other two terms, for which potential $V(R_{AB})$ is interchanged for $V(R_{BC})$ and $V(R_{CA})$. These three terms can be derived by considering separately the perturbation for each individual pair AB of atoms by the appropriate electrostatic interaction $V(R_{AB})$, therefore this potential is additive.
The second contribution consists of six terms where all three pair interactions are coupled together.

$$E_3^{(3)} = \langle 0_A 0_B | V(R_{AB}) | p_A p_B \rangle \tag{6.37}$$

$$\langle p_B 0_C | V(R_{BC}) | 0_B p_C \rangle \langle p_A p_C | V(R_{CA}) | 0_C 0_A \rangle + \cdots \tag{6.38}$$

where $\cdots$ denotes the five other non additive terms, which can be obtained by permutation of the potentials.

With the aid of the bipolar expansion the third order correction to the energy can be written as [90]

$$E^{(3)} = \sum \{(l_1 l_2)^{(3)} + (l_1 l_2 l_3)^{(3)}\} \tag{6.39}$$

The $(l_1 l_2)$ and $(l_1 l_2 l_3)$ terms can be interpreted as arising from $2^{l_1}-$, $2^{l_2}-$ and $2^{l_3}-$pole moments, induced in the charge distributions of atoms 1,2 and 3 respectively. The non-additive dispersion term can be expressed in a simple form as

$$E_3^{(3)} = \sum_{l_1 l_2 l_3} Z_{l_1 l_2 l_3} W_{l_1 l_2 l_3}(R_{ABC}) \tag{6.40}$$

Where $W_{l_1 l_2 l_3}$ are geometrical factors depending purely on the relative positions of the three nuclei. The dispersion coefficients, $Z_{l_1 l_2 l_3}$, are interaction constants which depend solely on the atomic species involved in the interaction and can be, similarly as for the two-body dispersion, computed with the Casimir-Polder relation. For example, Thakkar [91] computed the coefficients $Z_{111}^{(3)}$, $Z_{112}^{(3)}$, $Z_{113}^{(3)}$, $Z_{122}^{(3)}$, $Z_{222}^{(3)}$ for the rare gases Ne, Ar, Kr and Xe. With the use of an extensive basis set and high level of theory these constants are assumed to be close to the exact values.

6.2.2. Short Range Interactions

The conventional asymptotic form of the non-additive triple-dipole energy ceases to be valid at small interatomic separations due to charge overlap and exchange effects. The three-body short-range interactions are expected to lead to an effective softening of the overall interaction. Therefore, for equilateral triangle and linear geometries the short range can be expressed as [92]

$$V^{(3)}(R_{AB}, R_{BC}, R_{CA}) = Ae^{-\alpha(R_{AB}+R_{BC}+R_{CA})} \tag{6.41}$$

and can be extended to a functional form that is capable of representing all geometries

$$\begin{aligned} V_{BM}^{(3)}(R_{AB}, R_{BC}, R_{CA}) = \sum_{k}^{K} A_{k_1 k_2 k_3} e^{\beta_{k_1 k_2 k_3}(R_{AB}+R_{BC}+R_{CA})} \\ \times \mathcal{P}(P_{k_1}(\cos\theta_1) P_{k_2}(\cos\theta_2) P_{k_3}(\cos\theta_3)) \end{aligned} \tag{6.42}$$

where θ_1, θ_2 and θ_3 refer to the interior angles formed by the sides R_{AB} and R_{AC}, R_{AB} and R_{BC} and R_{AC} and R_{BC} respectively. $\mathcal{P}$ represents the permutation operator that rotates the expression between all three angles. This exponential term is based on the analysis of the helium overlap repulsion calculations of Novaro [93]. The choice of this function was later motivated by Loubeyre in 1987 [94], who used Bruch's potential to study the three-body exchange interaction in compressed solid helium.

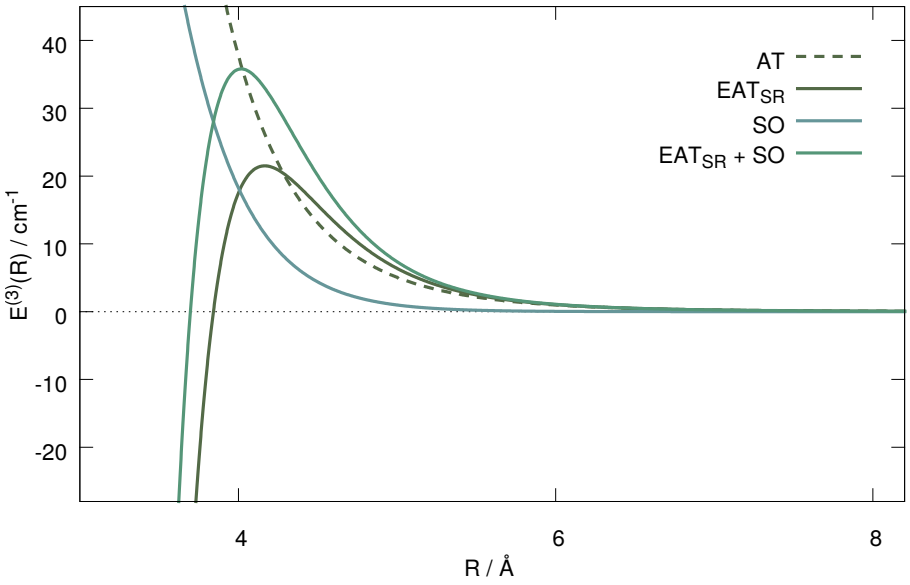

Figure 6.3.: The repulsive and attractive parts of the Extended Axilrod Teller potential for the radon trimer.

6.2.3. Functional Forms of the Three-body Potential

The functional forms of the three body potentials are based upon the perturbative expansion as discussed in section 6.2.1. Since the potentials now depend on three coordinates, instead of one, the functions quickly become computationally very demanding. Therefore, within our Monte Carlo simulation the Extended- Axilrod Teller potential will be employed, however more accurate potentials have been developed by Lotrich and Szalewicz. This highly accurate function is derived from symmetry adapted perturbation theory and although highly accurate, due to the many parameters obtaining a fit becomes very cumbersome and the complexity of the function makes it computationally extremely computer time consuming in simulations of the solid or liquid state.

The Axilrod-Teller Potential

The Axilrod-Teller potential [95] is the exact form of the triple-dipole interaction which is the dominant contribution of the three-body interaction in the dispersion region. It has the form

$$E^{(3)}_{ddd}(R_{AB}, R_{BC}, R_{CA}) = Z_{ddd} W^{(3)}_{111}(R_{AB}, R_{BC}, R_{CA}) \tag{6.43}$$

The geometrical factor $W_{111}^{(3)}$ is given by

$$W_{111}^{(3)}(R_{AB}, R_{BC}, R_{CA}) = 3R_{AB}^{-3}R_{BC}^{-3}R_{CA}^{-3}(1 + 3\cos\theta_1\cos\theta_2\cos\theta_3) \tag{6.44}$$

The sign of the AT energy is determined by the geometrical factor; the energy is positive if all the angles $\phi < 117^o$ and negative if at least one of the angles $\phi > 126^o$. The dispersion coefficient Z_{ddd} can be numerically derived using dipole polarizabilities or can be obtained from experimental data (for example [96] [97] [98] [99]) or set as a parameter and fitted to a set of ab-initio data points.
For an equilateral triangle ($\theta_1 = \theta_2 = \theta_3$, $R = R_{AB} = R_{BC} = R_{CA}$) the interaction energy simply becomes

$$E_{ddd}^{(3)}(R) = \frac{11}{8}\frac{C}{R^9} \tag{6.45}$$

The Extended Axilrod-Teller Potential

The long-range Axilrod-Teller potential deviates from the true three-body energy at short inter-atomic distances. A modified Axilrod-Teller potential was postulated by Bruch and McGee [92]

$$E_3^{EAT}(R_{AB},R_{BC}, R_{CA}) = f_\theta\left[ZR_g^{-9} - Ae^{-bR_s}\right] \tag{6.46}$$
$$\text{with} \quad f_\theta = (1 + 3\cos\theta_1\cos\theta_2\cos\theta_3),$$
$$R_g = (R_{AB}R_{BC}R_{CA})^{1/3} \quad \text{and} \quad R_s = R_{AB} + R_{BC} + R_{CA}$$

The first term of this equation is the Axilrod-Teller term, as given in the previous section. The second term represent the exchange Born-Mayer three-body interaction which at small inter-atomic distance describes the alterations of the charge densities of two interacting atoms by the presence of the third one.

This potential takes care of both attractive overlap effects in the short-range region and repulsive effects in the long-range of the three-body potential. Inclusion of the short range repulsive term is especially important for atomic clusters under high pressure, as for these systems the atoms are tightly packed. Neumann [100] showed that for helium the inclusion of this many-body short-range interaction brings path-integral Monte Carlo simulations in a better agreement with the kinetic and potential energies and the pressure of solid neon at room temperature. The calculations with the modified potential are in agreement with the experimental equation of state, whereas inclusion of an Axilrod-Teller dispersion term solely increases the pressure and worsens the agreement with experimental data.
In a similar fashion as for the extended Aziz potential, Schwerdtfeger [101] proposed to further extend Bruch's potential by multiplying the Born-Mayer

term with a polynomial such that we have

$$E_3^{EAT}(R_{AB},R_{BC},R_{CA}) \quad = f_\theta\big[c_0 R_g^{-9} + (c_1 + c_2 R_g^2 + c_3 R_g^4)e^{-\alpha R_s}\big] \tag{6.47}$$

This potential gives high-pressure equations of state for neon very close to experimental values [101].

Spin-Orbit Contributions For the heavier elements spin-orbit coupling become increasingly important beside the scalar relativistic effects. As ab-initio calculations including spin-orbit effects become computationally demanding for the three-body term, the spin-orbit effects are fitted by a separate function. The three-body contribution is repulsive and can be accurately reproduced by a fit to the simple function

$$E_{SO}^{(3)}(R_{AB},R_{BC},R_{CA}) = f_\theta(a + bR_g + (cR_g)^2)e^{-dR_s} \tag{6.48}$$

Fig. 6.3 shows the Axilrod-Teller, Extended Axilrod-Teller and Spin-Orbit contributions for the radon trimer.

7. Fitting Parameters

The point-wise obtained ab-initio two-body potential energy curve is fitted to the Extended Aziz (EA) potential and the computationally efficient Extended Lennard-Jones (ELJ) potential. For the three-body interactions we limit ourselves to a fit to the Axilrod-Teller and Extended Axilrod-Teller potentials. Here we describe the fitting procedure and list the resulting parameters.

7.1. Two-body Potential Parameters

7.1.1. Extended Aziz Potential

As shown in section 6.1.3, the Extended Aziz potential separates the short-range repulsive interaction from the long-range attractive interaction and has the chosen form

$$E_{EA}^{(2)}(r) = (a + br)e^{-A_1 r + A_2 r^2 + A_3/r + A_4/r^2} + \sum_{n=3}^{8} f_{2n}(r)\frac{C_{2n}}{r^{2n}} \tag{7.1}$$

where r is the internuclear distance. The short range is described by the exponential Born-Mayer type potential with fitting parameters a, b, A_1, A_2, A_3 and A_4 The second part of the potential describes the dispersion, with fitting parameters C_6, C_8 and C_{10} which is damped by the universal Tang-Toennies damping function

$$f_{2n}(r) = 1 - \left[\sum_{k=0}^{2n} \frac{(\alpha r)^k}{k!}\right] e^{-\alpha r} \tag{7.2}$$

with fitting parameter α.

The higher order dispersion coefficients, C_{12}, C_{14} and C_{16} are estimated with the semi-empirical recurrence relation [88, 102]

$$C_{2n} = C_{2n-6}\frac{C_{2n-2}}{C_{2n-4}} \tag{7.3}$$

Although the C_6 coefficient is a fitting parameter, we choose to fix this coefficient to a predetermined value. Since in the long range the potential is primarily described by the part of the potential with the smallest inverse power, this assures that the long range is described properly.

While holding the C_6 coefficient fixed, the dispersive region of the potential is fitted to the coefficients C_8, C_{10} and the damping coefficient α. The fitting parameters are found iteratively; while holding two parameters fixed, the third is obtained by a least squares fit. This iterative fitting routine is carried out multiple times after which the fitting coefficients of the repulsive Born-Mayer part of the Extended Aziz function are obtained by a least squares fit to the remaining values of the potential. The fitting coefficients for xenon and radon are listed in table 7.2.

7.1.2. Extended Lennard Jones Potential

The Extended Lennard Jones potential is of the form

$$E^{(2)}_{ELJ}(r) = \sum_{n\geq 6} \frac{C_n}{r^n} \tag{7.4}$$

with fitting parameters C_n. During the ELJ fitting procedure the C_6^{ELJ} coefficient is held fixed to the C_6^{EA} dispersion coefficient. This term is dominant in the long range and therefore fixing the C_6 parameter to this value assures a correct dispersive behavior. The C_7 coefficient is the next most dominant term. To assure that the long range is described solely by the attractive C_6/r^6 part of the potential, this coefficient is excluded form the ELJ potential. Note that, except for the C_6 coefficients, the coefficients in the ELJ potential contain both contributions from the attractive long-range and repulsive short-range part, and are therefore not related to the usual long-range dispersion coefficients. The fitting parameters are listed in table 7.1, 7.3 and 7.4,

7.1.3. Value of the C_6 Parameter

The ELJ parameters of krypton were obtained by a least-squares fit to the ab-initio two body potential calculated by Jäger [47] in the range of 3 to 12 Angstrom. The C_6 parameter is fixed to the C_6 dispersion coefficient obtained by Jäger who fitted the ab-initio potential to the modified Tang-Toennis type analytical function, which is similar to our extended Aziz function. The value of the C_6 dispersion coefficient is in agreement with the ab-initio values of $C_6 = 129.601$ a.u. and $C_6 = 126.792$ a.u., obtained by Waldrop [103] and Kumar [104], respectively.

For xenon, we set the C_6 coefficient to the experimentally derived C_6^{exp} value, which we obtain by adjusting the theoretically determined van der Waals coefficient, C_6^{theor} by the squared ratio of measured and computed polarisabilities, α^{exp} and α^{theor}

$$C_6^{exp} = C_6^{theor}\left(\frac{\alpha^{exp}}{\alpha^{theor}}\right)^2 \tag{7.5}$$

with, $C_6^{theor} = 287.5$ a.u. [98], $\alpha^{exp} = 27.815$ a.u.[105], and $\alpha^{theor} = 27.16$ a.u. (from [98], Table 1; S_k with $k = -1$). For the ELJ fitting procedure we allowed the C_6 coefficients to vary.

For the exotic elements radon and oganesson there are no recorded values in the literature of the C_6 coefficients. Hence, the C_6 dispersion coefficients of radon and oganesson are obtained by a fit to the far dispersive region as depicted for radon in Fig. 7.1.

Table 7.1.: Fitting parameters for the two-body ELJ krypton interaction energy. All potential parameters are given in atomic units.

	ELJ
C_6	-129.6833350939
C_8	14396.540458296
C_{10}	-4832182.6712422
C_{12}	377094256.797685
C_{14}	-9898188811.65233
C_{16}	89310447556.1652

Table 7.2.: Fitting parameters for the two-body EA potential for Xenon and Radon. All potential parameters are given in atomic units.

EAziz	Xe	Rn SR	Rn SR+X2C
C_6	301.5341093410077	424.6525348786	447.5748304291
C_8	10120.702848842004	16027.5308704127	18591.48791214
C_{10}	528135.5699104187	885677.621776292	1057578.34267109
c	1.0967311741145045	1.04297043975239	1.06929085585087
A_1	0.17492296052109577	-0.167545030524813	-0.463524679624738
A_2	-0.1384774059626884	-0.0763867426579562	-0.05764585930506
A_{-1}	-1.5944711447872206	5.19321102567466	3.49114206994604
A_{-2}	-1.620886067478606	7.02047025369425	4.48271517525371
a	-3.125937679977943	1.31426576783988	5.56565274012015
b	2.1841291883673795	-0.132467673137129	-0.549626158605542

Table 7.3.: Potential parameters for the xenon and radon dimer obtained from a fit of the ab-initio data to the ELJ potential. All potential parameters are given in atomic units.

ELJ	Xenon	Radon SR	Radon SR + X2C
C_6	-301.700000000000	-424.6525348786	-447.5748304291
C_8	-26816.4020712100	-8417220.92556745	-28314888.291503303
C_9	-29141425.4118978	659034029.258425	2524583758.700001
C_{10}	2525729440.60837	-22627158551.1357	-98236154678.43843
C_{11}	-93157553751.1815	447229392384.169	2189549802269.0093
C_{12}	1958061699137.66	-5607035210687.55	-30816973086110.53
C_{13}	-25959609531187.9	46142864081981.3	2841055606917376
C_{14}	225015902487099	-248588239685682	-1716353459038699
C_{15}	-1272921381781360	84388699602227	6556775983296994
C_{16}	4526862108942420	-1636947370010659	-14385785954864606
C_{17}	-9182845674164360	1382704803541692	13824897857732292
C_{18}	8100817151233590		

Table 7.4.: Fitting parameters for the oganesson dimer obtained from a fit of ab initio data for the ELJ functional form. Potential parameters C_n are given in atomic units.

ELJ	Og NR	Og SR	Og SR + X2C
C_6	-710.7031383523	-677.9908488582	-888.8466527976
C_8	-19713279.1888082	-1664638.505207	-4384901.20047962
C_9	1896030459.13112	149627425.358945	398569373.906809
C_{10}	-79842070963.2586	-6518341586.1836	-16601910672.3166
C_{11}	1927450385963.25	169557328373.934	405890768350.34
C_{12}	-29360865855330.7	-2791160884405.93	-6319994266579.97
C_{13}	292279348044922	29491541333967.4	64188295958813
C_{14}	-1900374348813550	-198476802969030	-422348243579330
C_{15}	7787445871057110	821314815244948	1733252497487270
C_{16}	-18278401671546700	-1905073205098960	-4030954412971440
C_{17}	18758678463993000	1897306326828080	4057926164803740

Table 7.5.: Equilibrium bond distance in Å, dissociation energy in cm^{-1} and root-mean-square error (RMSE) for the rare gas dimers of the original data, the extended Lennard-Jones (ELJ) and the extended Aziz (EA) potential fits.

		Data	ELJ	EA
Kr				
	r_e	4.0169	4.01634	4.015802[47]
	D_e	139.627	139.320	139.614[47]
	RMSE		$2.73 \cdot 10^{-6}$	
Xe				
	r_e	4.3617	4.3616	4.347
	D_e	196.30	196.27	195.726
	RMSE		$9.32 \cdot 10^{-7}$	$9.3 \cdot 10^{-6}$
Rn SR				
	r_e	4.462	4.456	4.452
	D_e	245.47	245.07	245.58
	RMSE		$2.73 \cdot 10^{-6}$	$3.37 \cdot 10^{-5}$
Rn SR+X2C				
	r_e	4.4420	4.4405	4.4330
	D_e	266.09	266.20	266.07
	RMSE		$9.17 \cdot 10^{-9}$	$5.49 \cdot 10^{-5}$
Og NR				
	r_e	4.88591	4.8871	–
	D_e	263.976	264.029	–
	RMSE		$3.81 \cdot 10^{-7}$	–
Og SR				
	r_e	4.49413	4.49236	–
	D_e	366.358	366.317	–
	RMSE		$4.94 \cdot 10^{-7}$	–
Og SR + X2C				
	r_e	4.31508	4.31381	–
	D_e	626.290	626.296	–
	RMSE		$3.73 \cdot 10^{-7}$	–

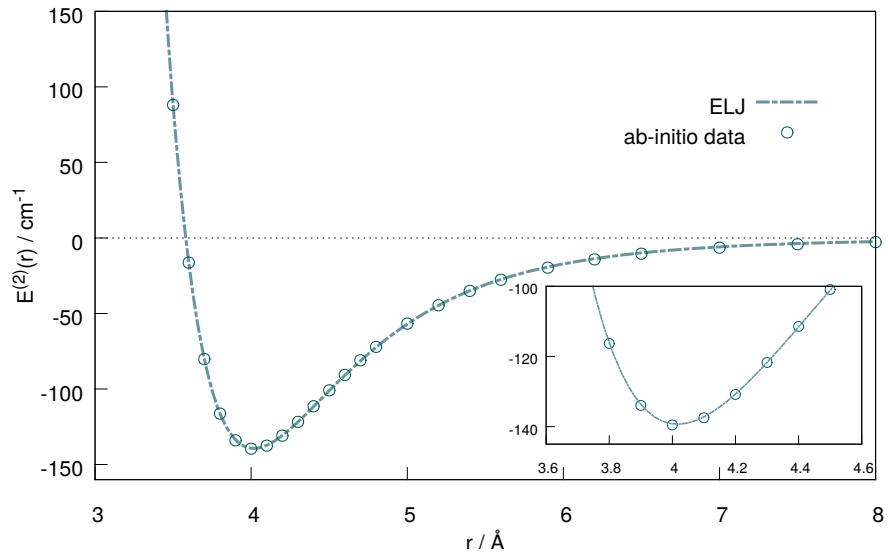

Figure 7.2.: Coupled cluster two-body potential energy curves for Kr_2 fitted to the ELJ potential.

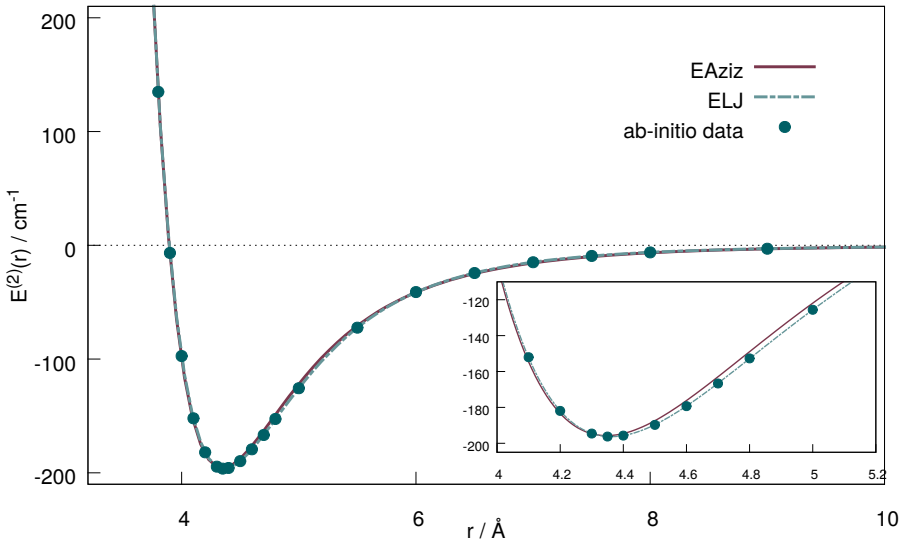

Figure 7.3.: Coupled cluster two-body potential energy curves for Xe_2 fitted to the EA and ELJ potential.

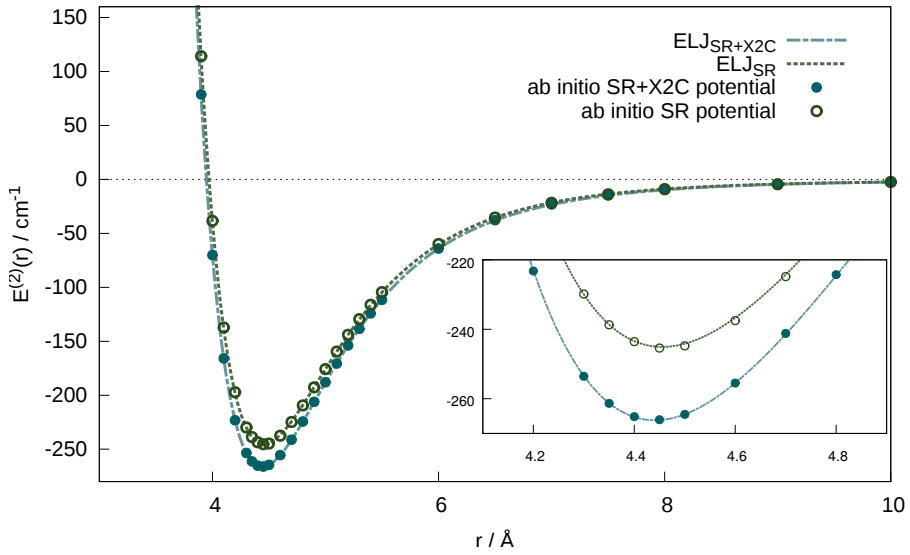

Figure 7.4.: bla bla Coupled cluster two-body potential energy curves for Rn_2, at the non-relativistic (ELJ_{NR}) and fully relativistic (ELJ_{R+X2C}) level of theory.

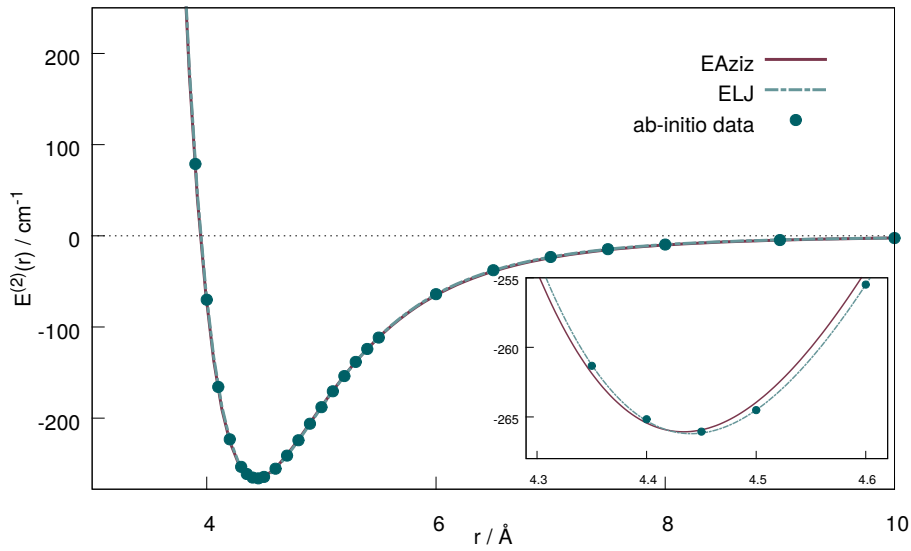

Figure 7.5.: Coupled cluster two-body potential energy curves for fully relativistic Rn_2 fitted to the EA and ELJ potential.

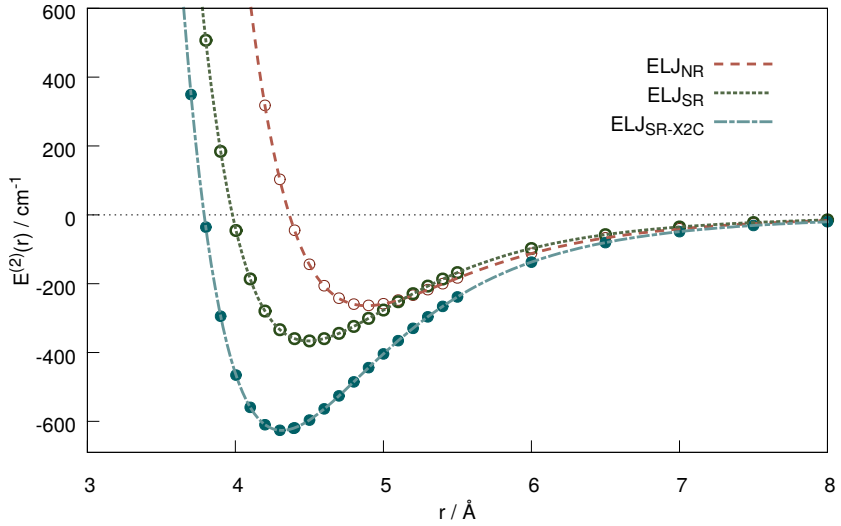

Figure 7.6.: Coupled cluster two-body potential energy curves for Og_2 fitted to the ELJ potential, at non relativistic (ELJ_{NR}), scalar relativistic (ELJ_{SR}) and fully relativistic (ELJ_{SR+X2C}) level of theory.

7.2. Three-body Potentials

The non-relativistic and scalar relativistic energy curves were fitted to the extended Axilrod-Teller (EAT) potential which accounts for short range repulsion as well as long-range dispersive attraction

$$\begin{aligned} E^{(3)}_{EAT}(r_{ijk}) =& f_\theta[C_{EAT} r_g^{-9} \\ &+ (B_0 + B_2 r_g^2 + B_4 r_g^4 + B_6 r_g^6) e^{-\alpha r_s}] \end{aligned} \tag{7.6}$$

with

$$f_\theta = (1 + 2\cos\theta_i \cos\theta_j \cos\theta_k), \qquad r_g = (r_{ij} r_{jk} r_{ik})^{1/3} \tag{7.7}$$

and

$$r_s = r_{ij} + r_{jk} + r_{ik} \tag{7.8}$$

and $r_{ij} = |\vec{r}_{ij}|$ being the distance between two atoms i and j and θ_i the corresponding angle between the vectors $\vec{r}_{ij}$ and $\vec{r}_{ik}$.

The computed spin-orbit contributions are fitted to the exponential form

$$E^{(3)}_{SO}(r_{ijk}) = f_\theta (a + b r_g + c r_g^2) e^{-d r_s} \tag{7.9}$$

with fitting parameters a, b, c and d, such that the total 3-body potential is described by

$$E^{(3)}(r_{ijk}) = E^{(3)}_{EAT}(r_{ijk}) + E^{(3)}_{SO}(r_{ijk}) \tag{7.10}$$

The fitting parameters of krypton, radon and oganesson were obtained by a least squares fit over 40 equilateral distances.
For xenon however, 300 trimer geometries were chosen to represent the most important points on the potential energy surface, according to the method as proposed by Cencek [106]. The C_{EAT} parameter is obtained by a least squares fit over the long-range equilateral ab-initio data points. The value of C_{EAT} is then held fixed and a new fit is obtained by a least squares fit to 300 ab-initio energies spanning also the non-equilateral region of space. The fitting coefficients are listed in table 7.6 and 7.7.

We also list the fitting coefficients of the simple Axilrod-Teller potential

$$E^{(3)}_{AT}(r_{ijk}) = f_\theta C_{AT} r_g^{-9} \tag{7.11}$$

of which the triple-dipole parameter C_{AT} is obtained by a fit to the data-point beyond the equilateral maximum. The fitting parameters C_{AT} are in good agreement with the theoretically obtained value of 1577 a.u. for krypton and 5573 a.u. for xenon, obtained by Kumar [98] and Tang [99] respectively. Figs. 7.7,7.8,7.9 and 7.10 show the ab-initio potentials and fitted AT and EAT functions.

Table 7.6.: Fitting parameters of the three-body extended Axilrod-Teller potential for krypton, xenon and radon. Parameters are given in a.u.

	Kr	Xe	Rn
C_{AT}	1725.79115641033	4544.70040639368	10075.9005005051
C_{EAT}	1606.77610926838	3471.93012715399	7782.99951402124
A_0	60036.9547561167	886.992268260218	-115686.644728068
A_2	-3670.25288702589	-132.687520259295	8636.78510713189
A_4	25.6338653669989	3.14321647514269	-256.235463339275
A_6	0.30585091087561	-0.01977876625979	2.31046375844624
α	0.98918853451850	0.68379059500687	0.87495898039468
a			-98.7812728919394
b			20.6273124059537
c			
d			0.6067818863

Table 7.7.: Fitting parameters of the three-body extended Axilrod-Teller potential for oganesson. Parameters are given in a.u.

Og	NR	SR	SR+SO
C_{AT}	23479.5437556554	17636.5795696874	17636.5795696874
C_{EAT}	29116.0029397717	15503.5089404812	15503.5089404812
A_0	-4229099.3524061	-4234453.0426502	-4234453.0426502
A_2	163825.251233113	256154.448379476	256154.448379476
A_4	390.1484625755	-5360.476974414	-5360.476974414
A_6	-81.0117068964	37.2407198038	37.2407198038
α	0.9946175572	0.933701141	0.933701141
a			7.9691187697
b			-1.1228026472
c			0.0393422448
d			0.3499380784

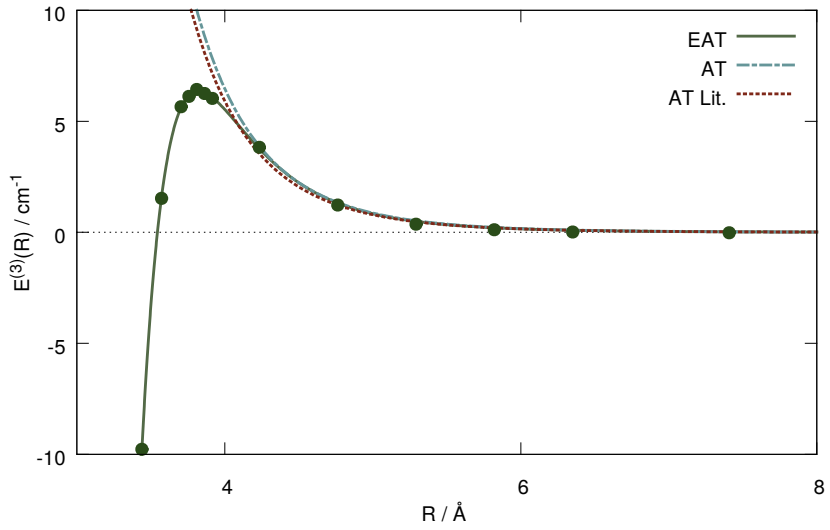

Figure 7.7.: Coupled cluster three-body potential energy curves for Kr_3 kept in D_{3h} symmetry ($R = r_{ij} = r_{ik} = r_{jk}$). Literature value of the Z_{111} triple-dipole coefficients is taken from Kumar [98].

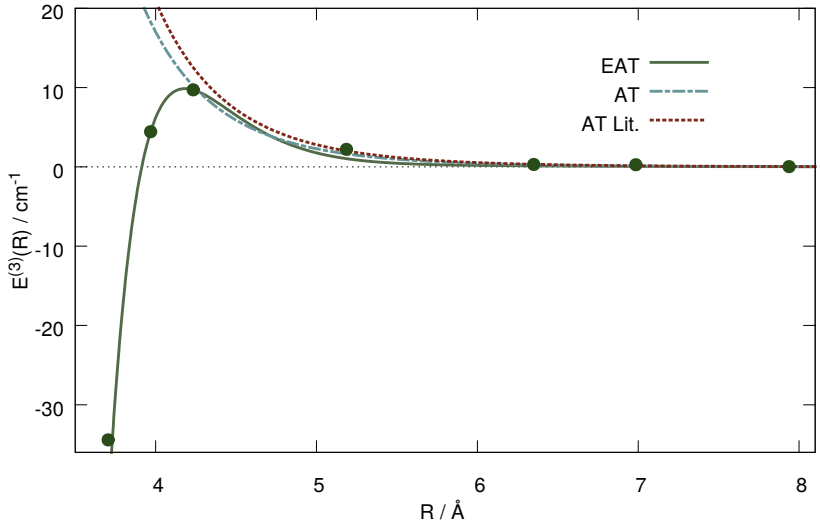

Figure 7.8.: Coupled cluster three-body potential energy curves for Xe_3 kept in D_{3h} symmetry ($R = r_{ij} = r_{ik} = r_{jk}$). Literature value of the Z_{111} triple-dipole coefficients is taken from Tang [99].

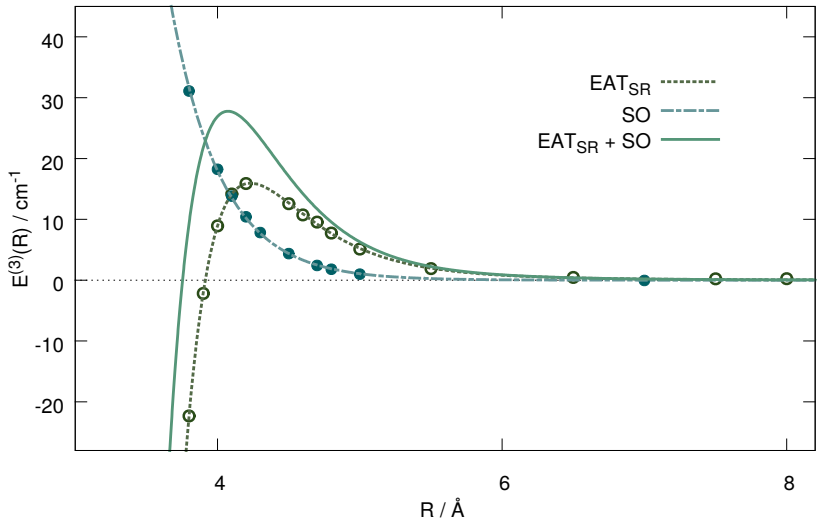

Figure 7.9.: Coupled cluster three-body potential energy curves for Rn_3 kept in D_{3h} symmetry ($R = r_{ij} = r_{ik} = r_{jk}$).

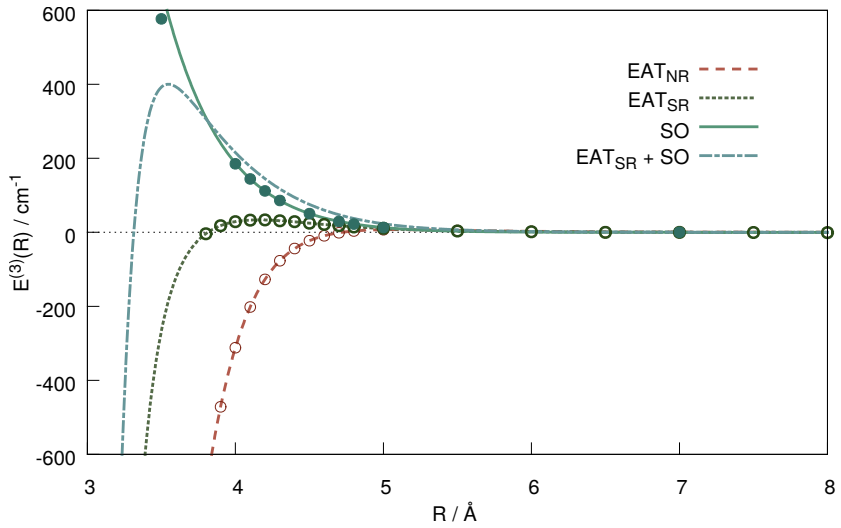

Figure 7.10.: Coupled cluster three-body potential energy curves for Og_3 kept in D_{3h} symmetry ($R = r_{ij} = r_{ik} = r_{jk}$).

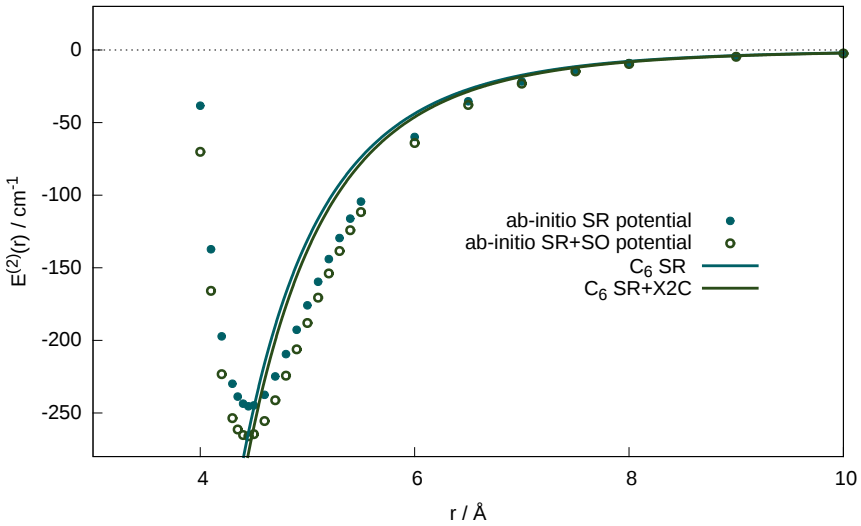

Figure 7.1.: C_6 dispersion parameters obtained by a fit to the far dispersive region of the ab-initio potential of radon.

8. Spectroscopic Constants

8.1. Theory

Within the Born-Oppenheimer approximation, the motion of the diatomic molecule, in a given electronic state, is described by the wavefunction $\Psi_{\nu JK}$ and energy $E_{\nu J}$ which are the eigenfunction and eigenvalue of the radial Schrödinger equation respectively (The K-dependency of rotational levels is considered by the wavefunction $\psi_{\nu JK}$)

$$\left[-\frac{\hbar^2}{2\mu}\frac{\mathrm{d}^2}{\mathrm{d}r^2} + \frac{\hbar^2 J(J+1)}{2\mu r^2} - E_{\nu J} + U(r) \right] \psi_{\nu J}(r) = 0 \tag{8.1}$$

with J being the rotational quantum number, r the internuclear distance with μ the reduced mass, $\mu = \frac{m_1 m_2}{m_1+m_2}$ with m_1 and m_2 the masses of atom 1 and 2, and $U(r)$ the internuclear potential.
One of the methods to determine the energy eigenvalues $E_{\nu J}$ is by the Dunham approach [107] in which the potential is assumed to be a power series of the instantaneous reduced displacement from the equilibrium $x = (r - r_0)/r_0$. By applying the Wentzel-Brillouin-Kramers method, the eigenvalues take the form of a series of vibration and rotation quantum numbers

$$E_{\nu,J} = \sum_{lm} Y_{lm} (\nu + \frac{1}{2})^l J^m (J+1)^m \tag{8.2}$$

The terms of the Dunham series give rise to rotational and vibrational energy terms as well as terms that account for the interaction between vibrational and rotational motion

$$\begin{aligned} E_{\nu,J} = & Y_{1,0}\,(\nu + \frac{1}{2}) + Y_{2,0}\,(\nu + \frac{1}{2})^2 + \dots \\ & + Y_{0,1}\,J(J+1) + Y_{0,2}\,J^2(J+1)^2 + \dots \\ & + Y_{1,1}\,(\nu + \frac{1}{2})\,J(J+1) + \dots \end{aligned} \tag{8.3}$$

$Y_{i,j}$ are referred to as spectroscopic constants. The energy terms can be seperated into three components

$$E_{\nu,J} = \Delta E_{vib} + \Delta E_{rot} + \Delta E_{vib/rot} \tag{8.4}$$

where the leading order vibrational terms are given by

$$\begin{aligned} Y_{1,0} &= \omega_e && \text{harmonic vibrational frequency} \\ Y_{2,0} &= -\omega_e x_e && \text{anharmonic vibrational frequency} \\ Y_{3,0} &= \omega_e y_e && \text{second anharmonic vibrational frequency} \end{aligned}$$

(note the negative sign in $-\omega_e x_e$ is by convention) and the leading order rotational terms are

$$\begin{aligned} Y_{0,1} &= B_e && \text{rotational constant} \\ Y_{0,2} &= -D_{ele} && \text{centrifugal distortion} \end{aligned}$$

and the leading order term that account for the interaction between vibrational and rotational motion

$$Y_{1,1} = -\alpha_e \qquad \text{rotational/vibrational coupling}$$

Transitions between vibrational states can be measured by their absorption or emission spectra, which corresponds to

$$\hbar\omega = E_f - E_i = E_{\nu_f, J_f} - E_{\nu_i, J_i} \tag{8.5}$$

These vibrational transitions can be experimentally measured up to high accuracy of which the spectroscopic constants can be deducted. The spectroscopic constants are thus a convenient quantity to compare between the calculated ab-initio potential energy and the experimental results. The spectroscopic constants of most diatomic molecules can be found in [108].

8.2. Spectroscopic Constants of Xenon, Radon and Oganesson

A finely spaced grid is generated to obtain rovibrational spectroscopic constants for the Dunham series with the Vibrot module of the Molcas 8.0 program package. This package solves the vibrational-rotational Schrödinger equation numerically. 18 vibrational and 12 rotational levels were included in the analysis, which results in spectroscopic constants which are stable with slight variation in the number of vibrational/rotational levels. Table 8.1 and 8.2 list the vibrational-rotational spectroscopic constants for the xenon, radon and oganesson dimers.

Xenon Considering the uncertainties in the experimental data we see excellent agreement with the experiment of Freeman et al. [109] and Wuest et al. [110]. Except perhaps for the bond distance derived by Wuest et al.,

which is 0.015 Å longer than our calculated value of 4.3617 and that of Freeman et al. (4.361 Å). However, our dissociation energy (196.0 cm^{-1}) agrees extremely well with both available experimental values (195.5 and 196.1 cm^1, respectively). Looking at the most recent theoretical results for the xenon dimer we can compare to the distances and dissociation energies of Hanni et al. ($R_e = 4.382$, D_e =196.84 cm^{-1}) using a scalar relativistic effective core potential (RECP) within a CCSD(T) procedure [111], two-component RECP CCSD(T) calculations by Tu et al. ($R_e = 4.342$ D_e = 221.89 cm^{-1}) [112], or exact two-component CCSD(T) calculations by Shee et al. ($R_e = 4.346$, D_e= 208.69 cm^{-1})[113]. Calculating the potential without consideration of spin-orbit interactions (i.e. only utilising scalar relativistic effects through DKH2), we find the minimum at $R_e = 4.3610$ with D_e = 195.4 cm^{-1} . For the xenon dimer, spin-orbit interactions lead to a slightly longer equilibrium distance and a higher dissociation energy.

Radon Relativistic coupled cluster calculations for the radon dimer give a bond distance of $r_e = 4.441$ Å, a dissociation energy of D_e = 266.2 cm^{-1}, and a harmonic vibrational frequency of ω_e = 19.9 cm^{-1} with an anharmonic correction of $\omega_e x_e = 0.46$ cm^{-1}. These values should be regarded as the most accurate currently available, and an improvement over previously published values [113]. Spin-orbit effects are already sizeable for Rn_2, that is at the scalar relativistic level we have a longer bond distance of r_e = 4.455 , and a smaller dissociation energy of D_e = 245.1 cm^{-1} .

Oganesson For oganesson, the total relativistic bond contraction with $\Delta_{\mathrm{R}} r_e = -0.573$ Å is extremely large. This implies that the Og_2 bond distance is shorter than that for Rn_2 and even for Xe_2 due to strong relativistic effects. Further, our results are the most accurate so far, and are close to the CCSD(T) results by Saue and co-workers [114, 115], but much shorter than the pseudopotential results by Nash who reports a value of 4.57 Å [116]. Saue and co-workers already pointed out the Og_2 has a rather high dissociation energy [114, 115]. We can now confirm that this is due to relativistic effects, i.e. scalar relativistic effects increase the dissociation energy by $\Delta_{\mathrm{SR}} D_e$= 102 cm^{-1} (38 % compared to the nonrelativistic value) and further by $\Delta_{\mathrm{SR+X2C}} D_e$= 261 cm^{-1} (71 % compared to the scalar relativistic value) due to spin-orbit effects. This is paralleled by a strong relativistic increase in the vibrational frequency, which is in itself however very small because of the large Og mass.

Table 8.1.: Spectroscopic constants for the electronic ground state of $^{132}Xe_2$ dimer calculated with the extended Lennard-Jones potential (ELJ) and the extended Aziz (EA) potential. Bond distance r_e is given in Å, dissociation energy D_e in cm^{-1} (not corrected for zero-point vibration), harmonic vibrational frequency ω_e in cm^{-1}, anharmonic vibration constants $\omega_e x_e$ and $\omega_e y_e$ in cm^{-1}, vibrational/rotational coupling constant α_e in cm^{-1}, rotational constant B_e in cm^{-1}, and centrifugal distortion constant D_{ele} in cm^{-1}.

	ELJ	EA	Exp.
r_e	4.3617	4.3623	4.361[117]
D_e	196.0	196.0	195.5 $\pm$ 3.0[117]
ω_e	21.06	21.06	21.12[117]
$\omega_e x_e$	0.6593	0.6605	0.65[117]
$\omega_e y_e$	0.00438	0.00437	0.003[117]
α_e	0.000251	0.000246	0.000302 (33)[118]
B_e	0.013182	0.013179	0.013495 (30)[118]
E_{ele}	0.0000046	0.0000049	

Table 8.2.: Spectroscopic constants for the electronic ground state of the $^{211}Rn_2$ and $^{294}Og_2$ dimers calculated for both extended Lennard-Jones potential (ELJ) and the extended Aziz (EA) potential. The mass of 222.0175777(25) u for 222-Rn has been used. Bond distance r_e is given in Å, dissociation energy D_e in cm^{-1} (not corrected for zero-point vibration), harmonic vibrational frequency ω_e in cm^{-1}, anharmonic vibration constants $\omega_e x_e$ and $\omega_e y_e$ in cm^{-1}, vibrational/rotational coupling constant α_e in cm^{-1}, rotational constant B_e in cm^{-1}, and centrifugal distortion constant D_{ele} in cm^{-1}.

	Rn ELJ	Rn EA	Og NR	Og SR	Og SR+X2C
r_e	4.4405	4.4330	4.8871	4.4923	4.3137
D_e	266.21	266.07	264.55	366.17	626.69
ω_e	19.94	19.95	14.54	17.41	22.39
$\omega_e x_e$	0.4624	0.4690	0.2262	0.2190	0.2132
$\omega_e y_e$	0.00294	0.00314	5.7×10^{-4}	4.9×10^{-4}	1.7×10^{-4}
α_e	0.002153	0.002049	3.6×10^{-5}	1.37×10^{-4}	1.80×10^{-4}
B_e	0.024167	0.009262	4.661×10^{-3}	6.001×10^{-3}	7.091×10^{-3}
E_{ele}	0.0000258	0.0000422	1.9×10^{-9}	2.9×10^{-9}	2.8×10^{-9}

Part III.

Simulating Melting

9. Thermodynamics of Melting

In the previous chapter we derived the functions that describe the interaction between noble gas atoms. This leaves us with three important aspects that need to be considered before we can determine the melting temperature. First, the statistics that determines the probability distribution needs to be known. Secondly, we need to be able to recognize the melting transition, or alternatively we need to know the properties that distinguish a solid from a liquid phase. And finally, a method (algorithm) for simulating the atom dynamics such that we can obtain the melting temperature needs to be formulated. These three aspects will be discussed in detail. In section 9.1 the relevant statistical ensembles and their properties is given. Section 9.2 discussed the characteristics of melting as a first order phase transition. Section 9.3 gives an overview of the different simulation methods.

9.1. Statistical Ensembles

For the Monte Carlo simulations we are interested in the both the canonical and the isobaric isothermal ensemble. Let us briefly recall the two ensembles.

9.1.1. Canonical Ensemble

The canonical ensemble is the statistical ensemble that represents the possible states of a mechanical system in thermal equilibrium with a thermal reservoir at a fixed temperature T. The system and reservoir are in contact through a diathermal but fixed an impermeable wall. This means that in the canonical ensemble all energies are allowed but the particle number N, temperature T and volume V are held constant. In the classical continuous limit, the canonical phase density is given by

$$\rho_c(q_v, p_v) = \frac{\exp\{-\beta\mathcal{H}(q_v, p_v)\}}{\frac{1}{h^{3N}} \int d^{3N}q d^{3N}p \exp\{-\beta\mathcal{H}(q_v, p_v)\}} \tag{9.1}$$

where $\mathcal{H}(q_v, p_v)$ is the (classical or quantum mechanical) Hamiltonian of system at absolute temperature $T = 1/(k_B\beta)$. For indistinguishable particles, the density needs to be multiplied by the Gibbs correction factor of $1/N!$. h^{3N} corresponds to a volume in classical phase space for every N-particle quantum state. The denominator is introduced such that the probability is

normalized to 1, $\int \rho_c(q_v, p_v) = 1$, where the integral $\int$ extends over all states. By introducing the *canonical partition function*

$$Z_{NVT} = \frac{1}{h^{3N}} \int d^{3N}q d^{3N}p \exp\{-\beta \mathcal{H}(q_v, p_v)\} \tag{9.2}$$

the canonical phase density can be written as

$$\rho_c(q_v, p_v) = \frac{\exp\{-\beta \mathcal{H}(q_v, p_v)\}}{Z_{NVT}} \tag{9.3}$$

The average of an observable O is given by

$$\langle O \rangle_\beta = \frac{\int dr^{3N} O(r^{3N}) \exp\{-\beta \mathcal{H}(p_v)\}}{\int dr^{3N} \exp\{-\beta H(p_v)\}} \tag{9.4}$$

Since the dependence on the partition function factorizes into a product of kinetic and potential parts and our system does not have a kinetic component, the kinetic contribution simply cancels out.

In the discrete notation, $(p_v) \rightarrow i$ and $1/h^{3N} \int d^{3n}p \rightarrow \sum_i$, the probability p_i of finding the system in a certain micro state i with the energy E_i corresponds to

$$p_i = \frac{\exp\{-\beta E_i\}}{\sum_i \exp\{-\beta E_i\}} \tag{9.5}$$

and the partition function becomes

$$Z = \sum_i \exp\{-\beta E_i\} \tag{9.6}$$

An ensemble average of an observable O is given by

$$\langle O \rangle = \frac{\sum_i O e^{-\beta E_i}}{\sum_i e^{-\beta E_i}} \tag{9.7}$$

9.1.2. Isobaric Isothermal Ensemble

The isobaric-isothermal ensemble is a statistical ensemble that maintains constant temperature T and constant pressure P, whereas the size of the system is allowed to fluctuate. With also the number of particles held constant, this is called the NPT ensemble. Intuitively the partition function of the NPT ensemble is written as an extension of the NVT ensemble

$$Z_{NPT} = \frac{1}{\nu} \int_0^\infty dV e^{-\beta PV} Z_{NVT} \tag{9.8}$$

It is however not easy to specify the volume and multiple attempts have been made to properly define the partition function in the NPT ensemble. Problems arise because one can not 'count' volume and attempts made, by for

example by Attard [119] and Koper and Reiss [120], lead to different expressions for the partition function. In this work we adapt the expression for the partition function as discussed in Meijer and Frenkel [121]. The partition function of the system is derived as if the system of volume V resides inside a larger system with volume V_0. Mechanical coupling allows the volume of the system to change such that the pressure in the system is the same as the reservoir. The partition function can now be written as the product of the partition function of the constituent subsystems after which the ratio between the two systems is taken to be $V/V_0 \to 0$. According to this approximation the partition function for the constant NPT ensemble is formulated as the weighted sum of the partition function of the canonical NVT ensemble

$$Z_{NPT} = c \int dV V^N \exp(-\beta PV) \int dr^N \exp\big(\beta U(r^N)\big) \tag{9.9}$$

where c is a normalizing factor. The probability density to find the system in a particular configuration of N atoms (given in reduced coordinates) at a given volume V is given by

$$\rho_v = \frac{V^N \exp(-\beta PV) \int d\mathbf{s}^N \exp\big[-\beta U(\mathbf{s}^N; L)\big]}{Z_{NPT}} \tag{9.10}$$

9.1.3. Thermodynamic Properties

Here we give a brief summation of important thermodynamic properties that will be used throughout this thesis.

Internal Energy With E_i being the total energy of a system of micro state i, the internal energy U is defined as the statistical mean value of energies E_i

$$U = \langle E \rangle := \sum_i p_i E_i \tag{9.11}$$

Enthalpy For thermodynamic systems which are allowed to change pressure or volume an important property is the enthalpy. Enthalpy is the thermodynamic quantity equivalent to the internal energy of the system plus the product of pressure and volume.

$$H = U + PV \tag{9.12}$$

Entropy The definition of entropy is

$$S = k_B \ln \Omega \tag{9.13}$$

where Ω is the number of accessible microscopic states of the system. The entropy can also be expressed in terms of the state probabilities

$$\begin{aligned} S &= -k \sum_j p_j \ln p_j \\ &= -k \langle \ln p_j \rangle \end{aligned} \tag{9.14}$$

Free Energy In the canonical ensemble the probability of finding the system in micro state E_j is given by

$$p_j = \frac{e^{-\beta E_j}}{Z} \tag{9.15}$$

This quantity can be reformulated as

$$\ln p_j + \ln Z = -\beta E_j \tag{9.16}$$

Combining the above equation with Eq. (9.14) gives the definition for the Helmholtz free energy

$$F \equiv U - TS = -kT \ln Z \tag{9.17}$$

For the isobaric-isothermal ensemble one can derive the **Gibbs free energy**

$$G = U + PV - TS \tag{9.18}$$

Heat Capacity The heat capacity at constant volume is defined as

$$C_v(T) = \left. \frac{\partial U}{\partial T} \right|_V \tag{9.19}$$

and the heat capacity at constant pressure is given by

$$C_p(T) = \left. \frac{\partial H}{\partial T} \right|_P \tag{9.20}$$

9.2. Identifying the Melting Temperature

Melting is a fundamental process in which a crystal undergoes a phase transition from a solid (ordered) state to a liquid (disordered to a certain extent) state. Fundamentally understanding the processes of melting has proven to be a difficult task as many theories have been developed during the past century, resulting in a range of different frameworks that tackle the problem of melting from different perspectives.

The melting point can be easily identified by the pair distribution function, $g(r, \beta)$, which gives the probability of finding a pair of atoms at a distance

r apart for given inverse temperature β. Structural arrangements are characterized by well defined peaks in the pair distribution due to the symmetry. Upon melting the order in the system disappears, the peaks in $g(r, \beta)$ broaden, and a phase transition is therefore easily recognizable upon inspection of the pair distribution function. Although the pair distribution function provide a method to identify the melting transition, it fails to theorize the fundamental cause of the melting transition.

Lindemann [122] proposed that the phase transition occurs at the temperature at which the amplitude of atomic thermal vibrations reaches a characteristic value. At this point melting is triggered by a mechanical instability, causing the atoms to move from their ordered state to a disordered fluid. By using this principle it is possible to determine the melting point by observing the average motion of the atoms in a system. For example, the Etters-Kaelberer parameter [123, 124] or the Berry parameter [125] are proportional to the fluctuations of the inter-atomic distances. These parameters suddenly increase at the melting point and may therefore be used as the definition of the melting temperature.

According to Born [126], melting occurs when one of the elastic shear moduli vanishes. Upon heating, the distances between the atoms increases due to thermal expansion, which reduces the restoring forces between the atoms and as a result the shear elastic moduli decrease with rising temperature. When the shear modulus vanishes the material experiences zero resistance and as a result the material can no longer sustain a shear stress which allows the atoms to move freely. In spite of the accordance of this model with the intuitive understanding of the difference between a solid and a liquid, this theory is not completely correct as the shear modulus does not vanish when the solid reaches the melting volume. However this criterion was later extended by Tallon et al. [127] who showed that by modification a melting criterion based on the shear moduli can nonetheless be formulated.

Cotterill [128] considered the role of anharmonicity in the process of melting and argued that the melting might be associated with bifurcation of the on-site potential. This idea closely follows Lindemann's idea, but provides a more thorough explanation of the melting phenomena. He suggested that with increasing volume at the melting point the crystal structure will be pushed towards a bifurcation instability, and that the liquid state might be the result of this bifurcation. This concept was further studied by Cotterill and Tallon [129], who demonstrated a bifurcation of the on-site potential at the solid-liquid phase transition. Melting as a result of the bifurcation of the on site potential will be further discussed in section 13.

Another method for identifying the likeliness of the system being in a solid or a liquid state can be formulated by inspection of the free energy. The curves of the free energy for the solid and liquid as a function of temperature will intersect and since a system will be in the state of the lowest free energy,

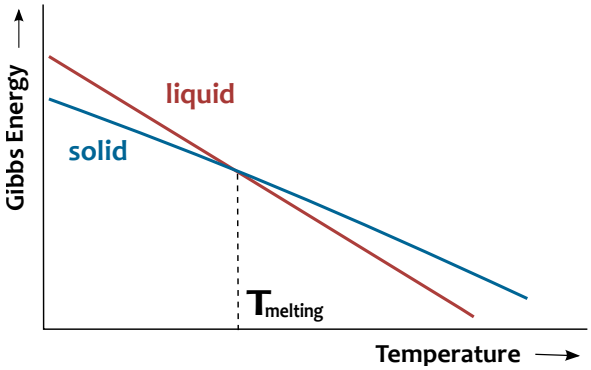

Figure 9.1.: Gibbs Free energy for the solid and liquid state

the temperature at intersection corresponds to the melting temperature. This is demonstrated in Fig. 9.1. At the melting temperature, the solid and the liquid are in thermodynamic equilibrium and the Gibbs free energies, $G = U + PV - TS$, are equal $G_s(P, T_m) = G_l(P, T_m)$. This theory not only includes the on-site potential in the description of the melting process but also considers the contribution of the entropy and perhaps provides the best explanation of the reason behind the melting transition.

The free energy of the system is a continuous function of pressure and temperature during the phase transitions, but other thermodynamic quantities such as internal energy U, entropy S, volume V and head capacity C undergo discontinuous changes. Upon melting, the inner energy suddenly increases and the heat capacity will show a peak at the phase transition. These quantities thus also allow to easily identify the melting point.

9.3. Simulation Methods

In the previous section it was shown how the melting temperature can be recognized by a range of different properties that define the difference between the solid and the liquid state or the transition between these two. It is therefore not surprising that there is also a wide range of possibilities in simulating the melting temperature. In this section a brief overview is given.

9.3.1. Direct Methods

The Hysteresis method

The most common method to study the melting temperature is by performing simulation of a perfect lattice by Molecular Dynamics (MD). Separate MD simulation are performed for a range of increasing temperatures. Starting

from a crystal structure, the atoms are given a kinetic energy, which on average corresponds to the simulation temperature. The temperature at which the lattice breaks down corresponds to the melting temperature. The problem which such a method is that due to superheating the system melts at a much higher temperatures called the hysteresis phenomenon. Similarly, when a liquid is cooled down, the phase change temperature is underestimated due to the existence of supercooling. As an approximation one can determine the melting point from the hysteresis method, for which the melting point is related to superheating and supercooling behavior as $T_m = T^+ + T^- - \sqrt{T^+ T^-}$ [130] [131] Supercooling and superheating are not just theoretical problems, but are observed experimentally as well and are currently a matter of intense research [132].

The Void Method

In order to eliminate superheating, defects can be introduced in the system as they are found to lower the observed melting point [133]. That is by either displacing atoms from their equilibrium solid state position or alternatively by removing atoms from the simulation cell. The impurities and vacancies introduced in the supercell create nucleation sites and eliminate the free energy barrier such that the solid melts at the true melting temperature rather then the superheated temperature. The void method is based on this principle: The melting point is determined by calculation on supercells with vacancies introduced in the solid structure [134]. The computed melting point decreases with the increasing concentration of voids until the melting point is independent of the number of voids, but this requires large numbers of particles N in the simulation.

The Interface Pinning

An alternative method to eliminate the superheating effect is by carrying out molecular dynamic simulations of a a system which contains both a solid and a liquid structure in the same simulated cell. The simulations are performed at various temperatures and the melting point is the temperature at which the phase boundary does not move. That is, when the temperature is too high, the solid-liquid interface moves such that the solid state melts starting from the interface and similarly when the temperature is too low the interface moves such that liquid state solidifies. [135] [136] [137] [138]

Monte Carlo

Whereas with MD the time evolution of a system at a given temperature is sampled, Monte Carlo (MC) aims to reproduce the statistical behavior at the thermodynamic equilibrium. Configurations are randomly generated for a

range of temperatures with the appropriate probability distribution and the average inner energy or heat capacity is obtained. This method allows to accurately determine the melting transition, but can computationally be cumbersome for systems of which the atomic or molecular interactions need to be determined by ab-initio methods, such as DFT, for each simulation step. The noble gases are special in the sense that their interaction potential converges fast and can thus be deducted from computational efficient functional forms which are fitted to the ab-initio data points as described in chapter 7. The MC melting method will therefore used to compute the melting temperatures of the noble gases and is discussed in detail in the next chapter.

9.3.2. Thermodynamic Integration

The thermodynamic integration method is based on the equality of the Gibbs free energy of the solid and liquid at the equilibrium melting point. By computing the Gibbs free energy of the solid and the liquid as a function of temperature, the melting point corresponds to the temperature at which the two curves intersect. Multiple schemes to solve the Gibbs free energy have been proposed, such as the single-occupancy cell method [139], Einstein Crystal Method (Free energy method for solids based on Monte Carlo) [140] or the Lambda integration method [141]
The first person to determine the melting temperature by applying the free energy method was Car in 1995 [142], who used the local density approximation to explicitly calculate the Gibbs energy of the solid and liquid by thermodynamic integration. Later, the melting properties of aluminum and iron were calculated from first-principles molecular-dynamics simulations using density-functional theory in the local-density approximation [143] [144] [145].
The high computational cost and the reliance on a good reference system for calculating the liquid free energy have so far hindered a general application. The difficulty lies in obtaining an absolute value for the entropy. Zhu [146], recently improved the method by by fitting two empirical potentials to the energies for the solid and the liquid phase which are obtained from density functional theory based on molecular dynamics runs. These potentials could then be used as reference systems for thermodynamic integration which leads to rapid convergence. The Gibbs free energy method has further been developed and used recently in random phase approximation simulations of silicon melting by Kresse and co-workers [147].

10. Monte Carlo Melting Simulations

In order to determine the melting temperature of the noble gases we aim to obtain the average energy as a function of the temperature. For systems in the NVT and NPT ensembles the expectation value of the energy is expressed as a multidimensional integral over the particle coordinates, which can only in very few cases be computed analytically. Therefore we will have to solve the integral by numerical methods instead. The Monte Carlo method has proven to be the most powerful numerical tool to compute such high-dimensional integrals efficiently. During a Monte Carlo simulation the expectation value of the energy, or other observables of interest, is approximated numerically by statistical sampling: many different configurations are generated of which statistical data can be obtained.
First we describe the general Monte Carlo algorithm in section 10.1. The melting temperatures will be obtained according to two different sampling schemes: Monte Carlo simulations at constant volume and Monte Carlo simulations at constant pressure. Numerical details on these two methods are given in section 10.3 and 10.2 respectively. Section 10.4 addresses the multi-histogram reweighting method. This method allows us to obtain the energy or heat capacity as a continuous function of the temperature without performing any additional simulations.

10.1. Monte Carlo

In order to obtain the melting temperature we are interested in the average value of an observable O at a given temperature

$$\langle O \rangle = \frac{\sum_i O e^{-\beta E_i}}{\sum_i e^{-\beta E_i}} \tag{10.1}$$

where the sum is over all the microscopic configurations of a system. Monte Carlo approximates this sum by averaging over a selected and much smaller number of more representative configurations of the system

$$\langle O \rangle = \frac{1}{M} \sum_{i=1}^{M} O_i \tag{10.2}$$

Such a selection can be made by generating configurations according to a Markov Chain. In the following sections this method is discussed.

10.1.1. The Metropolis Algorithm

Solving an Integral using Simple and Importance Sampling

The simplest form of the Monte Carlo technique is **simple sampling**, for which an integral

$$I = \int_a^b f(x)dx \tag{10.3}$$

is approximated by evaluating $f(x)$ at a large number of x_i values randomly distributed over the interval $[a, b]$, such that the expectation value of f is

$$\langle f \rangle = \frac{1}{\Omega} \int f(x)dx \approx \frac{1}{N} \sum_{i=1}^{N} f(x_i) \tag{10.4}$$

where $\Omega := \int dx$ is the integration volume. The error of this approximation is a statistical error which scales as $N^{-1/2}$.

$$\Delta f = \sqrt{\frac{\langle f^2 \rangle - \langle f \rangle^2}{N_{MC}}} \tag{10.5}$$

where N_{MC} is the number of Monte Carlo steps.
To improve the sampling convergence and the statistical error, the probability is approximated by **Importance Sampling**, where the sampling coordinates x_i are chosen not uniformly but according to a probability distribution $p(x)$,

$$\int p(x)dx = 1 \tag{10.6}$$

such that the integral can be sampled according to

$$I = \int f(x)dx = \int \frac{f(x)}{p(x)} p(x)dx \approx \frac{1}{N} \sum_{i=1}^{N} \frac{f(x_i)}{p(x_i)} \tag{10.7}$$

Because of this modification, the function will be evaluated in a concentrated region of space that make important contributions to the integral, and the error is

$$\Delta f = \sqrt{\frac{\langle g^2 \rangle - \langle g \rangle^2}{N_{MC}}} \tag{10.8}$$

where $g = f/p$. This implies that if the distribution function p is chosen very similar to f, the ratio f/p is nearly constant and the variance is small.

Generating Configurations According to a Markov Chain

In the previous section we saw how an integral can be numerically solved by importance sampling. We will now make the transition to the situation that directly applies to our simulation method: since we want to obtain the average energy of a system of noble gas atoms, many configurations are generated of which the average energy can be calculated. This means that the coordinates of the sum in Eq. (10.7) in fact are the coordinates of the noble gas atoms in the sampled system. During the Monte Carlo simulation we want to generate a sequence of random states so that by the end of the simulation each state has occurred with appropriate probability. This can be realized by sampling according to a **Markov chain**.

Starting from an initial configuration c_0 a Markov chain of configurations is generated

$$c_0 \to c_2 \to c_3 \to ... \to c_n \to c_{n+1} \to .. \tag{10.9}$$

In a Markov chain the probability for going from configuration c_x to configuration c_y depends only on c_x and not on previous configurations c_{-1}, c_{-2}. The transition probabilities of going from configuration c_x to c_y in one step of the Markov process is given by a transition matrix W_{xy} and since the sum of probabilities of going from configuration x to any other configuration is 1, the columns of the matrix W are normalized

$$\sum_y W_{xy} = 1 \tag{10.10}$$

At each step of the Markov process the probability distribution changes

$$\sum_x p_x^{(n)} W_{xy} = p_y^{(n+1)} \tag{10.11}$$

and converges to the desired equilibrium distribution p_x, such that p_x becomes the eigenvector of W with eigenvalue 1. For this to be the case the equilibrium condition must be fulfilled:

$$\sum_x p_x W_{xy} = p_y \tag{10.12}$$

Ergodicity and detailed balance are the two sufficient conditions to determine the transition matrix W such that we asymptotically reach the desired probability p_x.

Ergodicity: It has to be possible to reach any configuration x from any other configuration y in a finite number of Markov steps

Detailed balance: The probability of going from configuration x to configuration y, is the same as the probability of going from configuration y to configuration x

$$W_{xy} p_x = W_{yx} p_y \tag{10.13}$$

which satisfies both the equilibrium condition Eq. (10.12) and Eq. (10.10).

There are many different possibilities of formulating a set of rules such that on average the probability of finding the system in configuration x equals p_x. One of them is the **Metropolis algorithm** [148], which is a well-known technique in Monte Carlo simulations to efficiently sample the probability distribution p_x. The algorithm, starting from an initial configuration x, repeats the following steps:

- A test configuration x' is generated from x by moving a randomly selected atom i with randomly determined displacement δ according to $x_i \mapsto x_i + \delta$.
- Calculate the ratio of probabilites $\alpha(x \to x') \equiv \frac{p_{x'}}{p_x}$.
- If $\alpha(x \to x') > 1$ the next point is $x_{i+1} = x'$.
- If $\alpha(x \to x') < 1$ the next point is $x_{i+1} = x'$ with probability u, otherwise $x_{i+1} = x$. Here u is a random number, generated in the range $[0, 1]$.
- Calculate the quantity of interest O at the new point x_{i+1}.

The Metropolis algorithm satisfies detailed balance and is also ergodic if one ensures that the possible random changes allow all points in the integration domain to be reached in a finite number of steps. The acceptance probability can be written in a short notation as

$$\alpha(x, x') = \min\left(1, \frac{p(x)}{p(x')}\right) \tag{10.14}$$

Through the importance sampling algorithm it is possible to estimate the expectation value for an observable from the ratio of probabilities between two configurations. This is an important aspect of the sampling process: the partition function does not need to be solved.

10.1.2. Monte Carlo Cycles

In order to limit the influence of correlations, the statistical data of interest is not sampled after every MC step, but is only calculated after a cycle of steps. This cycle $\mathbf{R}_\xi \mapsto \mathbf{R}_{\xi+1}$ is realized by a sequence of $m \gg 1$ steps , such that:

$$\mathbf{R}_\xi \equiv \mathbf{R}_{\xi_0} \mapsto \mathbf{R}_{\xi_1} \ldots \mapsto \mathbf{R}_{\xi_\iota} \ldots \mapsto \mathbf{R}_{\xi_m} \equiv \mathbf{R}_{\xi+1} \tag{10.15}$$

The notation $\mathbf{R}_{\xi_\iota} \mapsto \mathbf{R}_{\xi_{\iota'}}$ means that from $\mathbf{R}_{\xi_\iota}$ a new configuration $\mathbf{R}_{\xi_{\iota'}}$ is created, wich will be accepted according to the acceptance criterion as given in equation Eq. (10.14). The step $\mathbf{R}_{\xi_\iota} \mapsto \mathbf{R}_{\xi_{\iota+1}}$, or a sequence of such steps, is referred to as propagation.

10.1.3. Updating the MC Step Size

During the MC simulation an atom is moved with step size δ_x, which is randomly selected in the range $\delta_x = \{-\Delta, \Delta\}$, where Δ is the maximum step size. Updating Δ allows the phase space to be sampled more efficiently and can improve the overall accuracy and convergence of the simulations. However, updating the maximum step size needs to be done carefully, since it can introduce an undesirable bias into the results of the simulation.

During our Monte Carlo simulation the step size is adjusted according to the acceptance-ratio method. The acceptance-ratio method (ARM) [149] is an optimization technique that adjusts the acceptance ratio to a predetermined optimal value P_{ideal}. The updating equation reads

$$\Delta_{new} = \Delta_{old} \frac{\ln(aP_{ideal} + b)}{\ln(aP_{old} + b)} \tag{10.16}$$

The constants a and b are chosen so that $\Delta_{new} = r\Delta_{old}$ when $P_{old} = 1$ and $\Delta_{new} = \Delta_{old}/r$ when $P_{old} = 0$. [150] Since the ARM method uses information from past configurations in determining the transition probabilities, it is not strictly Markovian, which raises the possibility that systematic errors are generated. It is shown by Swendsen [150] that the systematic error is smaller than the inevitable random errors in a Monte Carlo simulation and therefore negligible for practical applications.

During our simulation the maximal step size δ is compared after N atomic movements and updated if $P_{old} - P_{ideal} > 0.01$, such that the average acceptance is $P_{acc} = P_{ideal} = 0.5$. Lower optimal acceptance probabilities have been derived [149]). Nevertheless, we use the value of $P_{average} = 0.5$ because a lower rate means that too many moves are rejected and the wasting computational effort is increased. A higher average acceptance rate means that the generated trial configurations are too close to the starting ones, thus having a small difference in energy compared to the temperature. This implies that the accepted configurations evolve too slowly, again leading to increased computational effort. In Eq. (10.16) r is an adjustable variable and in our simulation chosen to be 2.0; for which $a = 0.47213595$ and $b = 0.14589803$.

10.1.4. Parallel Tempering

Systems simulated at low temperatures can have difficulties overcoming local minima since the full exploration of phase space is hindered, which could lead to non-ergodicities. Parallel Tempering Monte Carlo (PTMC) [151], also called Replica Exchange Monte Carlo, is a techniques that improves the sampling of configurations. The aim of PTMC is to enable systems that are simulated at low temperatures to overcome energetic barriers that hinder their sampling. During the PTMC simulation, multiple copies of the same system are simultaneously propagated at different temperatures and an exchange of

configurations of two temperatures is attempted at the end of a MC cycle. As a result, the low-temperature simulation can inherit new configurations for sampling from different parts in phase space without having to overcome the energy barriers itself. This allows the phase space to be explored more efficiently.

To be specific, after each Monte Carlo cycle an attempt to exchange configurations is made with a probability of 10 percent and the configurations are attempted to be exchanged at a randomly selected temperature t and t' . The exchange is accepted with a probability of

$$\text{acc}(x \rightarrow x') = \min(1, e^{(\beta_{t'} - \beta_t)(E(\mathbf{R}_{xt}) - E(\mathbf{R}_{xt'}) + P(V_{xt} - V_{nt'})}) \tag{10.17}$$

In order for the exchanges to be efficient, t is chosen randomly in $t \in \{1, N_R - 1\}$ and t‘ is a neighboring temperature, $t = t + 1$, such that probability of acceptance exponentially falls of with $\beta - \beta'$. In practice an exchange probability of around $\text{acc}(x \rightarrow x') = 0.8$ for temperatures far below or far above the temperature of the phase transition is found, whereas for the temperatures close to the phase transition an acceptance of $\text{acc}(x \rightarrow x') = 0.4$ is observed.

10.2. Constant Pressure Simulations for Periodic Cells

Melting of the bulk is simulated using face-centered cubic (FCC) sample cells of $N = 4k^3 = [32, 108, 256, 500, 864, ..]$ atoms with periodic boundary conditions. The simulations are performed in the isobaric-isothermal ensemble, which means that the particle number and simulation temperature are held constant while the simulation box is allowed to change volume to remain at constant pressure throughout the simulation.

In the following section details on the Monte Carlo algorithm are given that need to be implemented in order to calculate the melting temperature for periodic cells at constant pressure.

10.2.1. Acceptance Criterion for the Isobaric Isothermal Ensemble

During the NPT simulation the test configuration is generated by either randomly selecting particle i and changing its coordinates from $\mathbf{r}_i \mapsto \mathbf{r}_i + \mathbf{\Delta}$, or by varying the volume V with a randomly determined scaling parameter ς. The latter corresponds to the scaling of the volume V with ς^3, such that the new configuration is scaled as $\mathbf{R} \mapsto \varsigma\mathbf{R}$ and the simulation cell by $L \mapsto \varsigma L$. The decision between moving an atom or varying the volume has also to be made randomly. In typical implementations, a randomly determined particle i is displaced with a probability $P = N/(N+1)$ and scaling of the volume V takes place with a probability of $P = 1/(N+1)$.

When a volume change is attempted, the old volume is scaled according to

$$V_{new} = V_{old} + \Delta V \tag{10.18}$$

where ΔV is a random number uniformly distributed over the interval $[-\Delta V_{max}, +\Delta V_{max}]$. In the canonical ensemble the probability density to find a particular configuration of N atoms at a given volume V is proportional to

$$\begin{aligned} N(V;\mathbf{R}) &\propto V^N \exp(-\beta PV) \exp[-\beta E(\mathbf{R})] \\ &\propto \exp\big(-\beta[E(\mathbf{R}) + PV - N\beta^{-1} \ln V]\big) \end{aligned} \tag{10.19}$$

and therefore the ratio of probability is

$$\frac{p_{x'}}{p_x} = e^{-\beta(E_{x'} - E_x) - \beta(V_{x'} - V_x) - N k_B \ln(V'/V)} \tag{10.20}$$

such that the acceptance criterion for either moving an atom or scaling the volume becomes

$$\alpha(x \to x') = \min(1, e^{-\beta[\Delta E + P\Delta V] + N \ln(V/V')}) \tag{10.21}$$

Trial moves in the volume can also be made according to

$$V_{new} = V_{old}\, e^{\Delta V} \tag{10.22}$$

In this case the partition function takes a slightly different form and the acceptance criterion becomes

$$\alpha(x \to x') = \min(1, e^{-\beta[\Delta E + P\Delta V] + (N+1)\ln(V/V')}) \tag{10.23}$$

10.2.2. Determining the Melting Temperature

For the simulated cells the melting temperature will be extracted from the heat capacity curve $C_p(T) = \frac{\partial \langle H \rangle}{\partial T}$, which shows a maximum at the solid-liquid phase change. The enthalpy is given by

$$H = U + PV \tag{10.24}$$

(remember that the internal energy is defined as the statistical mean value of internal energies E_i: $U = \langle E_i \rangle = \sum_i p_i E_i$).
Using the identities

$$\langle H \rangle = \frac{\sum H e^{-\beta H_n}}{\sum e^{-\beta H_n}} = \frac{1}{Z}\frac{\partial Z}{\partial \beta} \tag{10.25}$$

$$\left\langle H^2 \right\rangle = \frac{\sum H^2 e^{-\beta H_n}}{\sum e^{-\beta H_n}} = \frac{1}{Z}\frac{\partial^2 Z}{\partial \beta^2} \tag{10.26}$$

the heat capacity can be expressed as

$$\begin{aligned} C_p(T) &= \frac{\partial \langle H \rangle}{\partial T} \\ &= \frac{-1}{k_B T^2}\left[\frac{1}{Z}\frac{\partial^2 Z}{\partial \beta^2} - \frac{1}{Z^2}\left(\frac{\partial Z}{\partial \beta}\right)^2\right] \\ &= \frac{\langle H^2 \rangle - \langle H \rangle^2}{k_B T^2} \end{aligned} \tag{10.27}$$

10.2.3. Minimum Image Convention

For consistency with the minimum image convention, which states that a particle must interact only with the closest image of any other particle, a spherical cut-off for the two body potential of $\frac{1}{2}L$ is applied, with L being the length of the simulation cell. For pair potentials, double counting can easily be avoided, but there is no unique way of applying the minimum image convention when calculating the three-body energy. When we consider a triangle of particles labeled i, j and k the minimum image convention can only be applied to two sides of the triangle say, to particle j with i and to

particle k with i. The distance between particle j and k is then fixed. The problem is that the distance between the closest image of particles j and k with respect to particle i is not necessarily the minimum-image distance of j to k. This problem can be overcome by defining the translation vectors [119],

$$t_{ij} = [(x_i - x_j)/L]L, \quad t_{ik}[(x_i - x_k)/L]L \tag{10.28}$$

with $[x]$ being the closest integer to x. The resulting x components (the same principle holds for the y and z coordinates) of the separation vector between the particles are given by

$$\begin{aligned} x_{ij} &= x_i - x_j - t_{ij} \\ x_{ik} &= x_i - x_k - t_{ik} \\ x_{jk} &= x_j - x_k + t_{ij} - t_{ik} \end{aligned} \tag{10.29}$$

10.2.4. Long-range corrections

The two-body contribution to the total interaction energy $E^{(2)}$ is determined by summing over all pairwise interactions up to a spherical cutoff distance r_c. The resulting two body energy of the simulations can be corrected to compensate for the missing long range contribution $E^{(2)}_{LRC}$.
Assuming pairwise additivity, the total two body energy in a system of density ρ and radial distribution function $g(r)$ is

$$E^{(2)} = \frac{1}{2}\rho \int_0^\infty E(r)g(r)4\pi r^2 dr \tag{10.30}$$

The integral can be split into a sum over the region $\{0, r_c\}$ and an integral over the long range $\{r_c, \infty\}$:

$$E^{(2)} = E^{(2)}_{MC} + E^{(2)}_{LRC} = \sum_{i=1}^{N} V(r_{rij}) + 2\pi N\rho \int_{r_c}^\infty r^2 E(r)g(r)dr \tag{10.31}$$

Where $E^{(2)}_{MC}$ is obtained during the MC simulation with $V(r)$ is the two body potential, and the second part of the energy contribution is the long-range correction. The radial distribution function $g(r)$ is assumed to be of the form

$$g(r) = \exp\Big[-\beta E^{(2)}(r)\Big] \tag{10.32}$$

The integral over the long range will be numerically evaluated using Gauss-Legendre quadrature, which is an algorithm that approximates an integral by the sum of weighted integrand values sampled at special points called abscissas

$$\int_{-1}^{1} f(x)dx \approx \sum_{i=1}^{n} w_i f(\xi_i) \tag{10.33}$$

where ξ_i are the n zeroes of the n^{th}-degree Legendre polynomials $P_n(\xi)$ and the weights are calculated as

$$w_i = \frac{2}{(1-\xi_i^2)[P_n'(\xi_i)]^2} \tag{10.34}$$

In order to use the Gauss-Legendre quadrature the integral is rewritten such that the boundaries are from -1 to 1 instead of a to b. After this transformation the integral can easily be evaluated

$$\begin{aligned}\int_a^b f(x)dx &= \frac{b-a}{2}\int_{-1}^{1} f\left(\frac{b-a}{2}x + \frac{a+b}{2}\right)dx \\ &\approx \frac{b-a}{2}\sum_{i=1}^{n} w_i f\left(\frac{b-a}{2}\xi_i + \frac{a+b}{2}\right)\end{aligned} \tag{10.35}$$

In our simulation the interval $[r_c, \infty)$ is divided into 100 intervals of length d and each sub-interval is integrated individually. This means that the integral is not calculated up to infinity, but instead is approximated with the boundaries being $[r_c, 100d]$. A 20-th order Gauss-Legendre scheme is used for numerical evaluation of each sub-integral. It is sufficient to calculate the tail correction only once at the beginning of the simulation, since the cut-off radius, r_c, is held constant. One might wonder why the tail correction would be included as for each MC step the same long range energy is considered. However the probability of accepting a volume displacements is influenced by the long-range correction because the density ρ varies during the simulation, see Eq. (10.31).

10.2.5. Correction for Superheating

The absence of a surface in the periodic melting simulations causes the simulated cells to melt at a superheated temperature. We adapt the superheating correction factor as derived by Belonoshko [152]

$$\frac{T_{SH}}{T_m} = 1 + \frac{\ln 2}{3} \approx 1.23105 \tag{10.36}$$

where T_{SH} is the superheated temperature of the solid to liquid phase transition and T_m is the true melting temperature of the bulk. The motivation behind the choice of this correction factor can be found in section 14.

10.3. Constant Volume Simulations for Clusters

Simulating periodic cells is problematic as the absence of a surface will cause the cells to melt at a superheated temperature. Therefore we will simulate the melting of the noble gases by an alternative method, that is by studying the melting of finite clusters in the canonical (NVT) ensemble, which means that the particle number N, hard-sphere volume V and temperature T are held constant during the Monte Carlo simulation. Since the cluster melting is initiated at the surface of the cluster, superheating does not occur.

In the past molecular dynamics simulations have been carried out on icosahedral argon clusters [153], however the method showed to be problematic as the outer atoms evaporated before melting of the core occurred. More recently Monte Carlo cluster simulations of neon and argon were performed by Pahl et al. [154], who defined a hard sphere around the icosahedral clusters such that the atoms are confined and therefore evaporation is avoided. In this thesis the heavier noble gases are simulated according to the same procedure.

Mackay icosahedral clusters are chosen as initial structures for the solid state, which are characterized by k complete shells of atoms around a central atom, see figures 10.1 and 10.2. The sizes of these so-called magic clusters with high stability are given by

$$N = 1 + 2\sum_{k=1}(5k^2 + 1) \tag{10.37}$$

$$= \frac{10}{2}k^3 + 5k^2 + \frac{11}{3}k + 1 \tag{10.38}$$

which corresponds to structures of N = [13, 55, 147, 309, 561, 923, 1415, ...] atoms. Of course, one is not confined to simulations of magic-number clusters only and the same simulating procedure can be applied to other particle sizes and configurations [155]. However, due to their closed shell structure, surface effects are minimized with respect to the clusters with incomplete shells, which allows us to linear extrapolate to the bulk melting temperature T_m. The justification of such an extrapolation scheme is explained in section 10.5.2.

10.3.1. Acceptance Criterion for the Canonical Ensemble

For the NVT ensemble the probability of being in a macrostate i is given by Eq. (9.5) and is proportional to

$$p_i \propto e^{-\beta E_i} \tag{10.39}$$

Therefore the ratio of probability between original configuration x and trial configuration x' is

$$\frac{p_{x'}}{p_x} = e^{-\beta(E_{x'} - E_x)} \tag{10.40}$$

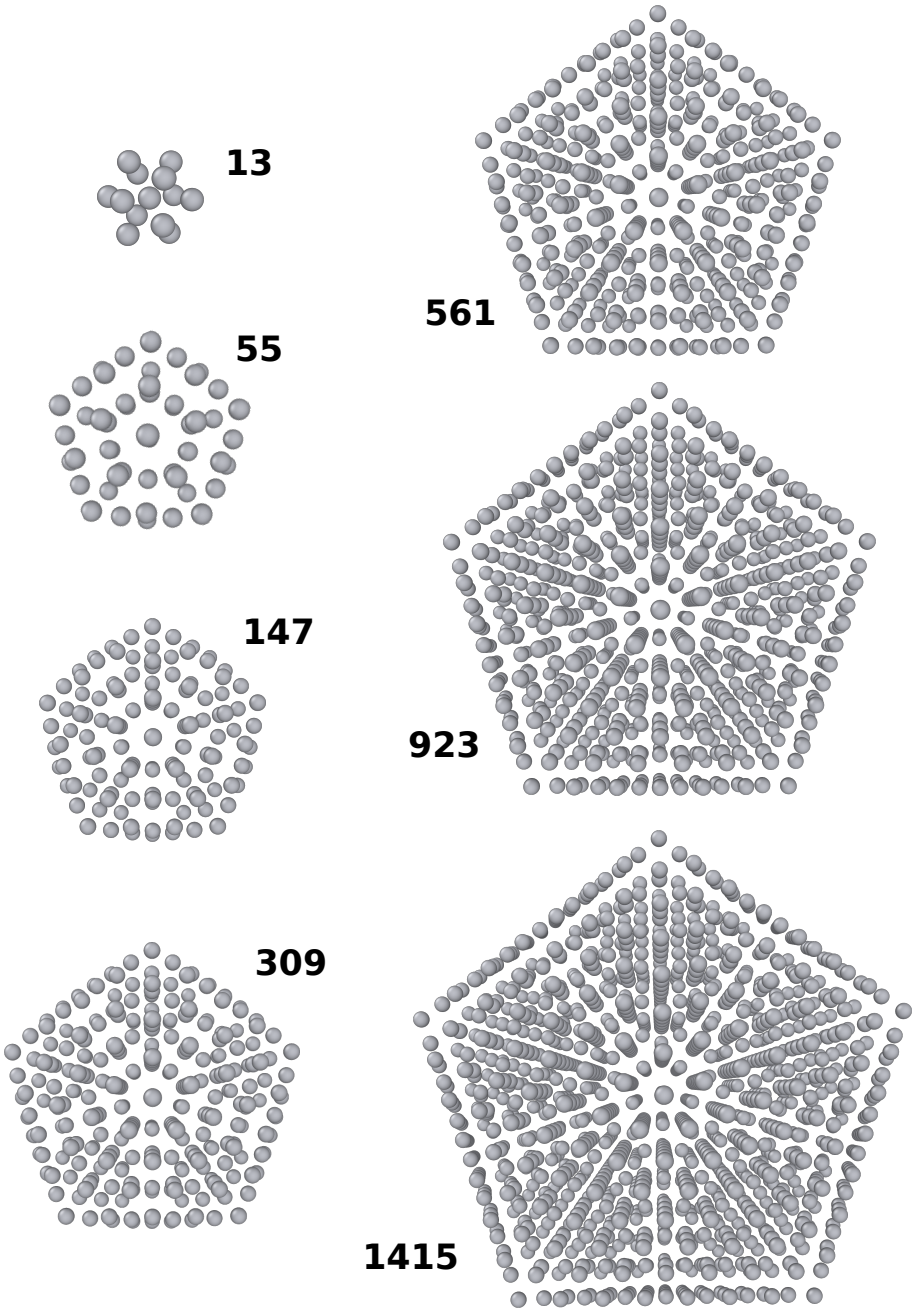

Figure 10.1.: Mackay icosahedral clusters with N = 13, 55, 147, 309, 561, 923 and 1415 atoms.

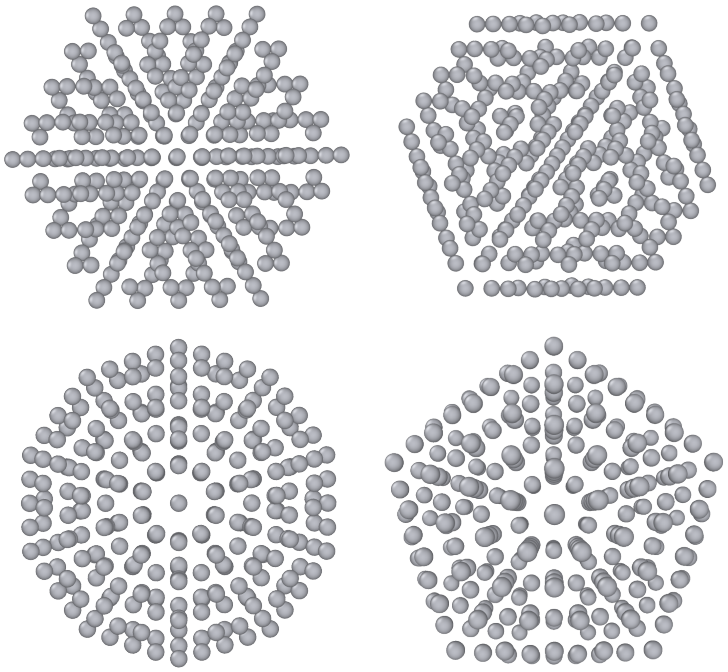

Figure 10.2.: Different orientations of the Mackay icosahedral cluster containing 309 atoms.

such that a Monte Carlo move is accepted with the probability of

$$\alpha(x \to x') = \min\left(1, e^{-\beta(E_{x'} - E_x)}\right) \tag{10.41}$$

10.3.2. Determining the Melting Temperature

For each cluster the melting temperature will be extracted from the heat capacity curve, $C_v(T)$, which shows a maximum at the solid-liquid phase change. Using the identity

$$\langle E \rangle = \frac{\sum E e^{-\beta E_n}}{\sum e^{-\beta E_n}} = \frac{1}{Z}\frac{\partial Z}{\partial \beta} \tag{10.42}$$

$$\left\langle E^2 \right\rangle = \frac{\sum E^2 e^{-\beta E_n}}{\sum e^{-\beta E_n}} = \frac{1}{Z}\frac{\partial^2 Z}{\partial \beta^2} \tag{10.43}$$

the heat capacity can be expressed in as

$$\begin{aligned} C_v(T) &= \frac{\partial \langle E \rangle}{\partial T} \\ &= \frac{-1}{k_B T^2}\left[\frac{1}{Z}\frac{\partial^2 Z}{\partial \beta^2} - \frac{1}{Z^2}\left(\frac{\partial Z}{\partial \beta}\right)^2\right] \\ &= \frac{\langle E^2 \rangle - \langle E \rangle^2}{k_B T^2} \end{aligned} \tag{10.44}$$

This means that the quantity of interest for the cluster simulations is the average energy as a function of temperature.

10.4. Multi-Histogram Reweighting Technique

During a Monte Carlo simulation at a given temperature not only the average energy, but the entire energy distribution is saved. This additional data carries many useful information. In fact, enough information is collected to interpolate between the different discrete temperatures by performing a reweighted multi-histogram analysis, such that the sample means are obtained smoothly over the temperature range [156] [157].

We will start with an explanation of the reweighting method in section 10.4.1. Reweightig enables to acquire the distribution of the energy probability $P(E,T)$ at temperature T from the distribution $P(E,T_0)$ at a neighboring temperature T_0, without performing any additional simulations. In section 10.4.2 the weighted multiple-histogram method is discussed. This method makes it possible to obtain a continuous function of the energy versus temperature by combined use of several histograms at neighboring temperatures.

10.4.1. Single histogram reweighting

We will start by deriving how, from a distribution of the energy probability $P(E,T_0)$ at temperature T_0, one can obtain the the distribution $P(E,T)$ at a neighboring temperature T without performing any additional simulations. The expectation of an observable O of the canonical ensemble at some inverse temperature $\beta = \frac{1}{k_B T}$ is given by

$$\langle O \rangle_\beta = \frac{1}{Z} \sum_{\{\alpha\}} O(\alpha) \exp(-\beta E_\alpha) \approx \frac{1}{N} \sum_{i=1}^{N} O_i \tag{10.45}$$

where the first sum goes over the full configuration space and the second over the Monte Carlo configurations. The corresponding canonical partition function is

$$Z = \sum_{\{\alpha\}} \exp(-\beta E_\alpha)) \tag{10.46}$$

This function, expressed as a summation over possible states α, can also be expressed as a summation over the density of states $n(E)$

$$Z = \sum_{\{\alpha\}} \exp(-\beta E_\alpha) = \sum_{E} n(E) \exp(-\beta E) \tag{10.47}$$

Similarly, the expectation value of the observable O at inverse temperature β can be expressed in terms of the density of states

$$\langle O \rangle_\beta = \frac{\sum_E O(E) n(E) \exp(-\beta E)}{\sum_E n(E) \exp(-\beta E)} \tag{10.48}$$

At a near lying inverse temperature β', the partition function at β' can be expressed as

$$\begin{aligned} Z' &= \sum_E n(E) \exp\bigl(-\beta' E\bigr) \\ &= \sum_E n(E) \exp(-\beta E) \exp\bigl(\beta E - \beta' E\bigr) \end{aligned} \tag{10.49}$$

and the expectation value of the same observable O at inverse temperature β' is

$$\begin{aligned} \langle O \rangle_{\beta'} &= \frac{\sum_E O(E) n(E) \exp(-\beta' E)}{\sum_E n(E) \exp(-\beta' E)} \\ &= \frac{\sum_E O(E) n(E) \exp(\Delta\beta E) \exp(-\beta E)}{\sum_E n(E) \exp(\Delta\beta E) \exp(-\beta E)} \end{aligned} \tag{10.50}$$

where

$$\Delta\beta = \beta - \beta' \tag{10.51}$$

During the Monte Carlo sampling the count of occurance is recorded. To construct such a histogram, an energy range $[E_{min}, E_{max}]$ is divided into a series of discrete intervals ΔE, called bins, such that each bin contains the number of occurrences of the range of energy that are contained within that bin. How many energies fall into each interval is referred to as the count of occurrence. The normalized distribution $H(E)$ of the counts of occurrence $h(E)$ is

$$H(E) = \frac{h(E)}{N} \tag{10.52}$$

where N is the total number of binned energies. In contrast to the density of states $n(E)$, the count of occurance $h(E)$ is temperature dependent. However, the normalized distribution $H(E)$ can be expressed in terms of the density of states

$$H(E) = C(T) n(E) \exp(-\beta E) \tag{10.53}$$

where $C(T)$ is an undetermined temperature dependent constant. Substituting Eq. (10.52) and Eq. (10.53) into the final equality of Eq. (10.50) leaves us with the average value of the observable O at temperature β' expressed in terms of the histogram $h(E)$ obtained at inverse temperature β and the inverse temperature difference $\Delta\beta$

$$\langle O \rangle_{\beta'} = \frac{\sum_E O(E) h(E) \exp(\Delta\beta E)}{\sum_E h(E) \exp(\Delta\beta E)} \quad . \tag{10.54}$$

This method is called the single histogram reweighting technique. Figure 10.3 shows the probability distributions obtained from the original $P(E, T_0)$ for $T = T_0 + \Delta\beta$. One immediately sees that at large temperature reweighting distances the histograms worsens, this is due to the limited statistics in the tails of the original distribution.

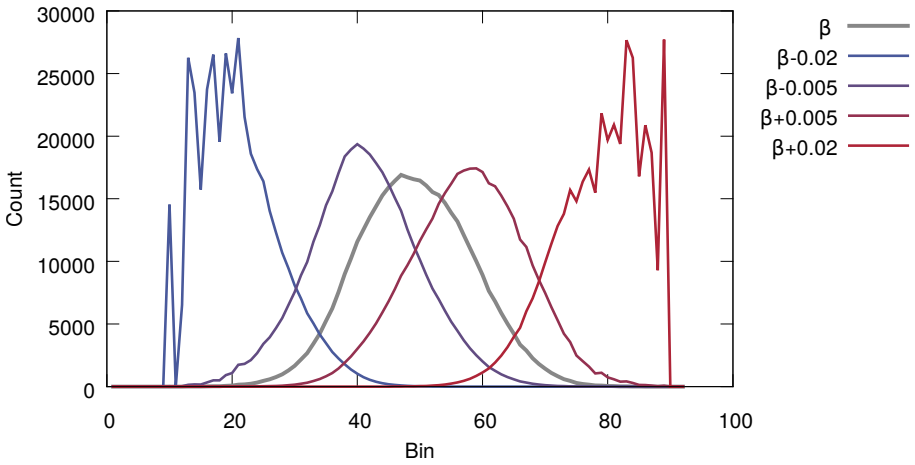

Figure 10.3.: A single histogram reweighted for different near lying temperatures. Errors are magnified when the histogram is reweighted for larger change in temperature.

10.4.2. Multiple Histogram Reweighting Technique

Since statistical errors get magnified in the wings of the distribution during the reweighting procedure, the single histogram techniques is not very reliable for large temperature shifts. This problem is eased by combined use of several histograms at suitable chosen neighboring temperatures, which can be done according to the Weighted Histogram Analysis Method (WHAM) [158] [159]. The idea is that at a given interpolated temperature, the contribution of the different histograms to the densities of states is weighted such that the error in the density of states is minimized. This interpolation scheme allows us to obtain a continuous function of the observed quantity O as a function of temperature, without performing any additional Monte Carlo simulations.
Similarly as for the Single Histogram Reweighting technique, but now for all simulated inverse temperatures β_i, the distribution $H_i(E)$ is expressed as

$$H_i(E) = \frac{n[E]\exp(-\beta_i E)}{\sum_E n(E)\exp(-\beta_i E)} \tag{10.55}$$

and the distribution of simulated inverse temperature β_i is related to the histogram $h_i(E)$

$$H_i(E) = \frac{h_i(E)}{N_i} \tag{10.56}$$

where N_i is the total number of configurations with an energy $E \pm \Delta E$.

The reduced free energy f_i is defined by

$$f_i \equiv \frac{F}{k_B T} = -\ln \sum_E n(E)\exp(-\beta_i E) \tag{10.57}$$

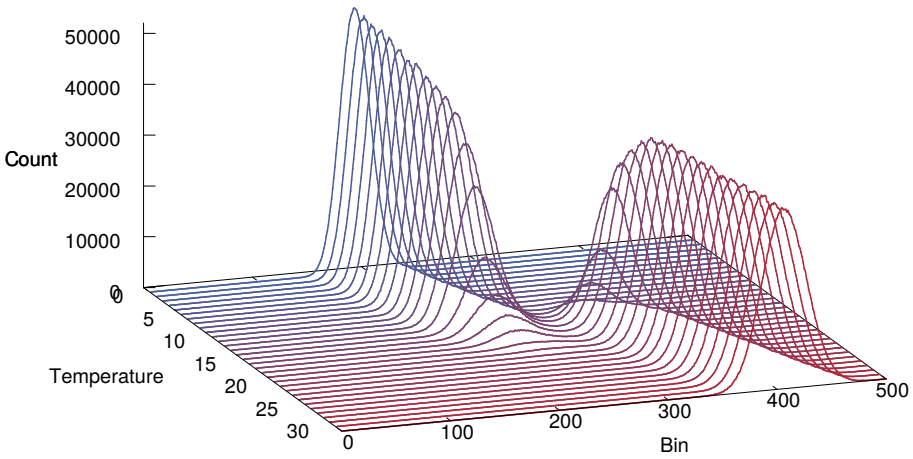

Figure 10.4.: Counted number of energy configurations for each of the 32 simulated temperatures. The simulation data was obtained for a cluster with $N = 147$ Oganesson atoms simulated with the scalar relativistic two body potential.

with F free energy. Therefore, Eq. (10.55) can be rewritten as

$$H_i(E) = \frac{n(E)}{\exp(\beta_i E - f_i)} \tag{10.58}$$

and by combining, Eq (10.58) and (10.56), the density of states can be written as

$$n(E) = \frac{h_i(E)}{N_i} \exp(\beta_i E - f_i) \tag{10.59}$$

Ideally, this would lead to the same density of states for all the different histograms obtained for the simulated inverse temperatures β_i. In practice however, this is most likely not the case. A solution to this problem is to combine the density of states $n(E)$ from the R different simulations temperatures β_i and weight them by a probability $p_i(E)$ such that the density minimizes the statistical error in $n(E)$:

$$n(E) = \sum_i^R \frac{p_i(E) h_i(E)}{N_i} \exp(\beta_i E - f_i) \tag{10.60}$$

The weighting coefficients $p_i(E)$ that minimize the error are determined to be [160]

$$p_i(E) = \frac{N_i \exp(-(\beta_i E - f_i))}{\sum_j^R N_j \exp(-(\beta_j E - f_j))} \tag{10.61}$$

Combining Eq. (10.60) and (10.61) gives a new expression for the density of

states,

$$n(E) = \frac{\sum_i^R h_i(E)}{\sum_j^R N_j \exp(-(\beta_j E - f_j))} \tag{10.62}$$

and substituting this into Eq. (10.57) allows us to write the free energy as

$$\exp(-f_k) = \sum_E \frac{\sum_i^R h_i(E)}{\sum_j^R N_j \exp(-(\beta_j E - f_j))} \exp(-\beta_k E) \tag{10.63}$$

The calculation of the free energy f_k at inverse temperature β_k is found self-consistently by iterating Eq. (10.63). When the change in free energy over an iteration is small - of the order of 10^{-5} the relative weights have converged. It is important to realize that this method will only lead to a converged free energy if there is sufficient overlap between near-lying histograms: if there is a small or no overlap, the difference between the free energy will be diverging. Once the free energy is converged, one uses the weighted value of the density of states $n(E)$ from Eq. (10.62) to calculate the observable $\langle O \rangle$ for any β in the simulated temperature range

$$\langle O \rangle_\beta = \frac{\sum_E O(E) n(E) \exp(-\beta E)}{\sum_E n(E) \exp(-\beta E)} \tag{10.64}$$

Fig. 10.5 illustrates the smooth curve obtained from the multi-histogram analysis. The heat capacity is calculated according to $C_v = \partial E / \partial T \propto \langle E(T)^2 \rangle - \langle E(T) \rangle^2$.

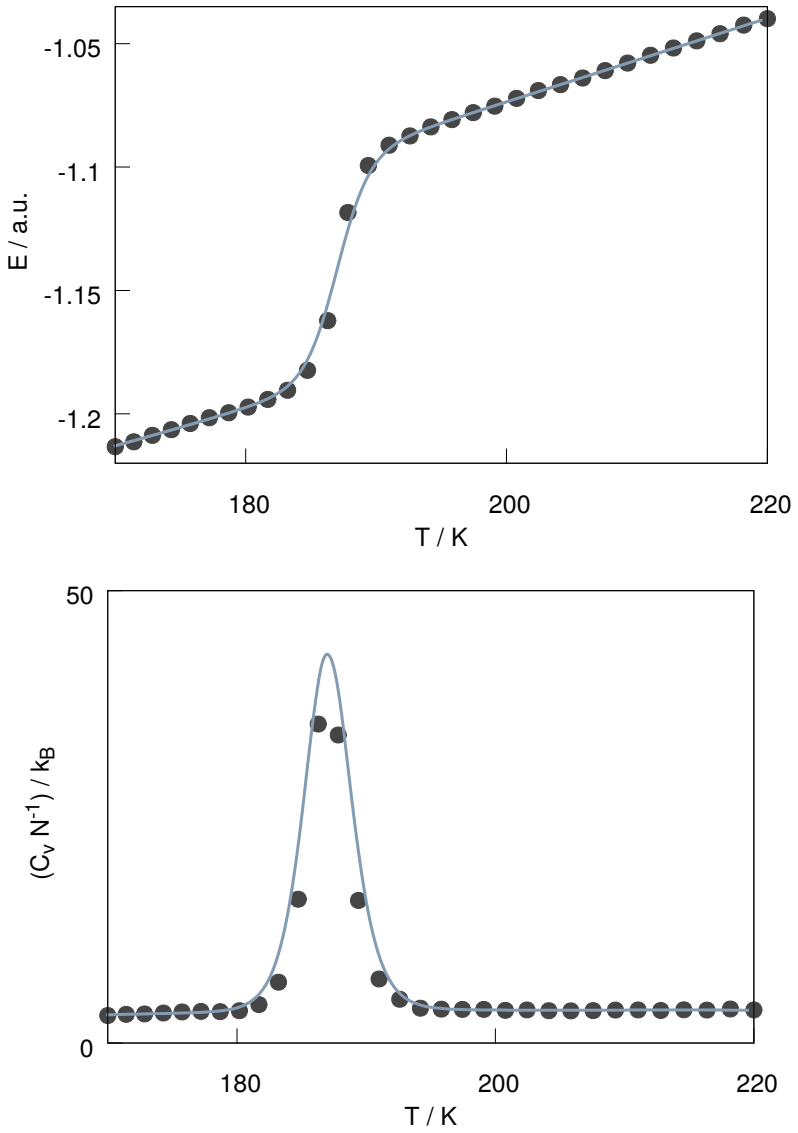

Figure 10.5.: Reweighted energy (top) and heat capacity curves (bottom) for a cluster with $N = 147$ oganesson atoms simulated with the scalar relativistic two body potential. Dots denote the discrete energies and heat capacities obtained from the 32 sampled temperatures, and the continued curve is calculated with the multi histogram analysis.

10.5. Size Effects

10.5.1. Broadening of the Heat Capacity Peak

The characteristic of a first-order phase transition is a sudden jump in the internal energy which translates to a very narrow peak in the heat capacity curve. However, often the first-order phase transition acquires a finite width over a range of temperatures and as a result the heat capacity peak is broadened. Broadening of the heat capacity is observed both in experiment as well as in numerical simulations and implies that the melting is not well defined for the system. In large systems broadening can also be observed due to phase co-existence, where during cooling or heating two phases co-exist, and as a result the melting temperature is again less well defined. In this case the broadening is most likely due to poor convergence with respect to the number of steps in the MC simulation rather than being an intrinsic character of system as in the macroscopic limit $N_{steps} \to \infty$ there is an exact transition temperature for an ideal system.
In small systems broadening of the heat capacity curve does not necessarily occur due to the co-existence of two phases but rather is a result of the finite size, i.e. the system being prone to strong fluctuation in their statistical properties. For example, the melting temperature is largely influenced by the shape of the finite-size system and due to these fluctuations the melting point is ill defined. Hence there is the possibility that, during a Monte Carlo cycle at a fixed temperature, the configurations propagate from the solid to the liquid and visa versa. This effect is known as dynamic coexistence [161]. Since the estimated inner energy is an average between the sampled configurations, the resulting energy curve as a function of temperature does not show a sudden jump but can become a slope over a finite temperature range. [162]
Imry [163] estimated the broadening ΔT_m for the melting transition as a function of system size N and the entropy difference ΔS between the solid and liquid state as

$$\frac{\Delta T_m}{T_m} \approx \frac{k_B}{N \Delta S} \tag{10.65}$$

Combining this result with the fact that the latent heat of melting is given by $L_m = \Delta S \, T_m$ the broadening of the heat capacity becomes

$$\Delta T_m(N) \approx \frac{k_B T_m}{N \Delta S} = \frac{k_B T_m^2}{N L_m} \tag{10.66}$$

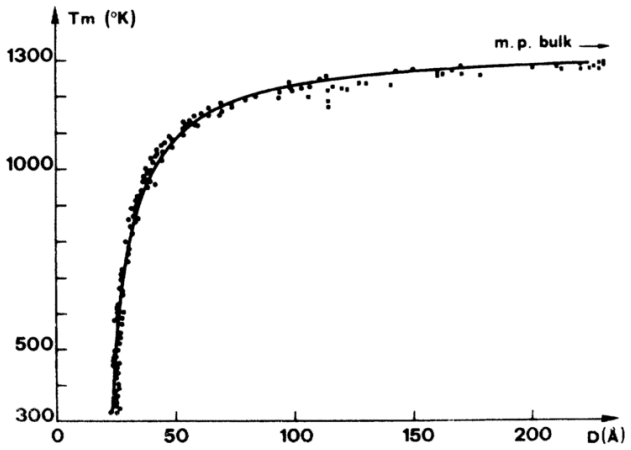

Figure 10.6.: Experimental (dots) and theoretical (solid line) melting-point temperatures of gold nano particles with respect to the cluster size. Reprinted with permission from [164] Copyright 1976 by the American Physical Society.

10.5.2. Size Dependent Melting Point Depression

A cluster's melting temperature decreases with an inverse dependence on cluster radius, as demonstrated for an experimental study on gold clusters [164] in Fig. (10.7). This melting trend can be attributed to the surface atoms being less strongly bound than bulk atoms, resulting in a lower melting temperature for smaller clusters. It is possible to derive a relation between the melting temperature of a cluster of N atoms with a spherical shape, $T_m(N)$, and the bulk melting temperature, $T_m(\infty)$. This relation enables us to extrapolate the obtained melting temperatures for the finite clusters to the melting temperature of the bulk. In order to do so, not only the binding energy of the individual atoms need to be considered, but also the inter-facial energies, solid/vapour and liquid/vapour, need to be included as well.

Pawlow's model A simple relation has been derived by Pawlow, [165], who considered the equilibrium condition between a solid and a liquid particle, leading to a relation that describes the melting temperature as a function of the particle size. As the chemical potentials of a solid, μ_s, and a liquid, μ_l, are equal at the melting temperature.

$$\mu_s(p,T) = \mu_l(p,T) \tag{10.67}$$

one can solve this equation starting from a first-order Taylor expansion of the chemical potential around its value at the triple point

$$\mu(p,T) = \mu(p_0,T_0) + \frac{\partial \mu}{\partial T}(T-T_0) + \frac{\partial \mu}{\partial p}(p-p_0) \tag{10.68}$$

Using the Gibbs-Duhem equation

$$-Vdp + SdT + Nd\mu = 0 \tag{10.69}$$

the following useful relations are obtained

$$\frac{\partial \mu}{\partial T} \equiv -s \qquad \frac{\partial \mu}{\partial p} = -\frac{1}{\rho} \tag{10.70}$$

where $s = S/N$ is the entropy per particle and $\rho = V/N$ is the number density. Since the chemical potentials for the solid and liquid phase are equal at the triple point, $\mu_s(p_0,T_0) = \mu_l(p_0,T_0)$, Eq. (10.67) can be written as

$$-s_l(T-T_0) + \frac{1}{\rho_l}(p_l - p_0) = -s_s(T-T_0) + \frac{1}{\rho_s}(p_s - p_0) \tag{10.71}$$

The Young-Laplace equation defines the pressure difference between the inside and the outside of a curved surface [166], which allows us to distinguish between the pressure p_s of a solid cluster and the pressure p_l of a liquid cluster

$$p_l = p_{ext} + \frac{2\gamma_{l\nu}}{r_l}, \qquad p_s = p_{ext} + \frac{2\gamma_{s\nu}}{r_s} \tag{10.72}$$

In both expressions the external pressure, p_{ext}, vanishes since clusters are being modelled in a vacuum. This, in combination with the latent heat of fusion, L,

$$L = (s_l - s_s)T_0 \tag{10.73}$$

and the geometrical relationship which holds if the particles have spherical shape

$$\frac{r_s}{r_l} = \left(\frac{\rho_l}{\rho_s}\right)^{1/3} \tag{10.74}$$

leads to the equation that describes melting point depression

$$1 - \frac{T_m(N)}{T_m(\infty)} = \frac{2}{\rho_s r_s L}\left(\gamma_{s\nu} - \gamma_{l\nu}\left(\frac{\rho_s}{\rho_l}\right)^{2/3}\right) \tag{10.75}$$

For large clusters the leading order of Eq. (10.37), which gives the number of atoms N in an icosahedral cluster, is k^3, where k is the number of shells in the cluster. Since the distance between the atoms in the icosahedral cluster is

approximately the dimer equilibrium distance, r_{de}, the radius of an icosahedral cluster corresponds to $r_s = r_{de}k$. Thus, it follows from the above that r_s scales approximately with $N^{1/3}$.

Since ρ_s/ρ_l is a constant and $r_s \propto N^{1/3}$, the melting temperature of a cluster with N atoms is related to the melting temperature by

$$T_m(N) = T_m(\infty)\left(1 - \frac{\mathcal{C}}{N^{1/3}}\right) \tag{10.76}$$

This means that it is possible to linearly extrapolate the melting temperatures of the different cluster sizes to the bulk melting temperature with the inverse cluster radius $N^{-1/3}$. Smaller clusters, for which the leading order in N is not k^3 are expected to deviate from this line.

Liquid Shell Model Over the years multiple efforts have been made to express a more accurate equation describing the melting point depression. A review of these models can be found in [167]. One improvement can be made by including the possibility of surface melting, first developed by Reiss and Wilson [168] and later developed by Hanszen [169], Sambles [170] and Chushak and Bartell [171] . In this scheme the clusters are assumed to have an inner core and an external liquid shell of thickness δ. The liquid layer over the solid core remains unchanged until the particle cluster transforms completely to a liquid at the melting temperature. The resulting non-linear expression of the dependence of the melting temperature on the cluster size is obtained

$$1 - \frac{T_m(N)}{T_m(\infty)} = \frac{2}{\rho_l L}\left(\frac{\gamma_{sl}}{r-\delta} + \frac{\gamma_{lv}}{r}\left[1 - \left(\frac{\rho_s}{\rho_l}\right)^{2/3}\right]\right) \tag{10.77}$$

This model predicts a lower melting temperature with respect to the inverse of the particle size and is decreased more with increasing radius of the liquid layer. In terms of fitting coefficients this relation can be formulated as

$$T_m(N) = T_m(\infty)\left[1 - \frac{C_1}{N^{1/3}} - \frac{C_2}{N^{1/3} - 2\delta}\right] \tag{10.78}$$

where C_1, C_2 and δ are the fitting parameters and Eq. 10.76 is recovered in the limit $\delta \mapsto 0$, which means that there is no liquid interface. Fig. (10.7) compares Pawlow's linear expression to the liquid shell model with different thicknesses of the liquid layer.

Second-Order Perturbation As an attempt to improve the equation that determines the relation between the cluster′s melting temperature, $T_m(N)$, and the melting temperature of the bulk, $T_m(\infty)$, higher order terms can be included in the Taylor expansion of Eq. (10.68). Second order corrections to

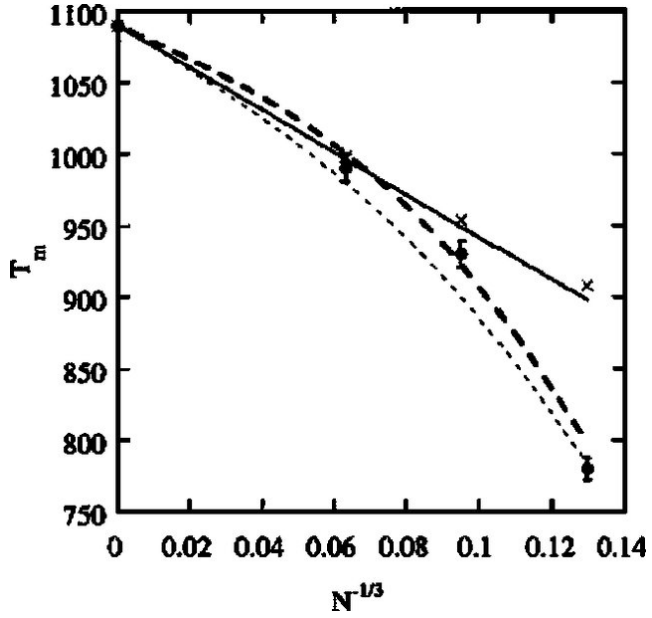

Figure 10.7.: Extrapolation to the bulk melting point $T_m(\infty)$ according to different theoretical results. Melting points of gold clusters from molecular dynamics simulations (black dots), and comparison with different theoretical results: Pawlow's theory [165] (solid line), second order correction from Buffat and Borel [164] (x), liquid-shell model by Sambles [170] (heavy dashed curves), second order corrections to Samble's formula (thin dashed curves). Reprinted with permission from [171]. Copyright 2001 by the American Chemical Society.

Pawlow's model have been obtained by Buffat and Borel [164] and second order corrections to Samble's liquid shell theory have been obtained by Chushak and Bartell [171]. In both cases the solution is not readily expressed in closed form and the resulting equations have to be solved numerically. These, in principle more accurate equations, have many fitting parameters and therefore need more cluster sizes in order to obtain an accurate fit. Due to our small number of cluster melting temperatures obtained, these extrapolation procedures were not considered.

Effect from Edges and Vertices In all of the previously introduced models the underlying assumption was that the clusters are spherical, that is with a uniform finite curvature. This is of course often not the case and especially smaller clusters tend to arrange into energetically favored non-spherical structures. The local variations of curvature, divided into a difference between surface, edges and vertices, induce an anisotropic Laplace pressure affecting (both increasing and decreasing) the melting temperature [172, 173]. The melting temperatures of clusters can therefore lead to size dependent fluctuations or even exceed its bulk value as observed for example in gallium clusters [174–176].

Explicitly including the contribution of edges and vertices in the partition function leads to additional terms in the Gibbs free energy [177]

$$F = Nf(p,T) + a(p,T)N^{2/3} + b(T)\ln N + c(T)N^{1/3} + d(p,T) \quad (10.79)$$

where the first term is the macroscopic term of order NkT. The surface term is of order $N^{2/3}kT$, the next two terms describe translation and the edges which contribute terms of order $kT\ln N$ and $N^{1/3}kT$ respectively. Both the rotation and the vertices are of order kT. The contribution of the edges and vertices is especially of importance for the smallest clusters where the fraction of surface atoms is very high. Yet, for the larger clusters the higher order effects become negligible, leading to a linear dependency of the melting temperatures on the inverse cluster radius. This, in combination with the liquid shell model, causes the smallest clusters to deviate from Pawlow's result. Instead of making use of a complex non-linear function with multiple fitting parameters, it is therefore recommended to extrapolate starting from (a yet to be determined) minimum cluster size.

10.5.3. Icosahedral Overstability

In the previous section it was shown that the melting temperature increases with increasing cluster radius. However, the size dependence of the melting point shows some irregular variations. For example, Frantz [178] studied the melting of small Lennard-Jones clusters containing 25 to 60 atoms and demonstrated that the cluster containing 55 atoms melts above the expected

melting temperature. This study was extended by Senn et al. [155], who obtained the melting temperature of argon clusters in the range from 55 to 309 atoms. In this case deviations from the linear trend in $N^{-1/3}$ were observed for and around magic values of N as well as for small N where the surface-to-volume ratio is large. Furthermore, Senn et al. demonstrated that, due to the icosahedral magic clusters melting at a higher temperature, variations in bulk melting temperatures, T_m^{bulk}, are obtained depending on the selected cluster range for extrapolation.

A systematic selection for the cluster sizes is therefore advisable. However, the above results do not imply that extrapolation with non-magic clusters would lead to better results. Namely, non magic clusters can show some complex behavior which can result in ill defined heat capacity curves. This is in contrast to magic number clusters, which show a well defined melting temperature. Furthermore with increasing atom number the variations in the melting temperature are expected to become less pronounced as the icosahedrals do not preseent the global minimum on the potential hypersurface anymore.

10.5.4. Premelting

Premelting is a phenomena often observed in the computational study of clusters and corresponds to structural rearrangements prior to melting. Solid-solid transitions can be expected for those with non-icosahedral geometries, see for example [179–183], but structural transitions are also observed in energetically favored Mackay icosahedra at finite temperature.

Premelting of 561 and 923-atom Mackay icosahedra has been studied by Doye and Wales [184] who performed constant energy molecular dynamics simulations in which the clusters where heated starting from the Mackay icosahedron. Apart from melting vacancies that are generated at the surface and the resulting ad-atoms diffuse across the surface, they also found that before melting there is a surface solid-to-solid reconstruction in which the atoms of the surface layer rearrange themselves to occupy an Anti-Mackay type packing structure. Such a transition would give rise to a premelting peak in the heat capacity curve.

To understand the origin of the first feature, these authors performed energy minimisations by the conjugate gradient method [185] of structures taken from the MD simulation such that they are free from thermal motions. Since the anti-Mackay overlayer involves 52 fewer atoms than the Mackay layer, the driving force for the reconstruction is the configurational entropy associated with the release of the 52 ad-atoms. These ad-atoms tend to clump together in disordered patches.

A similar study was performed by Noya and Doye [186], who studied the thermal behaviour of 309-atoms Lennard-Jones icosahedral clusters by par-

allel tempering Monte Carlo simulations. The observed heat capacity peak before melting is attributed to coincident with the structural transformation processes. Although they observe the Mackay to anti-Mackay overlayers reconstruction, other type of transformations were also present, such as surface roughening and whole scale transformations. However all transitions were driven by the increase in vibrational entropy, which can be understood from the fact that at zero temperature the equilibrium structure corresponds to the one with lowest energy but at finite temperatures, structures with lowest free energy will be found.

Part IV.

Melting Results

11. Monte Carlo Results

In the preceding chapters the relevant potentials and Monte Carlo method in order to obtain the melting temperature of Kr, Xe, Rn and Og by means of ab-initio methods has been discussed. We are now able to calculate the melting temperature by two different approaches; either by Monte Carlo sampling of finite clusters which can then be extrapolated to the bulk melting temperature, or alternatively by performing periodic simulations at constant pressure which corresponds to direct sampling of the bulk. The results of the two methods are given in section 11.1 and section 11.2 respectively

11.1. Melting Simulations of Rare Gas Clusters

11.1.1. Computational Details

All cluster simulations were performed in the canonical (NVT) ensemble, that is the particle number N, hard-sphere volume V and temperature T were held constant during the simulation. Melting simulations were performed for Mackay icosahedral clusters of size $N = 13$, 55, 147, 309, 561, 923 and 1415 atoms considering two-body interactions only, additional simulations were performed considering two+three-body interactions up to clusters containing 923 atoms. The coordinates of the icosahedral cluster, optimized for the Lennard Jones potential were taken from the Cambridge Cluster database [187]. These coordinates were rescaled to the noble gas dimer equilibrium distances of interest. To avoid the clusters from evaporating, a hard sphere is defined with a radius of one diatomic equilibrium distance larger then the radius of the icosahedral cluster. In order to obtain the inner energy as a function of temperature, 32 temperature trajectories were propagated simultaneously spanning the temperature interval of the melting transition, with a geometrical distribution of temperatures for the chosen interval. Exchanges of configurations are attempted of near-lying temperatures according to the parallel tempering method in order to overcome ergodicity problems and improving convergence. For each simulated temperature three million Monte Carlo cycles were performed of which statistical data was collected from the last one million cycles. During each MC cycle, N configurations are generated by the displacement of a randomly chosen atom, where N is the number of atoms in the cluster. Heat capacities were calculated using the two-body ELJ and three-body EAT potentials which were fitted to reproduce electronic structure calculations, as discussed in section 7.1 and 7.2 respectively.

Two-body interactions are considered over the entire sphere, whereas for the three-body interaction a cut-off radius of $r = 2\sigma$ is employed, where σ is the position of the maximum of the three-body EAT potential. The inner energy of the system $U(T)$ and the heat capacities $C_v(T)$ are obtained as a continuous function of temperature T from the simulation data using the histogram reweighting technique.

11.1.2. Heat Capacity Curves

Fig. 11.1 to 11.6 show the heat capacities for krypton, xenon, radon and oganesson clusters. While the curves are unimodal up to clusters containing 147 atoms, additional peaks are also present in the larger simulated clusters. These additional peaks are associated with surface reconstruction. This phenomenon has been discussed in section 10.5.4. For most of the simulations of the $N = 309$ cluster, no premelting peaks are observed. However, the heat capacity curves of xenon (including 2-body interactions only) and the NR oganesson (including 2+3-body interactions) clusters have a small shoulder. The temperature at which the surface reconstruction occurs is for these simulations thus very close to the melting transition. For the clusters of size $N \geq 561$, the premelting peaks appear at temperatures well below the temperature of the solid to liquid phase transition and are therefore not expected to affect the temperature of the melting transition. Oganesson, simulated with the spin-orbit corrected potential (including 2+3-body interactions) behaves quite differently to the above; only the $N = 923$ cluster shows a small premelting shoulder, the smaller clusters are unimodal. This behavior is most likely due to the strong three-body repulsion which influences the potential landscape.

The melting temperatures are determined from the equilibrium heat capacity as the maximum of the heat capacity curves and are listed in table 11.1.

11.1.3. Extrapolation to the Bulk

By plotting the melting temperatures as a function of $N^{-1/3}$, as shown in Fig. 11.7 and 11.8, the melting temperatures exhibit a linear trend at larger N values and can be extrapolated to the bulk value, $N = \infty$, corresponding to $N^{-1/3} = 0$. As predicted in section 10.5.2, the two smallest clusters of size $N = 13$ and $N = 55$ deviate from this linear trend and are therefore not considered in the extrapolation. The extrapolated melting temperatures are listed in Table 11.2, where the two-body melting temperature is obtained by extrapolation of the clusters $N = 147$ to 1415. Three-body corrections are taken as the difference in melting temperature when extrapolating clusters of size $N = 147$ to 923 including two- versus two+three-body interactions.

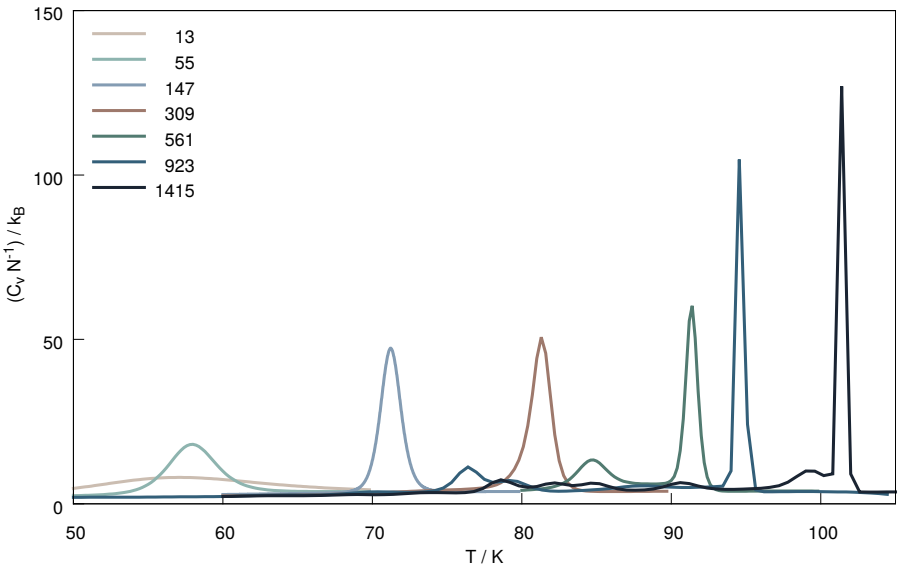

(a) Krypton, 2 body

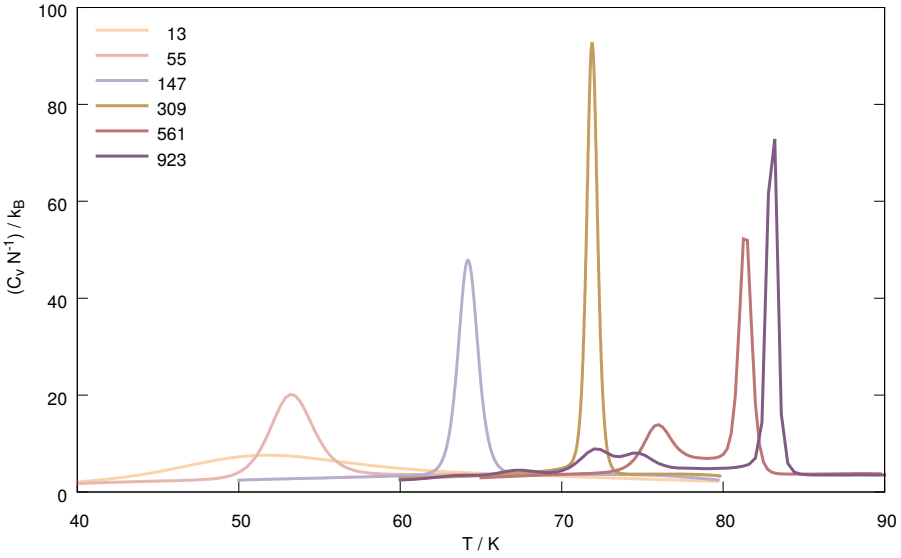

(b) Krypton, 2 + 3 body

Figure 11.1.: Heat capacities as a function of temperature per atom for the Mackay icosahedral clusters with up to 1415 atoms for krypton. Top, heat capacity curves obtained considering 2-body interactions only, using the ELJ potential. Bottom, obtained heat capacities considering 2- and 3-body interactions, computed with the ELJ and EAT potentials respectively.

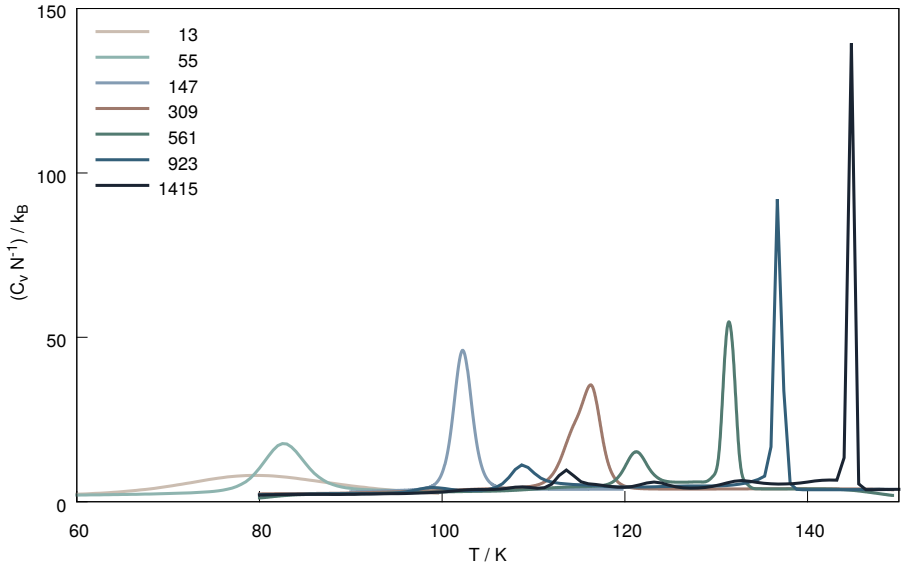

(a) Xenon, 2 body

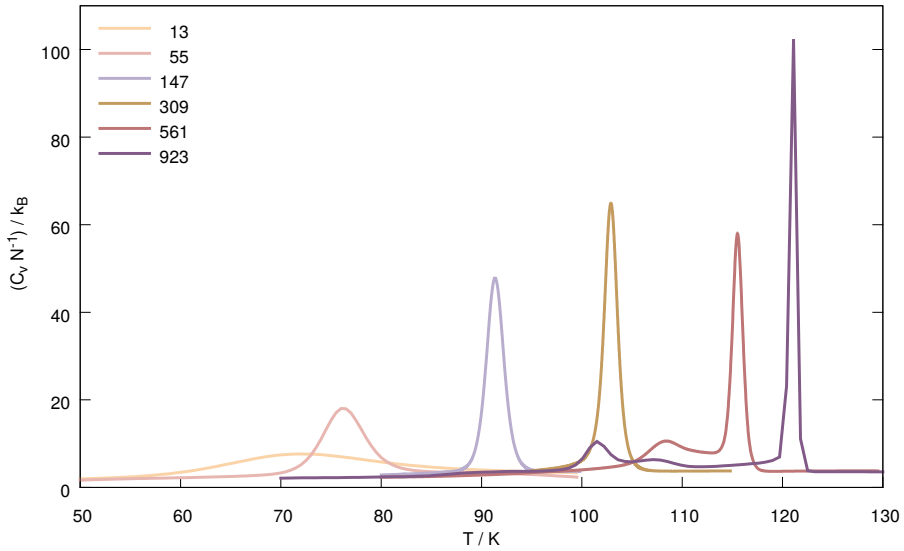

(b) Xenon, 2 + 3 body

Figure 11.2.: Heat capacities as a function of temperature per atom for the Mackay icosahedral clusters with up to 1415 atoms for xenon. Top, heat capacity curves obtained considering 2-body interactions only, using the ELJ potential. Bottom, obtained heat capacities considering 2- and 3-body interactions, computed with the ELJ and EAT potentials respectively.

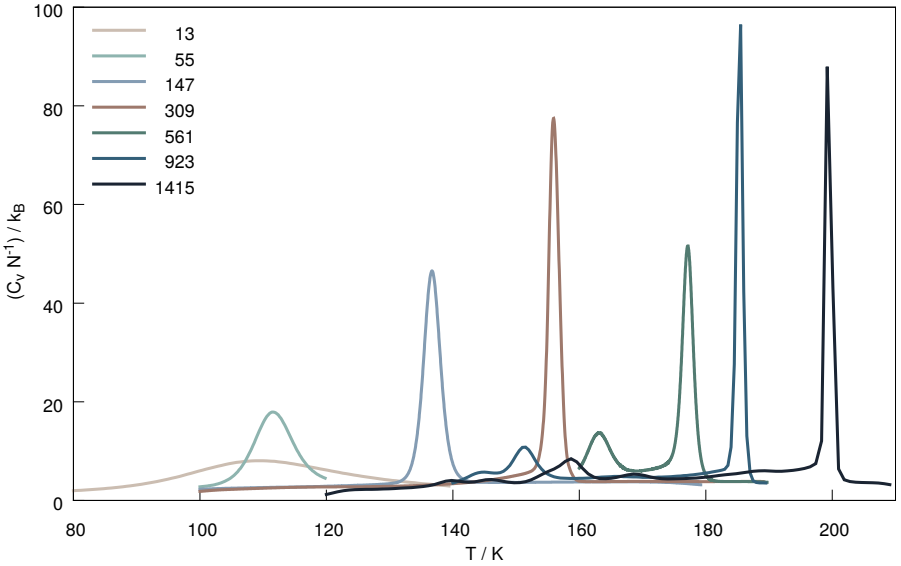

(a) Radon, 2 body

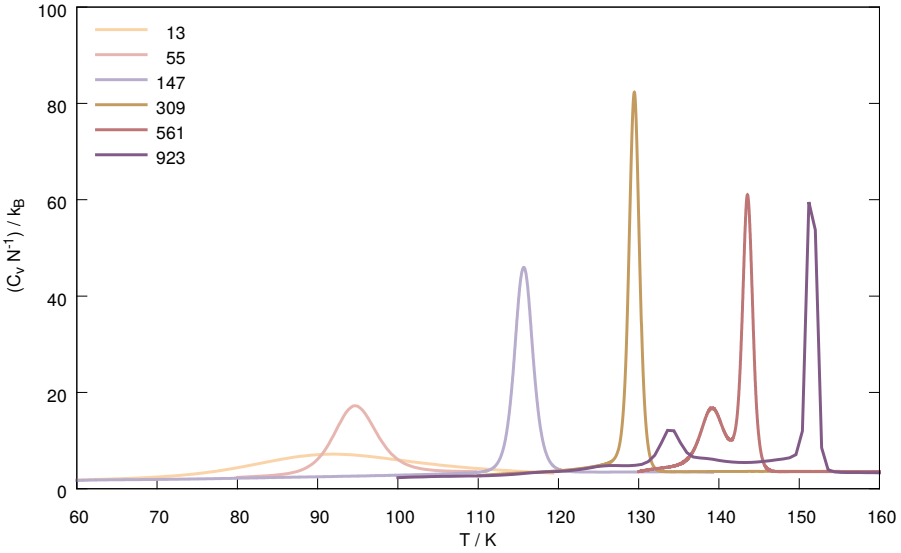

(b) Radon, 2 + 3 body

Figure 11.3.: Heat capacities as a function of temperature per atom for the Mackay icosahedral clusters with up to 1415 atoms for radon. Top, heat capacity curves obtained considering 2-body interactions only, using the ELJ potential. Bottom, obtained heat capacities considering 2- and 3-body interactions, computed with the ELJ and EAT potentials respectively.

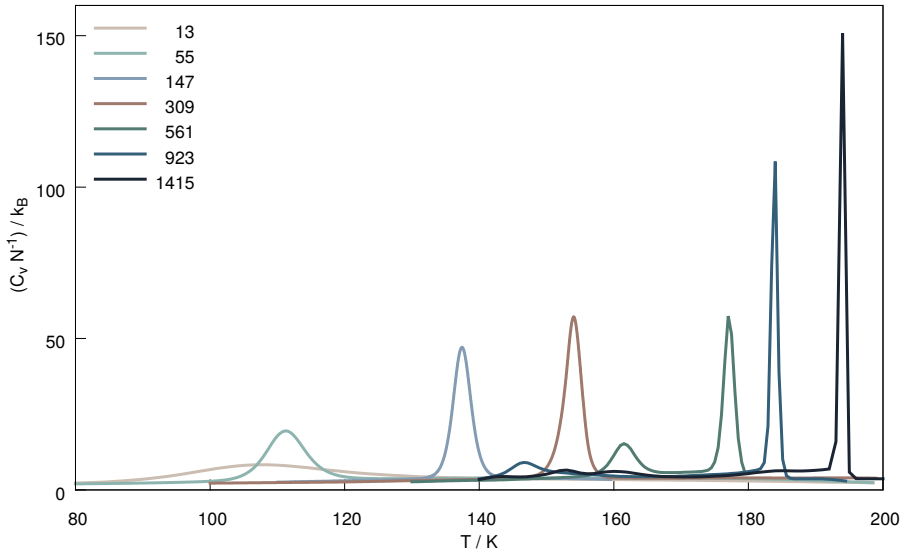

(a) Oganesson, NR, 2 body

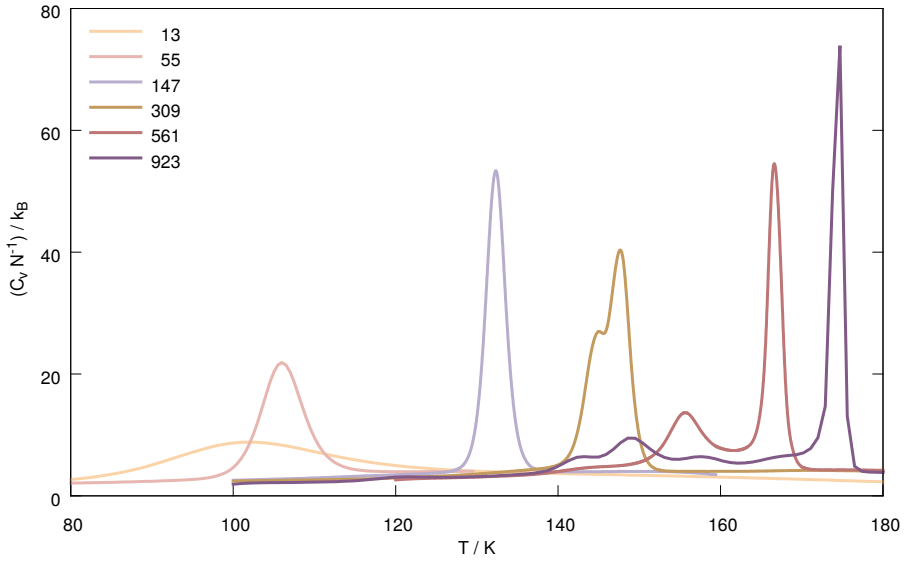

(b) Oganesson, NR, 2 + 3 body

Figure 11.4.: Heat capacities as a function of temperature per atom for the Mackay icosahedral clusters with up to 1415 atoms for oganesson at the non-relativistic (NR) level of theory. Top, heat capacity curves obtained considering 2-body interactions only, using the ELJ potential. Bottom, obtained heat capacities considering 2- and 3-body interactions, computed with the ELJ and EAT potentials respectively.

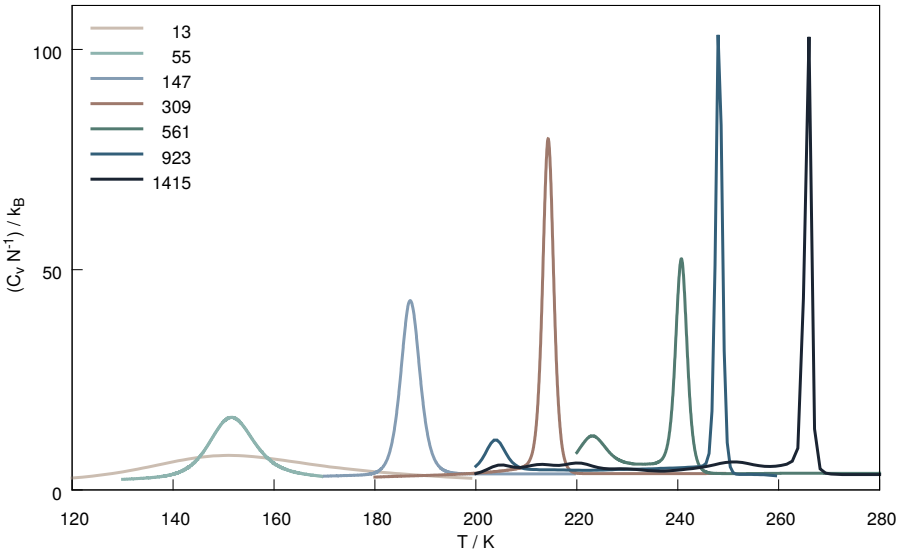

(a) Oganesson, SR, 2 body

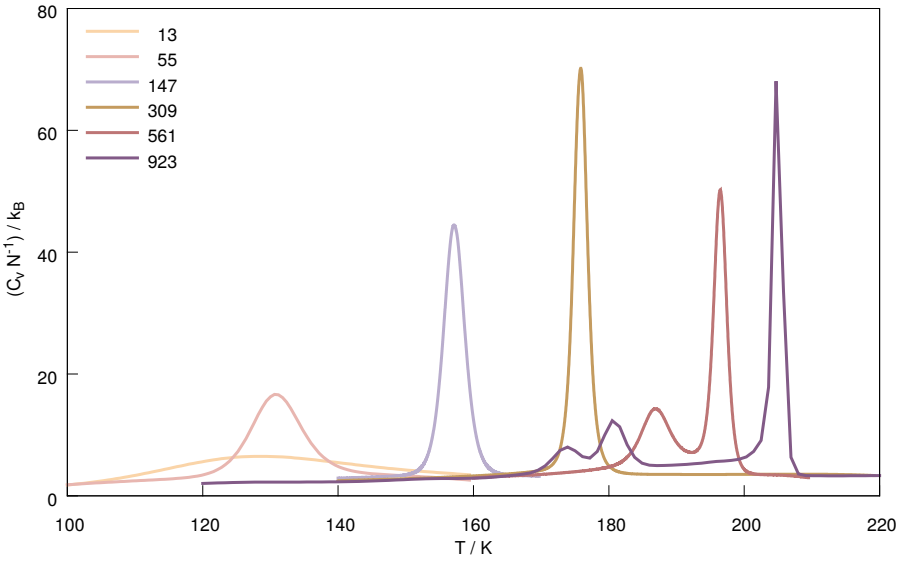

(b) Oganesson, SR, 2 + 3 body

Figure 11.5.: Heat capacities as a function of temperature per atom for the Mackay icosahedral clusters with up to 1415 atoms for oganesson at the scalar relativistic (SR) level of theory. Top, heat capacity curves obtained considering 2-body interactions only, using the ELJ potential. Bottom, obtained heat capacities considering 2- and 3-body interactions, computed with the ELJ and EAT potentials respectively.

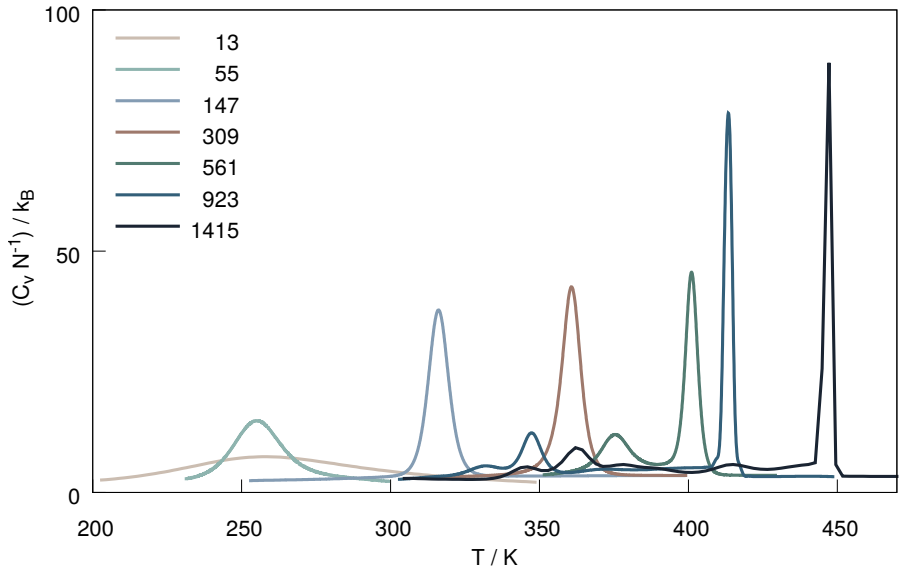

(a) Oganesson, SR + X2C, 2 body

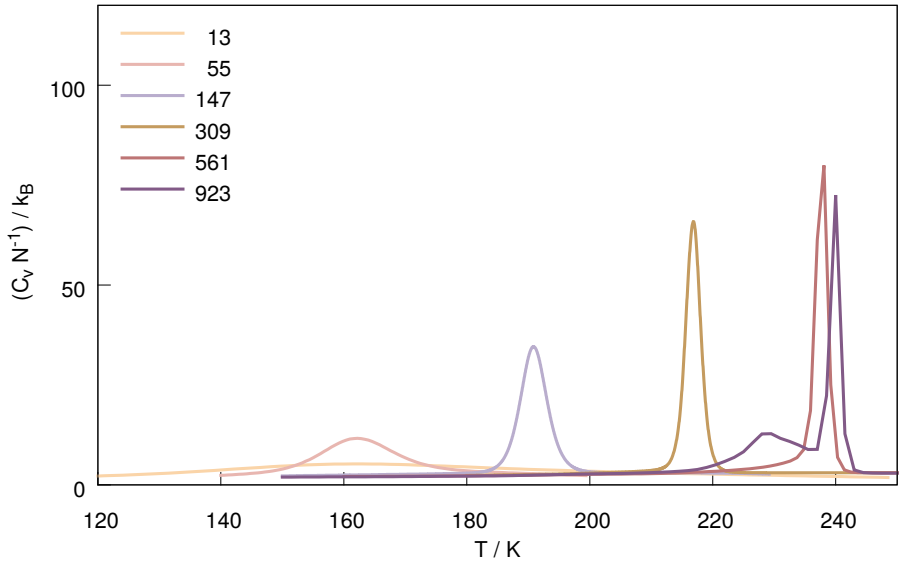

(b) Oganesson, SR + X2C, 2 + 3 body

Figure 11.6.: Heat capacities as a function of temperature per atom for the Mackay icosahedral clusters with up to 1415 atoms for oganesson at spin-orbit corrected (SR+X2C) levels of theory. Top, heat capacity curves obtained considering 2-body interactions only, using the ELJ potential. Bottom, obtained heat capacities considering 2- and 3-body interactions, computed with the ELJ and EAT potentials respectively.

Table 11.1.: Melting temperatures in Kelvin for the simulated rare gas clusters extracted from the heat capacity curves.

	N	13	55	147	309	561	923	1415
Krypton								
	2 body	57.08	57.94	71.22	81.3	91.37	94.55	101.40
	2+3 body	51.79	53.27	64.19	71.88	81.37	83.60	
Xenon								
	2 body	79.56	82.66	102.26	116.28	129.85	136.70	144.80
	2+3 body	72.07	76.22	91.36	102.89	115.50	121.10	
Radon								
	2 body	109.43	111.59	136.78	155.81	177.14	185.43	199.20
	2+3 body	91.09	94.68	115.71	129.50	143.50	151.49	
Og NR								
	2 body	107.73	111.36	137.46	154.00	175.86	183.98	194.00
	2+3 body	101.99	106.00	132.36	147.68	166.56	174.63	
Og SR								
	2 body	151.07	151.58	187.0	214.3	240.8	248.08	266.00
	2+3 body	128.5	130.83	157.14	175.91	196.49	204.7	
Og SR+X2C								
	2 body	257.93	255.07	316	360.76	401.09	413.49	440.3
	2+3 body	162.16	162.17	190.82	216.96	237.5	238.5	

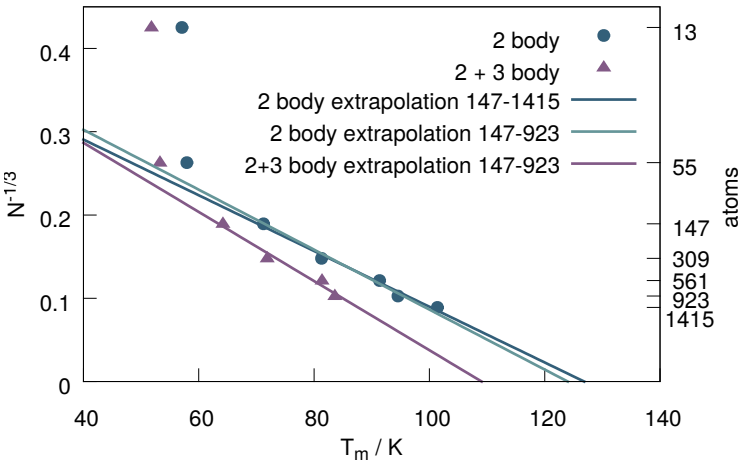

(a) Krypton

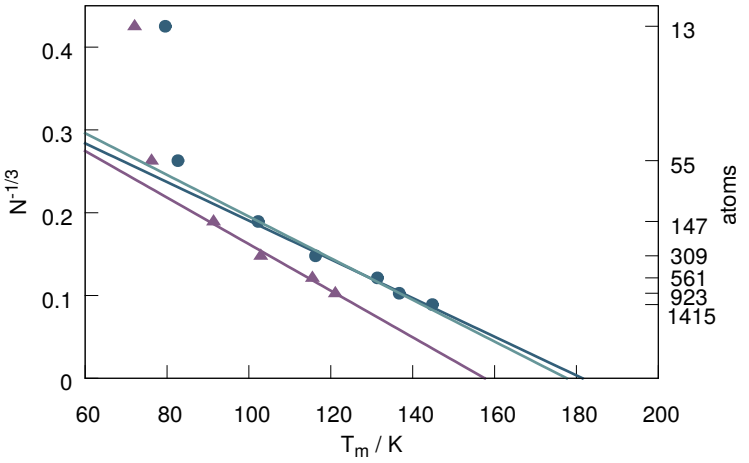

(b) Xenon

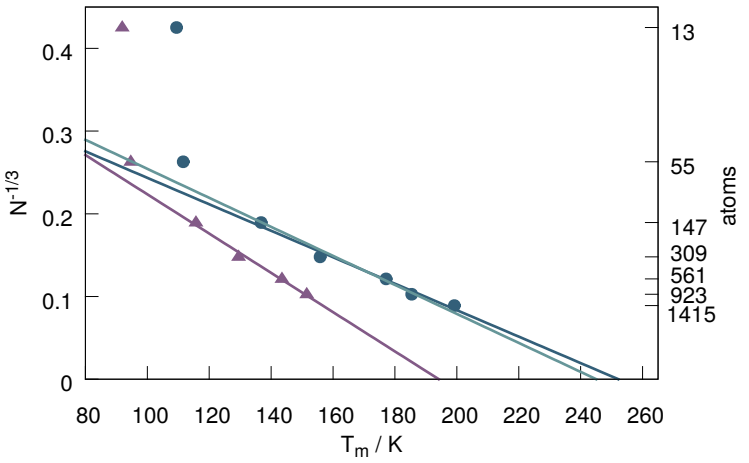

(c) Radon

Figure 11.7.: Extrapolated melting temperatures for krypton, xenon and radon, obtained using two-body ELJ interactions (circles) and three-body-corrected EAT values (triangles). The blue line corresponds to the linear fit of the melting temperatures of the $N = 147 - 1415$ ELJ clusters, light blue to the melting temperatures of the $N = 147 - 923$ ELJ clusters and the purple line corresponds to the linear fit through the $N = 147 - 923$ cluster including three-body EAT corrections.

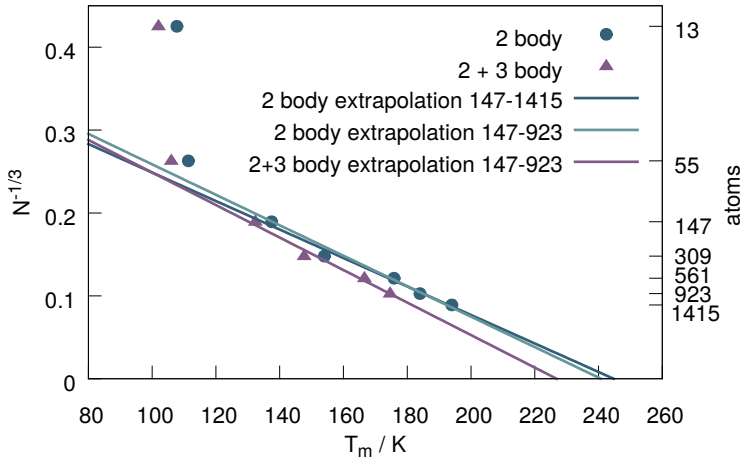

(a) Og NR

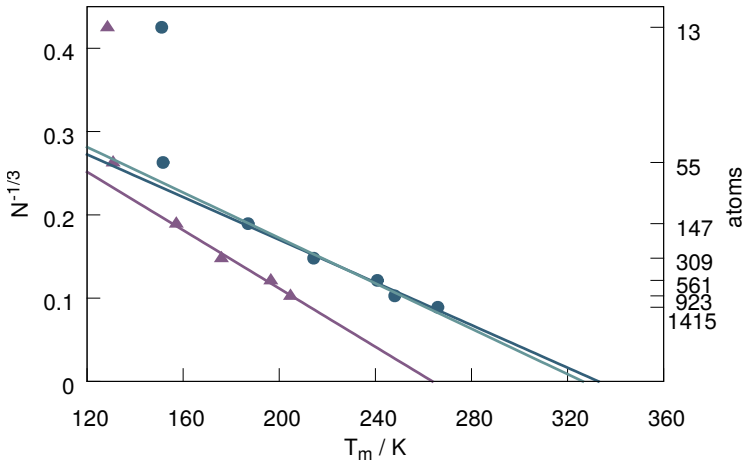

(b) Og SR

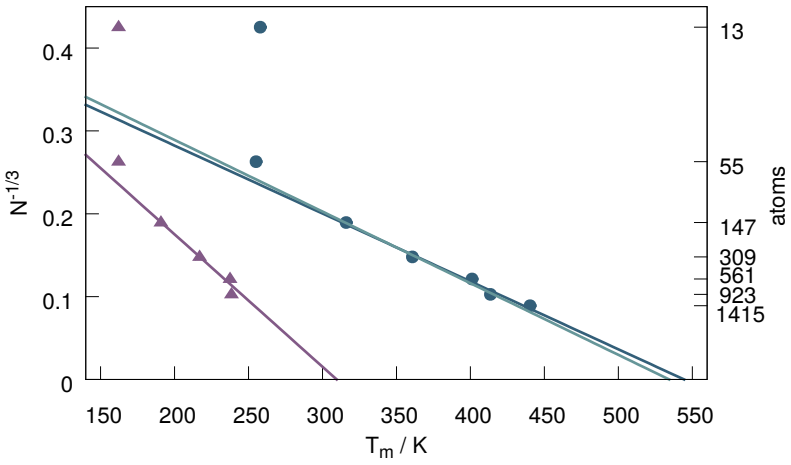

(c) Og SR+X2C

Figure 11.8.: Extrapolated melting temperatures for oganesson at the non-relativistic (NR), scalar relativistic (SR) and spin-orbit (RX2C) levels of theory, obtained using two-body ELJ interactions (circles) and three-body-corrected EAT values (triangles). The blue line corresponds to the linear fit of the melting temperatures of the $N = 147 - 1415$ ELJ clusters, light blue to the melting temperatures of the $N = 147 - 923$ ELJ clusters and the purple line corresponds to the linear fit through the $N = 147 - 923$ cluster including 3-body EAT corrections.

Table 11.2.: Melting temperatures in Kelvin obtained by linear extrapolation of $N^{-1/3}$ to the bulk melting temperature.

	N	2 body	2+3 body	$\Delta_{(2b-3b)}$
Krypton				
	$[147-1415]$	126.85	-	-
	$[147-923]$	124.22	109.06	15.16
	Δ	2.63		
Xenon				
	$[147-1415]$	181.47	-	-
	$[147-923]$	178.29	157.60	20.69
	Δ	3.18		
Radon				
	$[147-1415]$	252.16	-	-
	$[147-923]$	246.02	194.15	51.87
	Δ	6.14		
Og. NR				
	$[147-1415]$	244.65	-	-
	$[147-923]$	242.38	226.86	15.51
	Δ	2.27		
Og. SR.				
	$[147-1415]$	332.83	-	-
	$[147-923]$	326.79	263.75	63.04
	Δ	6.04		
Og. RX2C				
	$[147-1415]$	544.4	–	–
	$[147-923]$	534.34	309.59	224.75
	Δ	10.06		

11.2. Melting Simulations of Periodic Cells

11.2.1. Computational Details

Melting of the infinite crystals was simulated directly through periodic boundary conditions using face-centered cubic (fcc) samples. The simulations were performed in the isobaric-isothermal ensemble (NPT), that is particle number N and temperature T were held constant but the sample cells were allowed to change volume V to remain at atmospheric pressure P (1 bar) throughout the simulation.
Simulations were performed for fcc cells containing $N = 4k^3 = 32, 108, 256, 500$ and 864 atoms considering two-body ELJ forces. A spherical cut-off for the two-body potential of $\frac{1}{2}L$ is applied for consistency with the minimum image convention, where L is the length of the simulation cell. Additional simulations were performed considering two-body ELJ plus three-body EAT interactions for fcc cells up to 256 atoms. The three-body contributions were calculated up to $r = 2\sigma$, and for the smaller cells as defined in section 10.2.4. In the same manner as for the cluster simulations, the 32 temperature trajectories were propagated simultaneously spanning the temperature interval of the melting transition, with a geometrical distribution of temperatures for the chosen interval and the temperature trajectories were connected through the parallel tempering method. For each simulated temperature, three million Monte Carlo cycles were performed of which the average enthalpy, $H(T)$, was collected from the last million MC cycles. During each MC cycle, N configurations were generated by the displacement of a randomly chosen atom, where N is the number of atoms in the simulation cell. The enthalpy $H(T)$ and the heat capacities $C_p(T)$ are obtained as a continuous function of temperature from the simulation data using the histogram reweighting technique.

Histograms for NPT simulations

During a NPT parallel tempering Monte Carlo simulation the count of occurrence is not only stored for the different temperatures but is also binned as a function of volume. Fig. 11.9 shows the energy-volume histograms for trajectories 8, 10, 12, 14 and 16 of a radon NPT simulation for a simulation cell containing 108 atoms. The internal energy U grows horizontally from left to right and the volume V grows vertically from bottom to top. The heat capacity $C_p(T)$ is given on the bottom right, where crosses denote the discrete average energies from the 32 simulated temperatures and the continuous curve is obtained from the, in this case two dimensional, multi-histogram analysis. These graphs demonstrate nicely that during the solid to liquid phase transition in the NPT ensemble both the the inner energy and the volume increase.

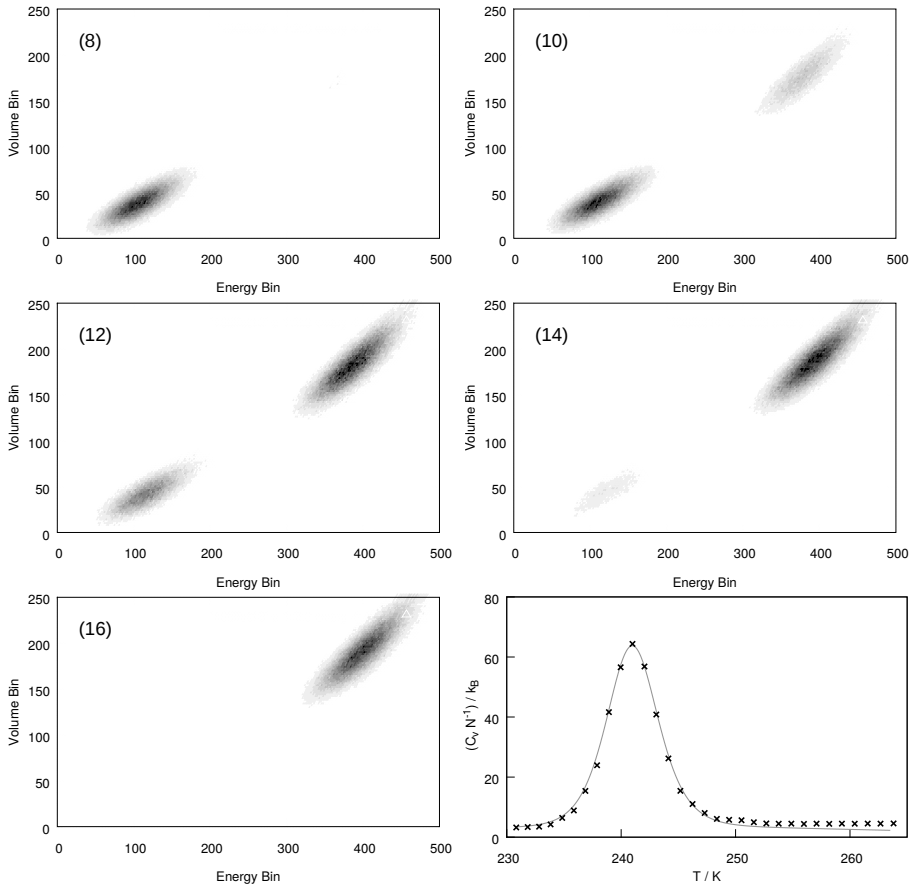

Figure 11.9.: Histograms $N(U, V)$ obtained for a cell with $N = 108$ radon atoms simulated in the NPT ensemble with periodic boundary conditions. In brackets the temperature trajectory number is given. Right bottom shows the heat capacity $C_p(T)$ (crosses) for the discrete 32 simulated temperatures. In grey the continuous curve obtained with the multi-histogram analysis is shown.

11.2.2. Results

Heat capacities per atom for the simulated cells are shown in Figs. 11.12 and 11.15. Left, heat capacity curves obtained considering two-body ELJ interactions only. Right, obtained heat capacities considering two- and three-body interactions, computed with the ELJ and EAT potentials respectively. Opposed to the melting simulations of the clusters, no additional premelting peaks are observed. This is as expected as the periodic cells are in absence of a surface and therefore no surface reconstructions or structural phase transitions occur. The melting temperatures are listen in table 11.3.

11.2.3. Energy Convergence

The total two- and three-body energy contribution for an equilibrated liquid cell as a function of the cutoff radius is demonstrated in Fig. 11.16. Vertical solid lines denote the cutoff radius for the different simulated cell sizes to ensure the minimal image convention is satisfied. The correlation between the melting temperature and the total interaction becomes apparent from this figure. For the smallest cell considered, containing 32 atoms, the total energy contribution is not converged. This explains the large deviation with respect to the melting temperatures of the larger cells. The melting temperature of the 108 atomic cell is already in good agreement with the $N = 864$ cell. This is not only because the energy is close to converged, but also for the reason that the contribution beyond the cutoff distance is approximated by the tail correction. For each of the simulated elements, the 864 cell has a very small difference in melting temperature compared to the $N = 500$ cell and sometimes even lies below the melting temperature of the $N = 500$ cell. It is therefore concluded that for the $N = 864$ cell the melting temperature has converged and lies within the range of statistical error.

Three-body corrections are estimated from the difference in melting temperature between the two-body only and two+three-body $N = 256$ cell. The largest contribution to the error is expected to evolve from this approximation since tail corrections are not considered for the three-body contributions. Besides this, the three body correction is determined from a rather small cell with only three-body contributions considered up to $r_{co} = 2\sigma$.

11.2.4. Densities

Fig 11.17 shows the temperature dependence of the densities for the simulated rare gases, and in particular the densities shortly before and after melting are listed in table 11.5. Two-body densities are extracted from the $N = 864$ simulation cells and three-body corrected values are extracted from the $N = 256$ simulation cell. As a reference, table 11.4 contains results from solid-state calculations for the fcc crystals using the two-body ELJ and three-body EAT terms as well as the classical 4-body Drude term and the 2-body vibrational contributions. The used masses are listed in table 11.5 In the following the densities for the individual elements are given and compared to experimental findings.

Krypton The density of frozen polycrystalline krypton has been experimentally obtained by Figgins and Smith in 1960 [188] using X-ray diffractive methods, the same method used to determine the thermodynamic properties of solidified argon [189]. Figgins obtained the density of solid krypton between 20 and 90 K (3.078 g/cm^3 at 20 K and 2.893 g/cm^3 at 90 K) .

Calado et al. [190] measured the liquid density of krypton close to the melting point and determined it to be 2.4517 g/cm^3 at 115.77 K. The latest experimental data is obtained in 1980 by Albuquerque et al. [191] who obtained a density of (2.3483 to 2.1983) g/cm^3 for the temperature range of $T = (129.32$ to $147.08)$ K.

Before melting starts we obtain a density of solid krypton of 2.7 g/cm^3 (106 K), which slightly decreases to 2.3 g/cm^3 (108 K) for the liquid phase. This value is in excellent agreement with experimental results.

Xenon Studies on the densities of xenon at normal pressure are in principle the most easy to obtain in comparison to the other noble gases, since xenon is not radioactive and offers the widest accessible range of temperatures at normal pressures. The first measurements on the density of solid xenon date back to Sears et al. [192] and Eatwell et al. [193] who carried out measurements in the 1960s on the expansivity and density of frozen polycrystalline xenon according to the same x-ray diffractive method as for argon and krypton. A density of of 3.694 g/cm^3 and 3.689 g/cm^3 at 60 K by Sears and Eatwell was obtained respectively.

The density of liquid xenon was determined by Leadbetter et al. [194] according to the bulk density method, where the density of a liquid is determined by condensing a known mass of gas into a volume-calibrated glass capillary tube. They obtained a liquid density of 2.980 g/cm^3 at 161.9 K. A summary of the liquid density of krypton and xenon around the melting point can be found in [195].

Regarding the MC results, the solid density (3.3 g/cm^3 at 152 K) is lower

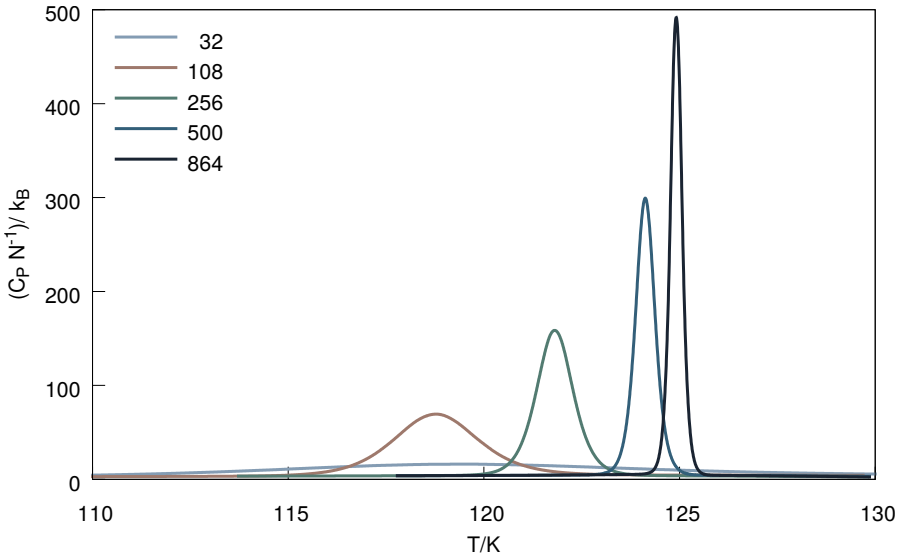

(a) krypton, 2 body

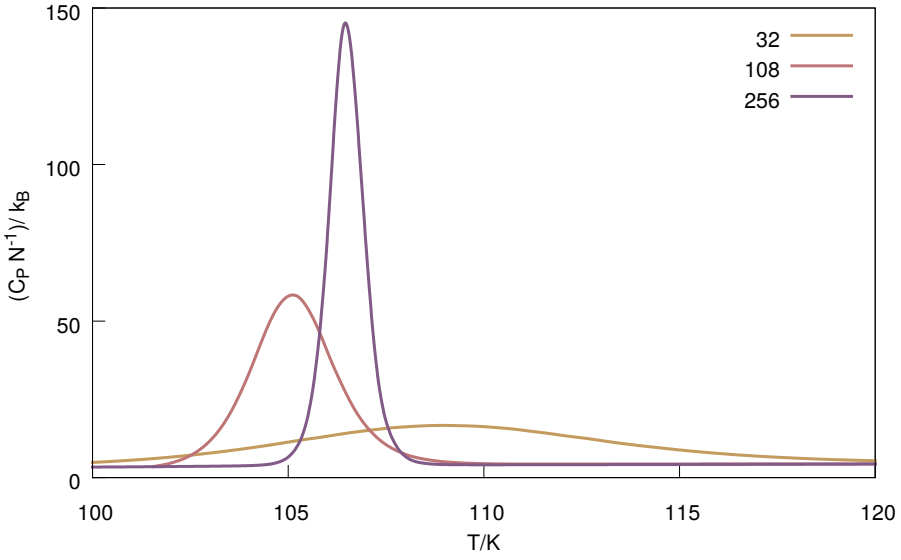

(b) krypton, 2 + 3 body

Figure 11.10.: Heat capacities per atom for simulations with periodic boundary conditions for krypton. Top, heat capacity curves obtained considering two-body ELJ interactions. Bottom, obtained heat capacities considering two- and three-body interactions, computed with the ELJ and EAT potentials respectively.

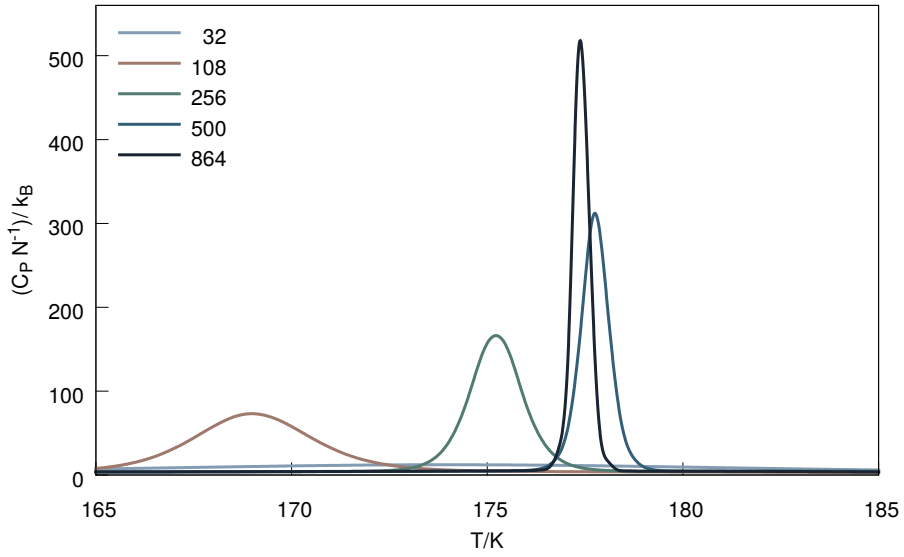

(a) xenon, 2 body

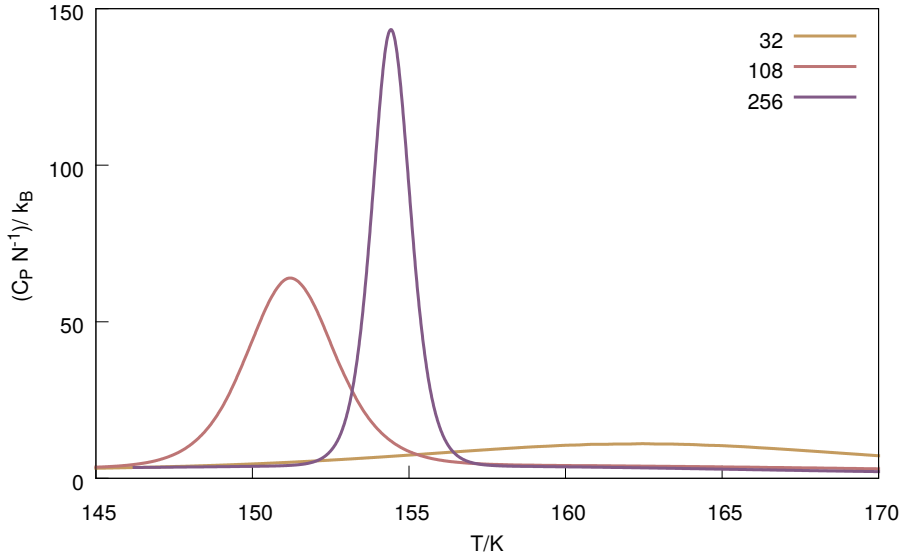

(b) xenon, 2 + 3 body

Figure 11.11.: Heat capacities per atom for simulations with periodic boundary conditions for xenon. Top, heat capacity curves obtained considering two-body ELJ interactions. Bottom, obtained heat capacities considering two- and three-body interactions, computed with the ELJ and EAT potentials respectively.

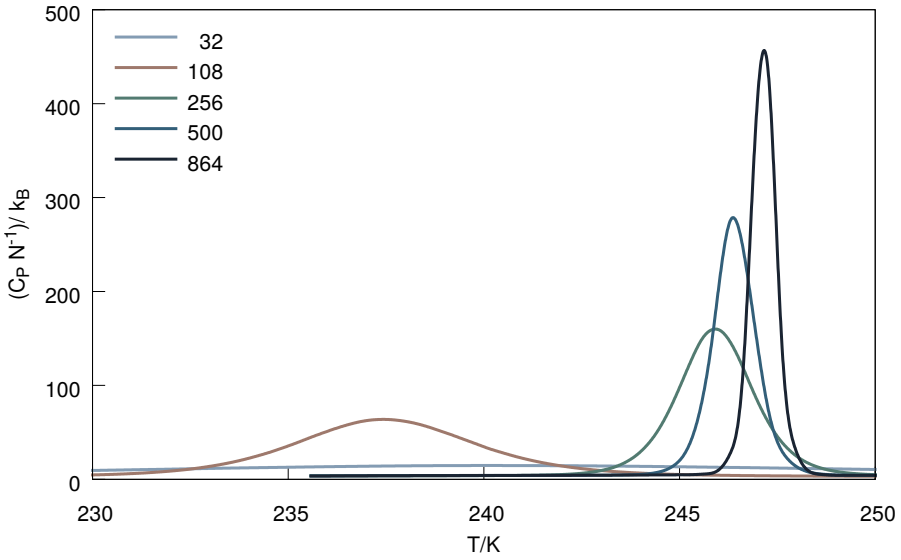

(a) radon, 2 body

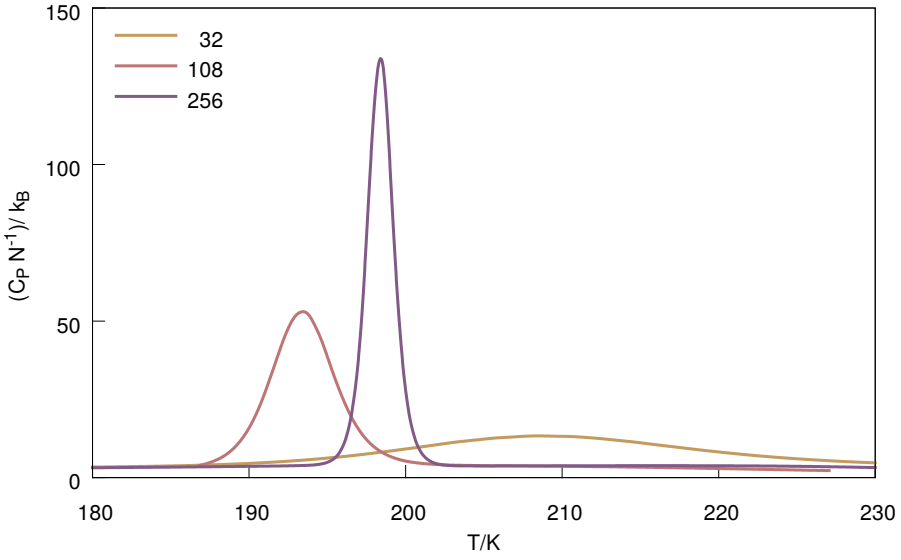

(b) radon, 2 + 3 body

Figure 11.12.: Heat capacities per atom for simulations with periodic boundary conditions for radon. Top, heat capacity curves obtained considering two-body ELJ interactions. Bottom, obtained heat capacities considering two- and three-body interactions, computed with the ELJ and EAT potentials respectively.

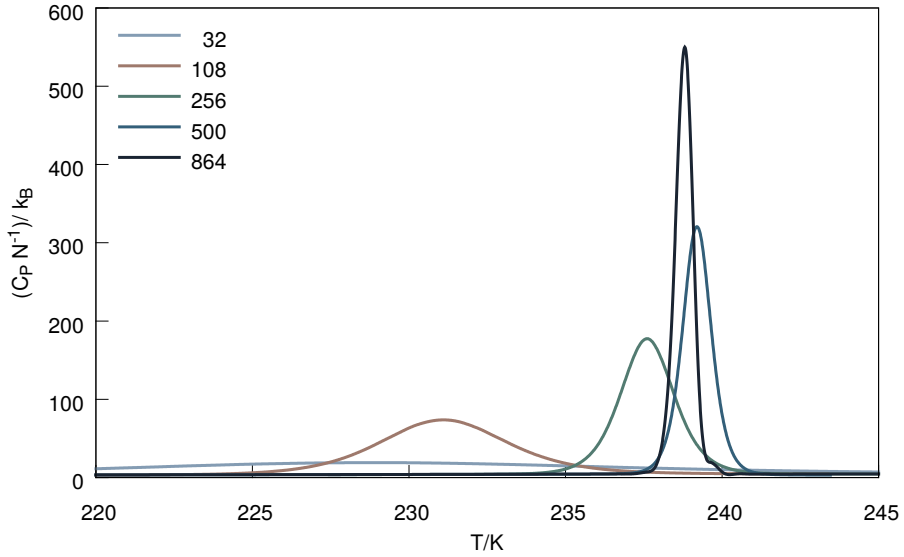

(a) Oganesson, NR,2 body

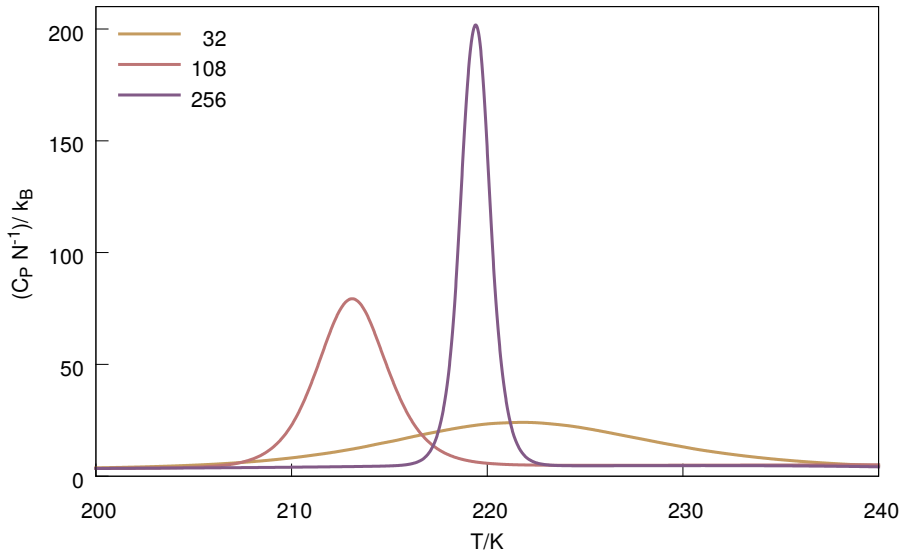

(b) Oganesson, NR,2 + 3 body

Figure 11.13.: Heat capacities per atom for simulations with periodic boundary conditions for oganesson non-relativistic (NR) level of theory. Left, heat capacity curves obtained considering two-body ELJ interactions. Right, obtained heat capacities considering two- and three-body interactions, computed with the ELJ and EAT potentials respectively.

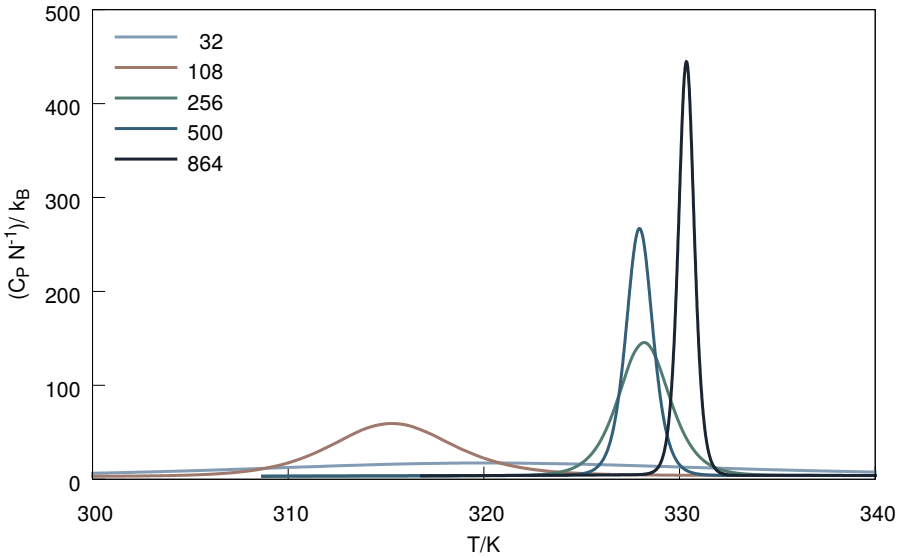

(a) Oganesson, SR, 2 body

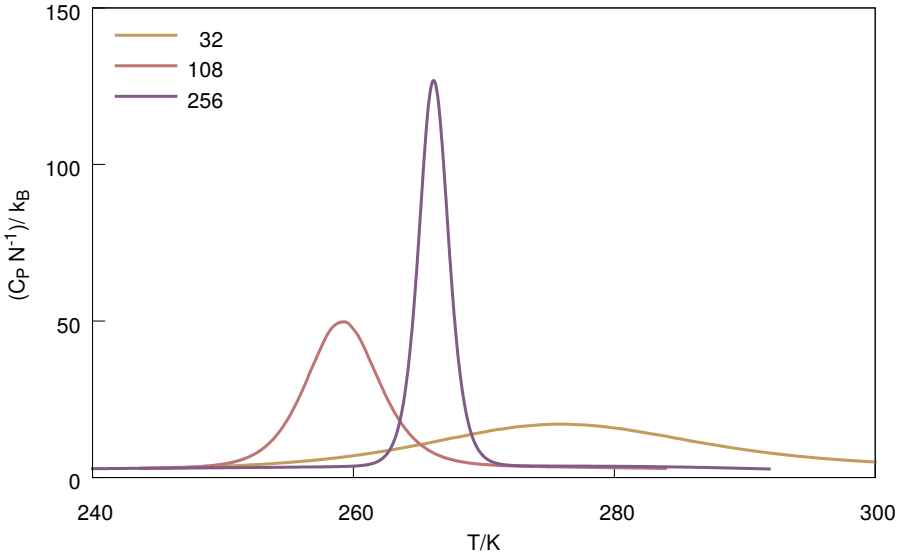

(b) Oganesson, SR, 2 + 3 body

Figure 11.14.: Heat capacities per atom for simulations with periodic boundary conditions for oganesson at scalar relativistic (SR+X2C) levels of theory. Left, heat capacity curves obtained considering two-body ELJ interactions. Right, obtained heat capacities considering two- and three-body interactions, computed with the ELJ and EAT potentials respectively.

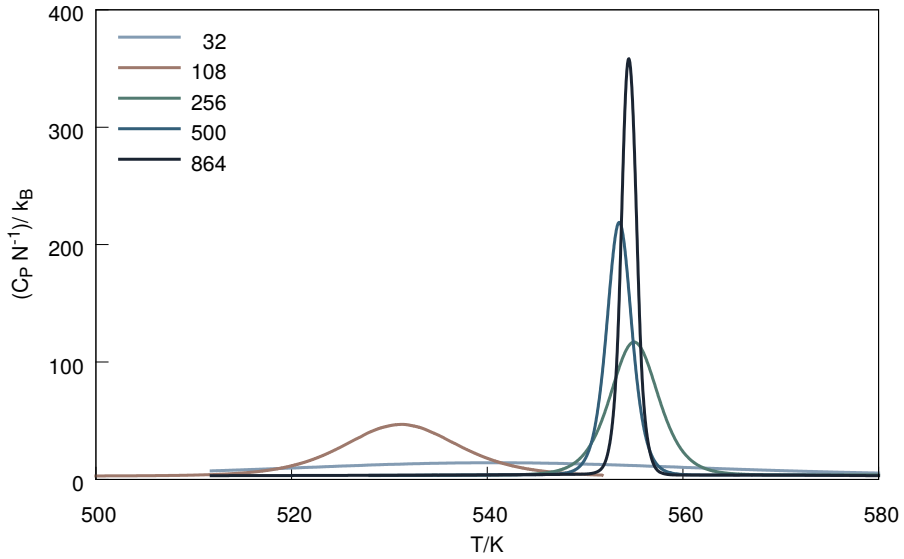

(a) Oganesson, SR + SO, 2 body

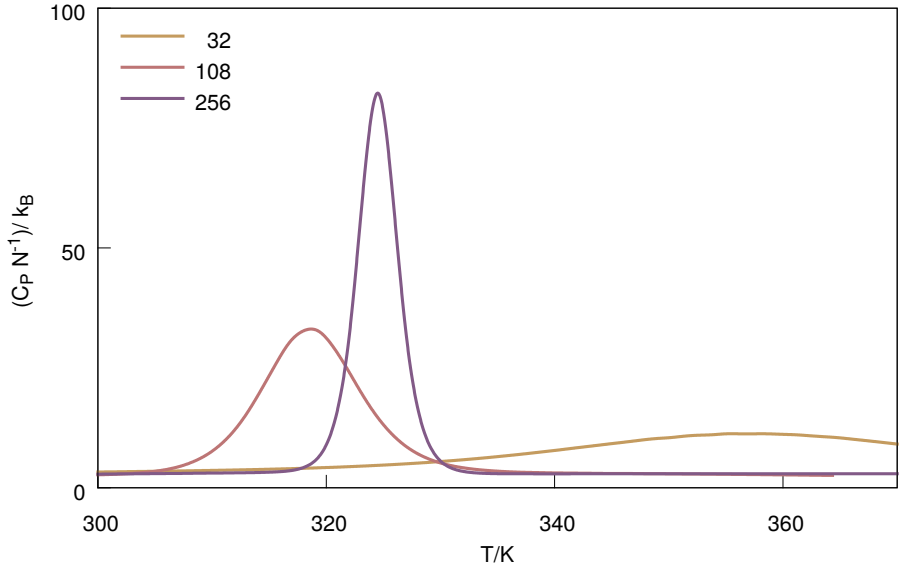

(b) Oganesson, SR+X2C, 2 + 3 body

Figure 11.15.: Heat capacities per atom for simulations with periodic boundary conditions for oganesson at spin-orbit corrected (SR+X2C) levels of theory. Left, heat capacity curves obtained considering two-body ELJ interactions. Right, obtained heat capacities considering two- and three-body interactions, computed with the ELJ and EAT potentials respectively.

Table 11.3.: Periodic NPT melting temperatures extracted from the heat capacity curves of the rare gas elements using different cell sizes.

	N	32	108	256	500	864
Krypton						
	2 body	119.35	118.77	121.81	124.13	124.91
	2+3 body	119.00	105.10	106.42		
	$\Delta_{(2b-3b)}$	10.36	13.67	15.40		
Xenon						
	2 body	173.98	168.98	175.22	177.74	176.60
	2+3 body	162.33	151.22	154.44		
	$\Delta_{(2b-3b)}$	11.65	17.76	20.78		
Radon						
	2 body	240.30	237.45	245.92	246.31	247.18
	2+3 body	208.83	193.39	198.46		
	$\Delta_{(2b-3b)}$	31.47	44.06	47.46		
Og. NR						
	2 body	228.81	231.09	237.61	239.20	238.83
	2+3 body	221.67	213.06	219.43		
	$\Delta_{(2b-3b)}$	7.14	18.03	18.18		
Og. SR						
	2 body	320.07	315.29	328.19	327.94	330.35
	2+3 body	275.94	259.15	266.18		
	$\Delta_{(2b-3b)}$	44.13	56.14	62.01		
Og. RX2C						
	2 body	540.56	531.16	555	553.48	554.44
	2+3 body	357.21	318.55	324.53		
	$\Delta_{(2b-3b)}$	183.35	212.61	230.46		

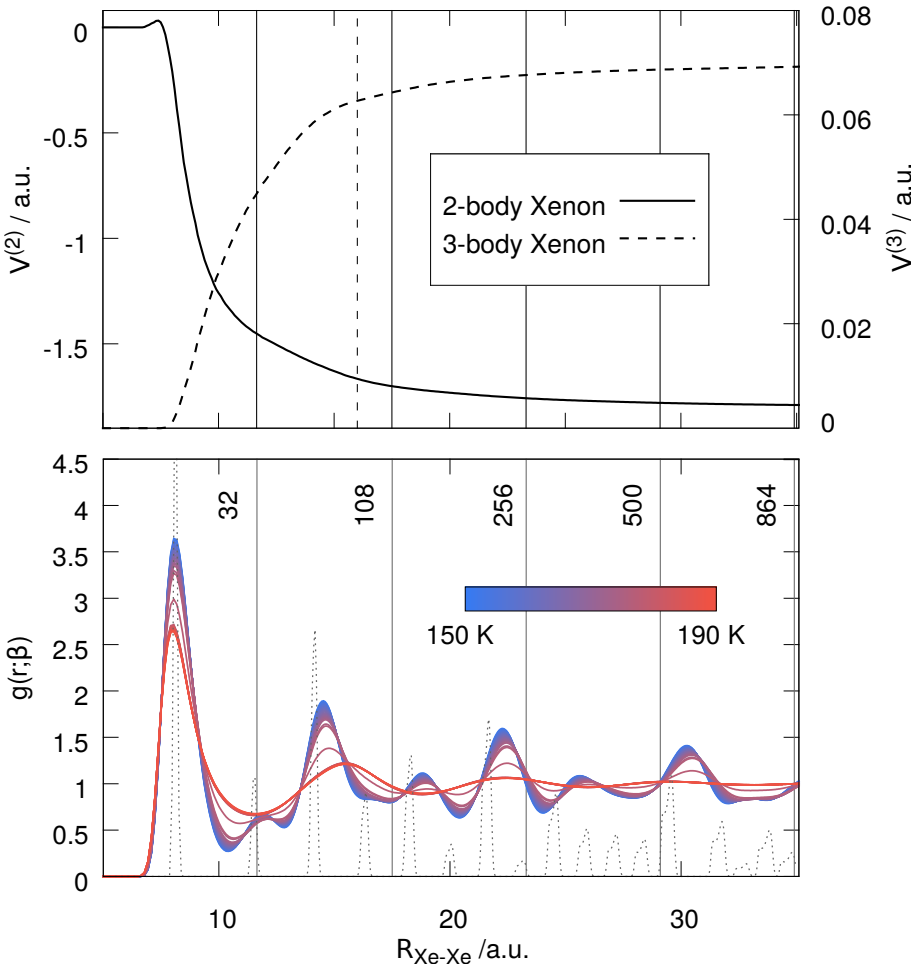

Figure 11.16.: (Top figure) The total two (solid line) and three body (dotted line) contribution as a function of the cut-off radius. The vertical lines denote the spherical two-body cutoff radius that is implemented for the different simulated sizes such that the minimum image convention is satisfied. The vertical dashed line corresponds to the three body cut-off radius, which is held fixed for the different sample sizes.
(Bottom figure) Pair distribution function $g(r, \beta)$ of Xenon between 150 and 190 K for a simulation with periodic boundary conditions. Near T_m the fcc lattice breaks down to form a disordered fluid. The gray dotted line indicates a near perfect initial fcc structure.

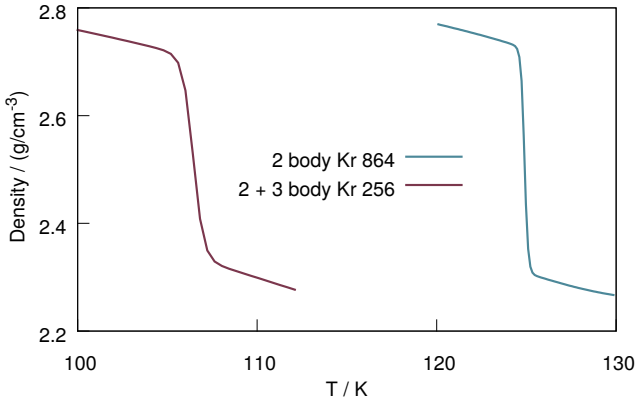

(a) Krypton

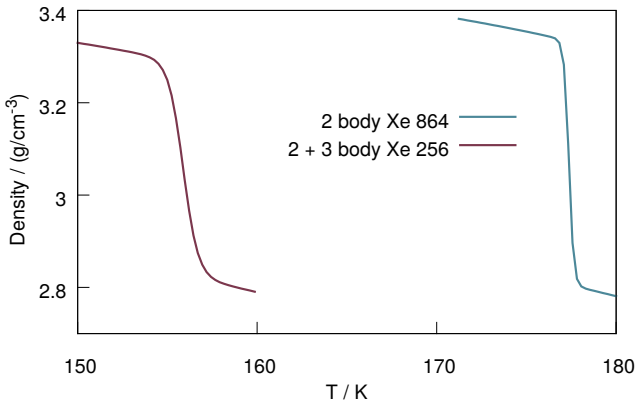

(b) Xenon

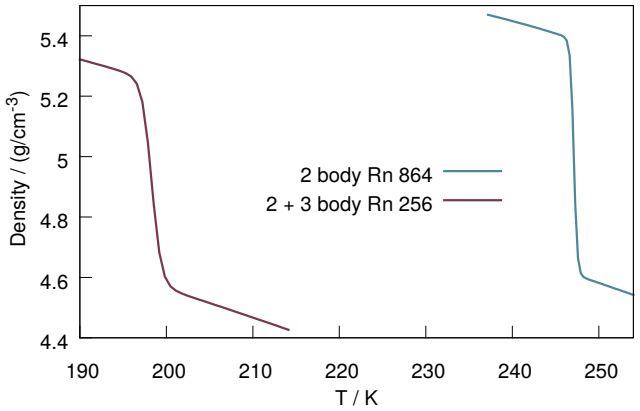

(c) Radon

Figure 11.17.: Densities for the simulated noble gases Kr, Xe and Rn. In blue the densities for the MC simulation including two-body ELJ interactions only, in red the densities obtained including two-body ELJ and three-body EAT interactions.

then the experimentally obtained values. However this can be attributed to thermal expansion at that temperature compared to the 60 K value. Indeed, the density of the liquid (2.8 g/cm^3 at 157 K) is in good agreement with experimental results. The solid density obtained using lattice summations is slightly higher, which can again be attributed to the temperature since this result corresponds to the 0 K density.

Radon Due to its high radioactivity, experimental results on the thermodynamic properties of radon are extremely rare. In 1910 Gray and Ramsay [1] estimated the liquid density to be somewhere between 4.6 and 5.7 g/cm^3. This is in agreement with the results of Herreman [196], who obtained the approximated density of 4.3 g/cm^3, and with the value of Cook, who obtained a density of 4.4 g/cm^3 at its boiling point. Grosse et al. [197] calculated the densities of radon by extrapolation of the lighter noble gases and obtained a liquid density of 4.07 g/cm^3 and a solid density (at 0 K) of 5.25 g/cm^3.

Before melting starts we obtain a density of solid radon of 5.3 g/cm^3 (191 K), which sharply decreases to 4.5 g/cm^3 (204 K) for the liquid phase. This value is similar to the approximated densities obtained by Gray, Herreman and Cook and in close correspondence with our solid state calculations. The density obtained from the lattice sums, 6.126 g/cm^3 (at 0 K), is slightly higher then the predicted density by Grosse.

Oganesson Determining the density of oganesson by experimental methods is not possible due to low production yield (one atom at a time), and an estimated density of oganesson has only been found by extrapolation from the lighter noble gases. Grosse et al. [197] estimated the density of the liquid state at the melting point to be 4.92 g/cm^3 and the density of the solid (0 K) was estimated to be 6.29 g/cm^3. His result was obtained by choosing an atomic weight of 314 g/mol.

Grosse's estimated density is similar to our 0 K density at the non-relativistic level obtained from lattice sums. The density of the liquid obtained by Grosse from extrapolation is also similar to the densities we obtain for the non-relativistic calculations. However both the solid and liquid densities do not agree with our more accurate relativistic results. The discrepancy does not come as a surprise, since a simple extrapolation does not account for the large increase in relativistic effects. This is nicely demonstrated in Fig. (11.19).

Table 11.4.: Density for the fcc crystals of 222-Rn and 294-Og at the non-relativistic (NR), the scalar relativistic (SR) and spin-orbit (SR +SO) level of theory obtained from a simple lattice summation using program SAMBA [73].

density $[g/cm^3]$	Xe	Rn SR	Rn RX2C	Og. NR	Og. SR	Og. RX2C
E2	3.938	6.221	6.312	6.256	8.156	9.348
+ ZPV-EH	3.852	6.175	6.268	6.222	8.114	9.311
+ ZPV-EAH	3.808	6.176	6.268	6.221	8.114	9.311
+ E3	3.808	6.126	6.094	5.948	7.757	8.059
+ E4	3.783	–	6.102	5.954	7.787	8.126

Table 11.5.: Densities, $\rho[g/cm^3]$, obtained from the PT MC simulations. In brackets the temperature at which the density is extracted.

		solid		liquid	
	mass $[g/mol]$	$E^{(2)}$	$+E^{(3)}$	$E^{(2)}$	$+E^{(3)}$
Kr	83.798	2.7 (123 K)	2.7 (106 K)	2.3 (126 K)	2.3 (108 K)
Xe	131.293	3.3 (175 K)	3.3 (152 K)	2.8 (178 K)	2.8 (157 K)
Rn	220.018	5.4 (245 K)	5.3 (193 K)	4.6 (248 K)	4.5 (205 K)
Og NR.	294.00	5.4 (235 K)	5.4 (218 K)	4.5 (240 K)	4.4 (223 K)
Og SR.	294.00	7.0 (326 K)	6.8 (258 K)	6.0 (333 K)	5.9 (267 K)
Og RX2C	294.00	8.0 (550 K)	7.2 (319 K)	7.0 (560 K)	6.6 (327 K)

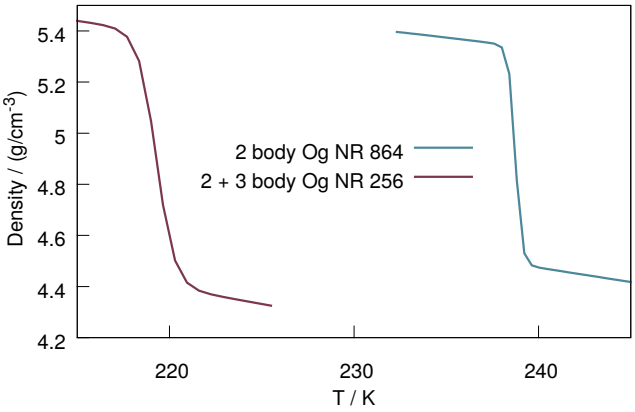

(a) Oganesson, NR

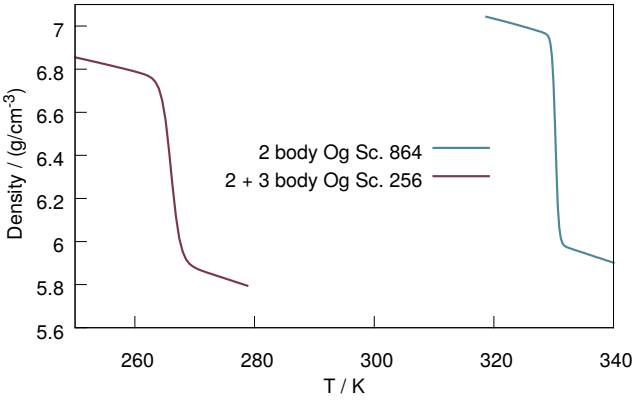

(b) Oganesson, SR

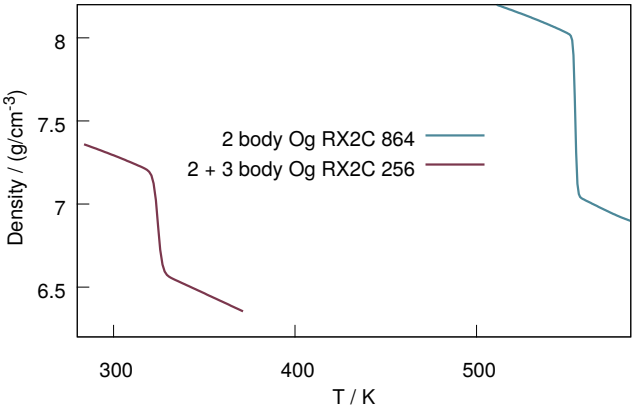

(c) Oganesson, SR + SO

Figure 11.18.: Density of the simulated noble gases. In blue the densities for MC simulation including 2-body ELJ interactions only, in red the densities obtained including 2-body ELJ and 3-body EAT interactions.

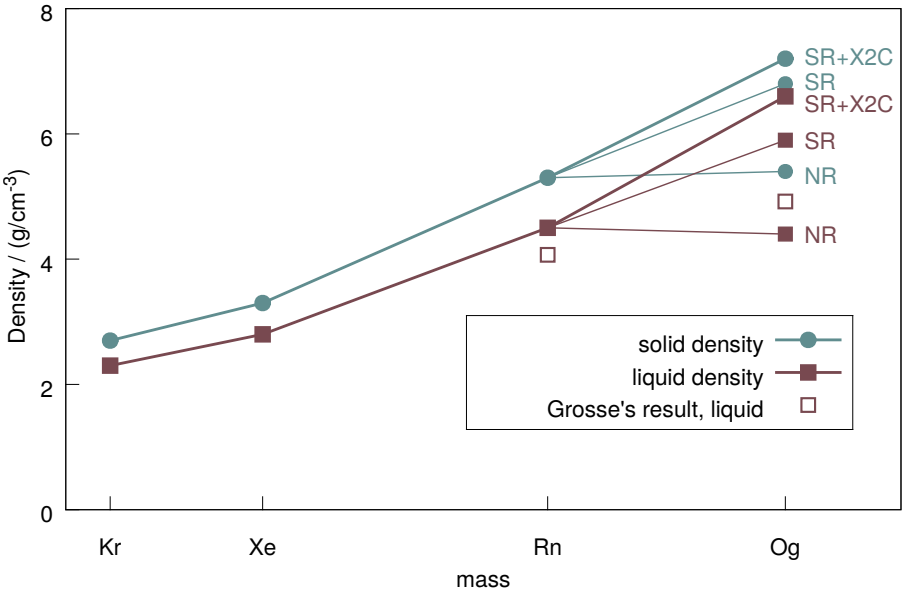

Figure 11.19.: Density as a function of mass for the solid (blue, circles) and liquid (red, squares). The filled squares and cirles denote the MC results, open squares correspond to the values obtained by extrapolation [197]

11.3. Melting Temperatures

We have finally reached the point where the obtained cluster and periodic melting temperatures can be compared with experimental data. Table 11.6 summarizes the melting temperatures for both the cluster and the periodic approach. Fig. 11.20 shows the cluster results and the known experimental melting temperatures. In the following, the melting temperatures are compared to experimental data.

Krypton The first to publish an accurate value of the triple point of krypton were Allen and Moore [198] in 1931, who reported a triple point of 116.7 $\pm$ 0.1 K. They stated that the triple point was best observed by getting the solid krypton in a apparatus 'as much as a fluffy and snow-like form as a possible' and found the melting point by waiting for it to melt as the temperature rose. Multiple similar values were later obtained, for example Keesom et al. [199] reported a triple point of 115.94 K in 1935 and Freeman and Halsey [200] reported a value of 115.6 K. Recently the triple point was confirmed by Hill [201] up to high accuracy, who obtained a triple point of 115.7755 K $\pm$ 0.3 mK.

Two-body melting temperatures are calculated to be $T^{p}_{m,2b} = 124.9$ and $T^{c}_{m,2b} = 126.9$ K for the periodic (p) and cluster (c) simulations respectively.

The lowering in melting temperature due to the three-body repulsive forces is similar for both approaches ($T^p_{m,3b} = 15.4$ K and $T^c_{m,3b} = 15.2$ K respectively). The final melting temperatures are determined to be 109.5 and 111.7 K respectively, These values of T_m are slightly lower then the experimental value of 115.78 K.

Xenon The triple point value of 133.15 K for xenon has been first obtained by Ramsay and Travers [202] in 1901, after which Allen and Moore [198] obtained the improved value of 157.65 $\pm$ 0.5 K. A melting point of 161.3 K was reported by Kane [203] in 1939 and after which the improved value was determined to be 161.40 K [2].

Two-body melting temperatures are determined to be $T^p_{m,2b} = 176.9$ K and $T^c_{m,2b} = 182.2$ K for the periodic and cluster simulations respectively. Upon inspection of the heat capacity curve of the periodic simulations one notices that the melting temperature of the 864 cell is slightly lower then the 500 cell, so the discrepancy could have evolved from statistical fluctuations of the periodic simulation. The cluster simulations lead therefore most likely to a more accurate two-body melting temperature. The lowering in melting temperature due to the three-body repulsion is for both methods fairly similar ($T^p_{m,3b} =$ - 20.8 and $T^c_{m,3b} =$ - 20.7 K). The final melting temperatures are determined to be $T^p_m = 156.1$ K and $T^c_m = 161.6$ K, of which especially the cluster result is in good agreement with the experimental value of 161.40 K.

Radon Since radon is highly radioactive and potentially poisonous, knowledge about the chemistry and physical properties of this element are scarce. Measurements of the physical properties of elemental radon are experimentally very challenging and were only done in the early years after its discovery. The melting point at $T_m = 202$ K was determined in 1909 by Ramsay and Gray [1], and is to our knowledge the only experimentally obtained value. They reported that the solid glows with great brilliancy, like a small, steel-blue arc-light. Based on the melting temperatures of the lighter noble gases, the Ramsay-Gray experiment has been questioned as early as 1925 by Paneth and Rabinowitsch, who recommended $T_m = 160$ K instead for radon [204]. However, both the cluster extrapolation as well as the periodic boundary condition simulations lead to a final melting temperature of 200 K, which is in excellent agreement with the measurement by Gray and Ramsay. Of these temperatures, $T^p_m = 247.2$ and $T^c_m = 252.2$ K as two-body melting temperature were obtained, and the three-body corrections were determined to be $\Delta T^p_m =$ - 47.5 K and $\Delta T^c_m =$ -51.9 K.

Oganesson Since oganesson is such a heavy element, relativistic effects are expected to have a large contribution to the interaction potential. Therefore

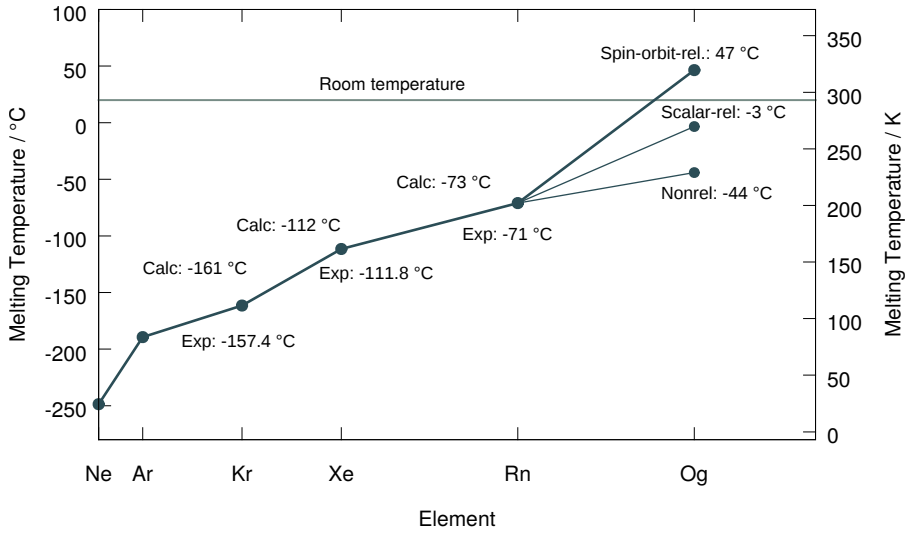

Figure 11.20.: Melting temperatures as a function of the element number. The calculated temperatures are taken from cluster simulations.

simulations were performed at three different levels of relativistic treatment (non-relativistic (NR), scalar relativistic (SR) and fully relativistic (SR+X2C)).

The **non-relativistic** results gave a melting point $T_m^p = 220.7$ K and $T_m^c = 229.1$ K, of which the three-body contribution was determined to be $T_{m,3b}^p =$ -18.2 K and $T_{m,3b}^c =$ -15.5 K respectively. Upon considering relativistic effects, the interactions between the atoms increase significantly, that is two-body interactions become more attractive whereas the three-body interactions become more repulsive. Indeed, the **scalar-relativistic** results show approximately a 100 K increase in the two-body melting temperature, and also the three-body contributions increase significantly, i.e. $T_{m,3b}^p =$-62.0 K and $T_{m,3b}^c =$-63.0 K. This leads to the final melting temperatures of $T_m^p = 268.3$ and $T_m^c = 269.8$ K. The **spin-orbit** corrected potentials gave an even larger increase in interaction strength, which results in the surprisingly high melting temperatures of $T_{m,2b}^p = 554.4$ K and $T_{m,2b}^c = 544.4$ K. However these values are greatly reduced by the three-body repulsion which is $T_{m,3b}^p =$ -230.5 and $T_{m,3b}^c =$ -224.8 K respectively. This leads to the final melting temperature of $T_m^p = 324.0$ K and $T_m^c = 319.7$ K (50.9^{o}C, 46.6^{o}C) and with room temperature being around 20^{o}C, it implies that oganesson is a solid (!). This value is much larger than reference value obtained by Grosse who estimated the melting temperature to be $T_m = 256$K [197].

Table 11.6.: Periodic and cluster final melting temperatures. For oganesson simulations were performed for the three different levels of relativistic treatment (Non relativistic (NR), scalar relativistic (SR) and fully relativistic (SR+X2C))

		Periodic	Cluster	**Exp.**
Krypton				
	2b	124.9	126.85	
	$\Delta_{(2b-3b)}$	15.4	15.16	
	T_m	109.5	111.69	**115.78**
Xenon				
	2b	176.85	182.24	
	$\Delta_{(2b-3b)}$	20.78	20.66	
	T_m	156.07	161.58	**161.40**
Radon				
	2b	247.18	252.16	
	$\Delta_{(2b-3b)}$	47.46	51.87	
	T_m	199.72	200.30	**202**
Og NR				
	2b	238.83	244.65	
	$\Delta_{(2b-3b)}$	18.18	15.51	
	T_m	220.65	229.14	-
Og SR.				
	2b	330.35	332.83	
	$\Delta_{(2b-3b)}$	62.01	63.04	
	T_m	268.34	269.79	-
Og RX2C				
	2b	554.44	544.4	
	$\Delta_{(2b-3b)}$	230.46	224.75	
	T_m	323.98	319.65	-

11.3.1. Errors

There are multiple sources for errors involved in calculating melting temperatures. They come from (i) the choice of the interaction potentials, (ii) the algorithm for the melting simulation used, (iii) the extrapolation to the bulk temperature for finite clusters, (iv) for a cell with periodic boundary conditions the number of particles used in the cell and the estimate of the superheating correction factor, and (v) the neglect of quantum / vibrational effects (which should however be small for the heavy rare gas systems studied here).

The close correspondence between cluster and periodic results implies that we can confide on the Monte Carlo method. Even though in a present paper by Pahl et al. [10] an accuracy of the melting temperature of almost a few Kelvins was achieved, it is by no way trivial to achieve a similar accuracy for the heavier rare gases as large relativistic and correlation effects require higher order terms in the many body expansion. The greatest source of error would thus be due to the truncation in the many-body interaction, especially for oganesson. The four-body forces are of attractive type and therefore the given melting temperatures should be interpreted as a lower bound to the melting temperature reported here.

12. Lennard-Jones Melting

In this chapter, melting results of the 6-12 LJ potential in reduced units ($\varepsilon = 1$ K and $r_e = 1$ Å) are presented. The extrapolated result obtained from the cluster MC simulations and the superheated melting temperatures obtained from the periodic MC simulation will guide as a reference value for the analytical calculations (see Chapter 13), and will enable us to obtain insight on the superheating mechanism (Chapter 14).

12.1. Literature Results

The popularity of numerical simulations utilizing the 6-12 LJ potential can be attributed to the numerical efficiency of the potential. The phase diagram and the triple point value of the 6-12 LJ potential have therefore extensively been studied over the past decades. In chronological order, triple point values were obtained by Hansen and Verlet [205] (0.68 K) using a Monte Carlo algorithm in free energy calculations; by Ladd and Woodcock [206] (0.67 K) using molecular dynamics simulations; by Agrawal and Kofke [207](0.687 K) using Gibbs-Duhem integration; by Barroso and Ferreira [208] (0.692 K) using Helmholtz free energy calculations; by Ahmed and Sadus [209] (0.661 K) using molecular dynamics simulations; and by Kataoka and Yamada [210] (0.683 K) who obtained the triple point value by carrying out molecular dynamics simulations using the interface pinning method. For consistency, it is useful to compare these results with the results obtained from the PTMC simulation method used in this thesis.

12.2. Monte Carlo Melting Results

The periodic and cluster simulations are conducted according to the same numerical procedure and specifications as implemented here for the more realistic many-body potentials of the noble gases. Heat capacities and extrapolated cluster melting temperature is depicted in Fig. 12.2. Melting temperatures, which correspond to the temperature where the heat capacity curve shows a maximum, for the periodic NPT simulations are listed in table 12.2 and the melting temperatures of the clusters are listed in table 12.1.

Regarding the cluster simulations, the LJ melting temperatures T_m^N of the two smallest clusters ($T_m^{13} = 0.284$ and $T_m^{55} = 0.295$) are very similar to the values ($T_m^{13} = 0.29$ and $T_m^{55} = 0.31$) obtained by Berry and Smirnov [211]

and the extrapolated melting temperature of 0.676 K is in excellent agreement with the reported values of the triple point. Regarding the periodic simulations, by inspection of the energy contribution as a function of the two-body cutoff distance it can be concluded that the melting temperature for the $N = 864$ cell is converged. However, the melting temperature of the $N = 864$ cell overestimates the bulk melting temperature by a factor of $0.832/0.676 = 1.230$. This is in agreement with the $\ln 2/3 + 1 = 1.231$ superheating correction factor used throughout this thesis.

Table 12.1.: Melting temperatures of the N atomic LJ clusters and extrapolated melting temperature $T_m(\infty)$ (in reduced units).

N	13	55	147	309	561	923	1415	$T_m(\infty)$
T_m	0.284	0.295	0.374	0.428	0.486	0.504	0.535	0.676

Table 12.2.: Melting temperatures of the LJ periodic cells, not corrected for superheating (in reduced units).

N	32	108	256	500	864
T_m	0.806	0.806	0.809	0.822	0.832

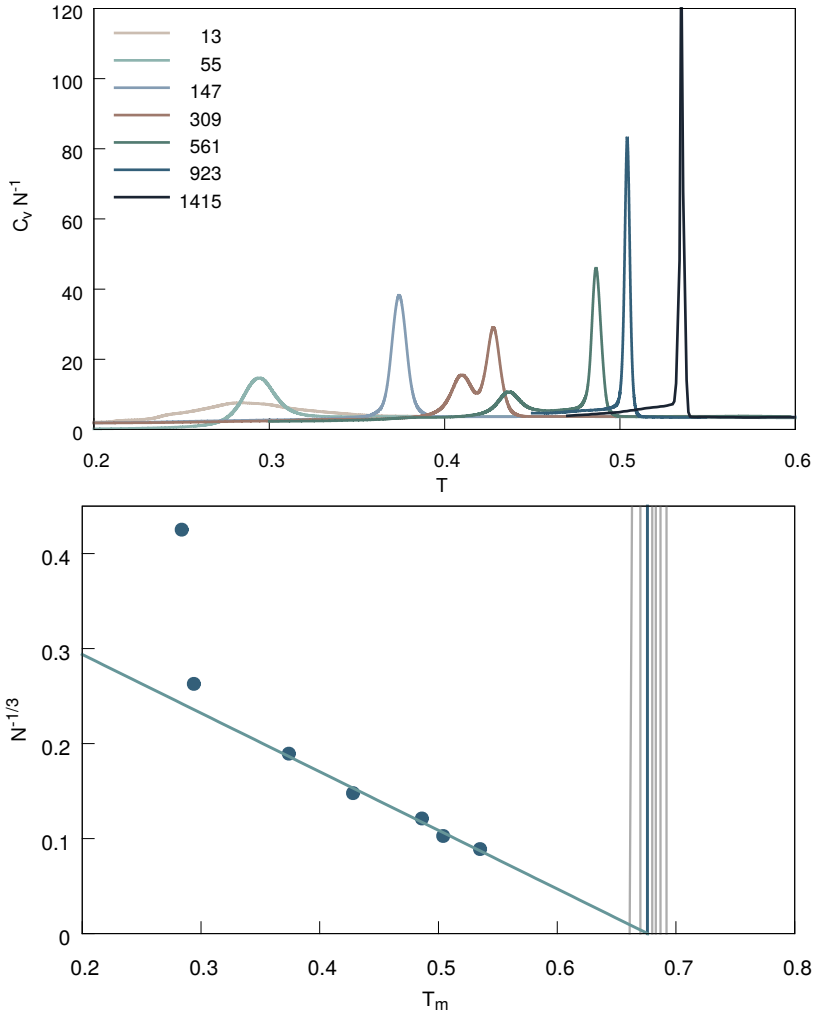

Figure 12.1.: (Top) Heat capacities per atom for the Mackay Icosahedral clusters containing up to 1415 atoms.
(Bottom) Cluster melting temperatures extrapolated to the bulk melting temperature. Grey lines show the literature values of the melting temperatures as listed in the text.

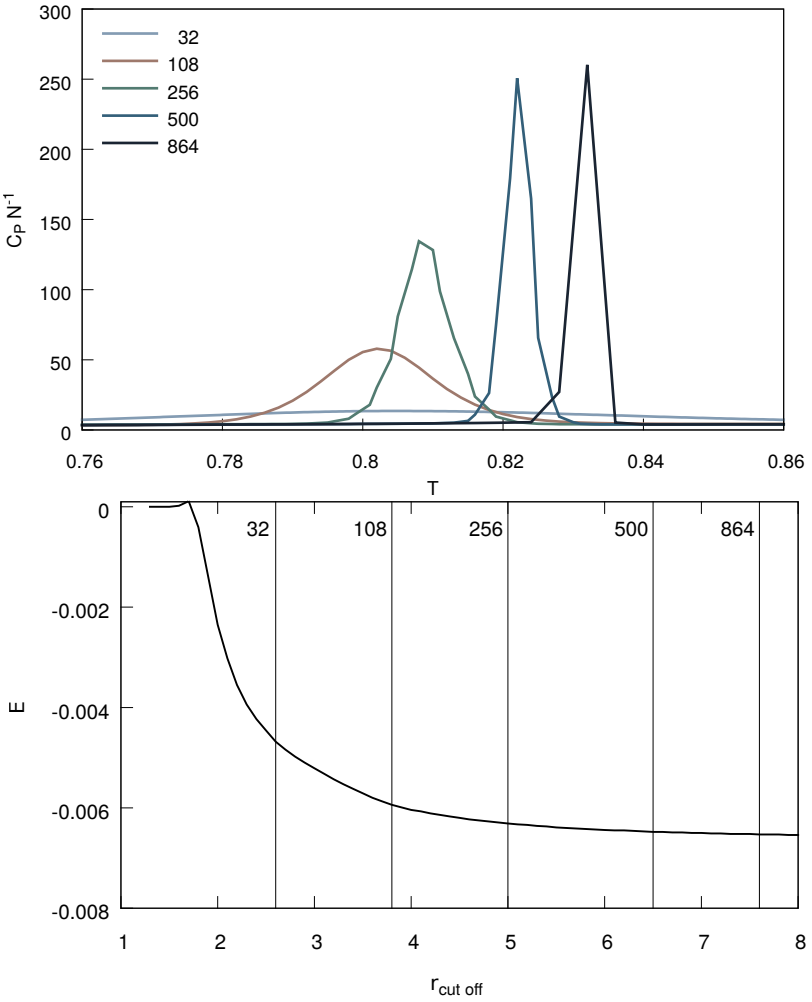

Figure 12.2.: (Top) Heat capacities per atom for the NPT periodic LJ cells. (Bottom) The total two-body contribution as a function of the cut-off radius. Vertical lines correspond to the cut-off distances for the different simulation cells.

Part V.

Beyond Simulations

13. Analytical Findings

The content of this chapter result from the general observation that there is a well known approximate linear correlation between the cohesive energy and the melting temperature for the elements in the periodic table including the metals and the noble gases, as is demonstrated in Fig. 13.1. This relationship is purely empirical and not well understood. More specifically, whereas the metals show some irregular behavior, the noble gases all lie nicely on a sraight line. Besides, the possibility of obtaining an approximate melting temperature of the heavy noble gases by extrapolation, this correlation also hints that there is simple underlying analytical relationship between the interaction potential and the melting temperature. Such a relation would not only be an important contribution to the prediction of melting temperatures, but will shed perhaps some light on the mechanism that causes melting. In this chapter we show for the first time that it is indeed possible to formulate a simple analytical equation and at the same time demonstrate how the melting mechanism correlates to superheating. In section 13.2 the scaling relation between the cohesive energy and the melting temperature is studied from the ad-hoc assumption that $E^{\mathrm{coh}}/T_m =$ constant. In section 13.3 an analytical expression for the melting temperature as a function of the two-body fitting coefficients is formulated.

13.1. Relations for the Bulk

Here the analytical relation for the cohesive energy and bulk modulus for certain lattices in terms of the ELJ fitting parameters is given.

13.1.1. Relation between dimer potential and cohesive energy

An analytical form for the cohesive energy as a function of nearest neighbour lattice distance r_s has originally been formulated by Lennard-Jones and co-workers [213] and later extended to a more general expression by Schwerdtfeger et al. [73]

$$E^{\mathrm{coh}}_{\mathrm{ELJ}}(r_s) = \frac{1}{2}\sum_{n>3} C_n L_n r_s^{-n} \tag{13.1}$$

where C_n are the Extended Lennard-Jones fitting parameters and L_n are the (Lennard-Jones-Ingham) lattice sums. For physical reasons $n \geq 6$ is usually

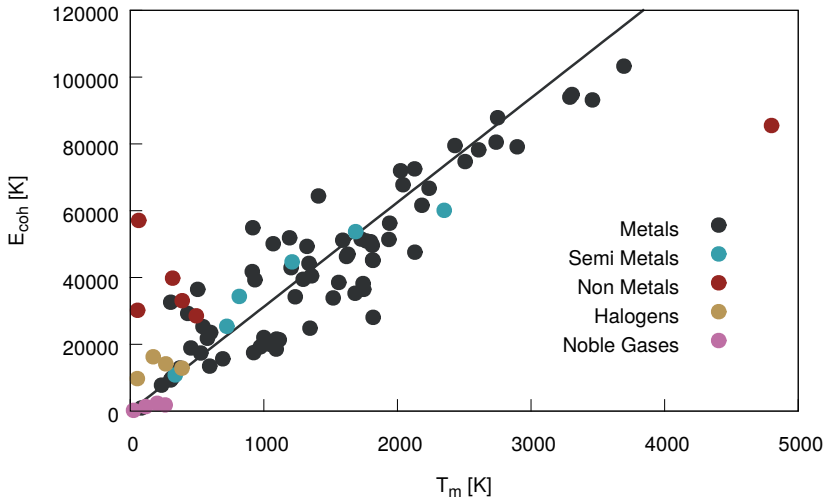

Figure 13.1.: The correlation between meting temperature and cohesive energy for all known elemental solids. The line is the scaling relation derived by Guinea [212] for pure metals.

chosen. The lattice sums have been evaluated to computer precision by the Auckland group for the cubic lattices and for the hexagonal closed packed structure [73]. For the simple Lennard-Jones 6-12 potential,

$$V_{\mathrm{LJ}}(r) = \varepsilon\left[\left(\frac{r_{de}}{r}\right)^{12} - 2\left(\frac{r_{de}}{r}\right)^{6}\right] \tag{13.2}$$

the expression for the cohesive energy simplifies to

$$E_{\mathrm{LJ}}^{(2)}(r_s) = \varepsilon\left[\frac{1}{2}L_{12}\left(\frac{r_{de}}{r_s}\right)^{12} - L_6\left(\frac{r_{de}}{r_s}\right)^{6}\right] \tag{13.3}$$

where ε is the minimum and r_{de} the dimer equilibrium distance of the 6-12 Lennard-Jones potential. From minimization of the cohesive energy with respect to the solid-state distance r_s we obtain the solid state equilibrium distance r_{se}

$$r_{se} = \left(\frac{L_{12}}{L_6}\right)^{1/6} r_{de} \tag{13.4}$$

Combining Eq. (13.3) and Eq. (13.4) gives the minimim value of the 6-12 LJ cohesive energy E_{min}^{LJ}

$$E_{min}^{\mathrm{LJ}} = \frac{1}{2}\frac{\varepsilon L_6^2}{L_{12}} \tag{13.5}$$

13.1.2. Bulk Modulus

The bulk modulus can also be expressed in terms of the ELJ fitting parameters and Ingham coefficients

$$B_{\mathrm{ELJ}}(r_s) = \frac{1}{18V}\sum_{n>3} n(n+3)c_n L_n r_s^{-n} \tag{13.6}$$

Here f_s is a lattice-specific parameter converting the nearest neighbour distance r_s into the volume V, i.e. $f_{sc} = 1$, $f_{bcc} = 1/(3/\sqrt{2})$, $f_{fcc} = 1/\sqrt{2}$ and $f_{hcp} = 1/\sqrt{2}$. For the fcc and hcp lattice this takes the form

$$B_{\mathrm{ELJ}}(r_s) = \frac{\sqrt{2}}{18r_s^3}\sum_{n>3} n(n+3)c_n L_n r_s^{-n} \tag{13.7}$$

and the simple relation for the fcc and hcp Lennard-Jones bulk modulus is

$$B_{\mathrm{LJ}} = L_{12}\left(\frac{2L_6}{L_{12}}\right)^{5/2}\frac{\varepsilon}{r_{de}^3} \tag{13.8}$$

13.2. Scaling Relation Between the Cohesive Energy and Melting Temperature

In the following the scaling of the melting temperature as a function of the cohesive energy for fcc structures is studied. In section 13.2.1 the expected scaling for Lennard-Jones-like potentials is derived, which will be compared to the scaling relation of the noble gases in section 13.2.2.

13.2.1. Lennard-Jones Scaling

Solids described by the Lennard-Jones interaction, but with a different interaction strength, E_{min}, are expected to satisfy the relation

$$\frac{E_{min}^{\mathrm{LJ}}}{T_m} = const. \tag{13.9}$$

The melting temperature of the Lennard-Jones potential in reduced units ($\varepsilon = 1$, $r_{de} = 1$) is determined to be $T_m = 0.681$ (see section 12.2) such that

$$\frac{\varepsilon}{T_m} = \frac{1}{0.681} \tag{13.10}$$

Combining Eq. (13.5) and Eq. (13.10) the relation between the cohesive energy, E_{min}^{LJ}, and melting temperature, T_m, is therefore expected to be

$$\frac{E_{min}^{\mathrm{LJ}}}{T_m} = \frac{L_6^2}{2L_{12}}\frac{1}{0.681} \cong 12.64 \tag{13.11}$$

13.2.2. Extended Lennard Jones Scaling

Similarly as for the LJ potential, a scaling relation can be formulated for the melting temperatures obtained with the ELJ potential. In this case the scaling relation follows from the average value of $E_{min}^{\mathrm{ELJ}}/T_m^{2b}$, where E_{min}^{ELJ} is calculated according to Eq. (13.1) and two body melting temperatures are obtained from our extrapolated Monte Carlo cluster simulations. We find for the scaling relation

$$\frac{E_{min}^{\mathrm{ELJ}}}{T_m^{2b}} \cong 12.14 \tag{13.12}$$

which is close to the ideal LJ value (Eq. (13.11)). The two-body ELJ potential curves are depicted in Fig 13.3 (Bottom) and the similarity with the Lennard-Jones potential becomes apparent when the potentials are plotted in reduced units as shown in Fig. 13.3 (Center). One can clearly see that the two-body noble gas potentials in reduced units are all of very similar shape and, in comparison to the Lennard-Jones potential, are only slightly less binding in the dispersive region. The similarity in the scaling relation for the LJ potential and the noble gas ELJ potentials is therefore not surprising. Small deviations in the ratios of the noble gases are not surprising, since the potentials (in reduced units) show slight variations in the dispersive region as demonstrated in Fig. 13.3 (Bottom).

Of course, when the many-body expansion in terms of the interaction energy breaks down as in the case of metals, this simple relation holds to a lesser degree. A deviation of the linear relation is already expected for the heavier noble gases when three-body contributions to the potential become more pronounced: the three-body repulsion causes the on-site potential to be less binding. As a result the cohesive energy and T_m are reduced and the ratio is altered. The element that is most deviating from the ideal LJ result is oganesson simulated at the two+three-body RX2C level of theory. For the lighter elements, however, the three-body contributions are very small and therefore also the ratios $E_{min}^{\mathrm{ELJ}}/T_m$ for the two+three body MC results as well as the ratios for the experimental results are in good agreement with Eq. (13.12). (NB: for helium the experimental value has to be taken with care as solid helium only exists under pressure and vibrational effects become dominant.)

While the E_{min}/T_m ratios discussed so far are empirical, we require a deeper understanding of the relation between the potential energy curve and the melting temperature. The analytical expressions determined in the next section will give us deeper insights into the origin of this simple relation.

Table 13.1.: Cohesive energies, E_{min}, and melting temperatures, T_m, for the nobles gases. Non-relativistic (NR), scalar relativistic (SR) and fully relativistic with spin-orbit included (SO) two-body LJ and ELJ cohesive energies are obtained from Eq. (13.1) which gives the cohesive energy for the (Extended) Lennard Jones potentials. The two+three-body cohesive energies are obtained from solid state calculations performed with SAMBA [73].

		$E_{min}^{\mathrm{LJ}}\ [K]$	$E_{min}\ [K]$	$T_m\ [K]$	E_{min}/T_m
Ne	2B	354.55	326.20	26.9	12.13
Ar	2B	1201.29	1095.72	90.6	12.09
Kr	2B	1729.57	1521.05	126.85	11.99
Xe	2B	2431.81	2161.25	182.24	11.86
Rn	2B	3297.83	3052.07	253.32	12.05
Og NR	2B	3270.73	2904.27	244.65	11.87
Og SR	2B	4537.90	4095.90	332.83	12.31
Og SO	2B	7758.48	7099.04	554.4	12.80
Xe	2+3B		1995.27	161.58	12.35
Rn	2+3B		2613.96	201.64	12.96
Og NR	2+3B		2643.89	229.14	11.54
Og SR	2+3B		3500.57	269.79	12.98
Og SO	2+3B		5170.03	319.65	16.17
Ne	EXP		232.51	24.56	9.47
Ar	EXP		928.74	83.85	11.08
Kr	EXP		1422.53	115.79	12.29
Xe	EXP		1898.34	161.35	11.76

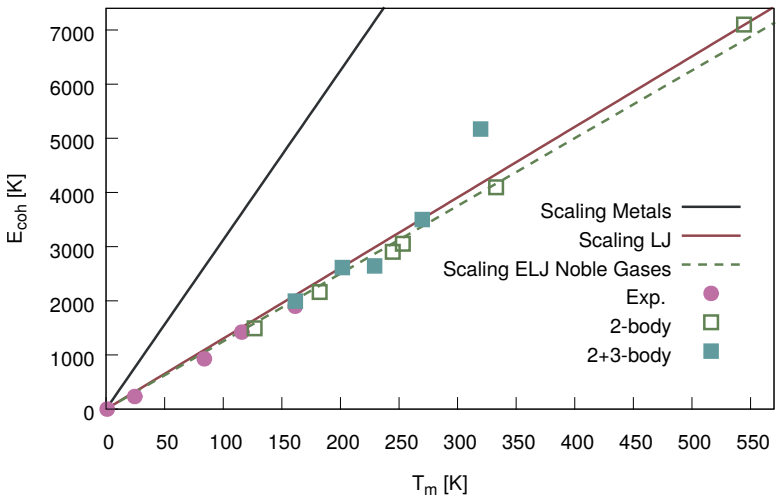

Figure 13.2.: Melting temperature versus cohesive energy for the rare gases. The dotted green line corresponds to the expected linear relation for Lennard Jones type potentials according to Eq. (13.11). The solid red line corresponds to the linear relation between the two-body MC melting temperatures and ELJ cohesive energies. For comparison, the solid black line is the scaling relation for pure metals as derived by Guinea [212].

13.3. Analytical Relation

In the previous section the scaling relation between the melting temperature and cohesive energy was given for the ad-hoc assumption that $E_{min}/T_m = const.$ where the scaling constant was determined by a linear fit to the MC melting temperature versus the analytically obtained cohesive energy. We will now show that the two-body melting temperature can also be calculated analytically.

13.3.1. Melting at the Inflection Point

Melting occurs when the root-mean-square amplitude of thermal vibrations of atoms reaches a critical fraction of the nearest-neighbour separation. Lindemann [122] determined the critical fraction to be roughly 10 percent. However, this estimate was based on experimental findings rather than from a mathematical perspective. In this section it will be demonstrated that the critical interatomic distance lies at the inflection point of the cohesive energy potential curve $E_{coh}(r_s)$.

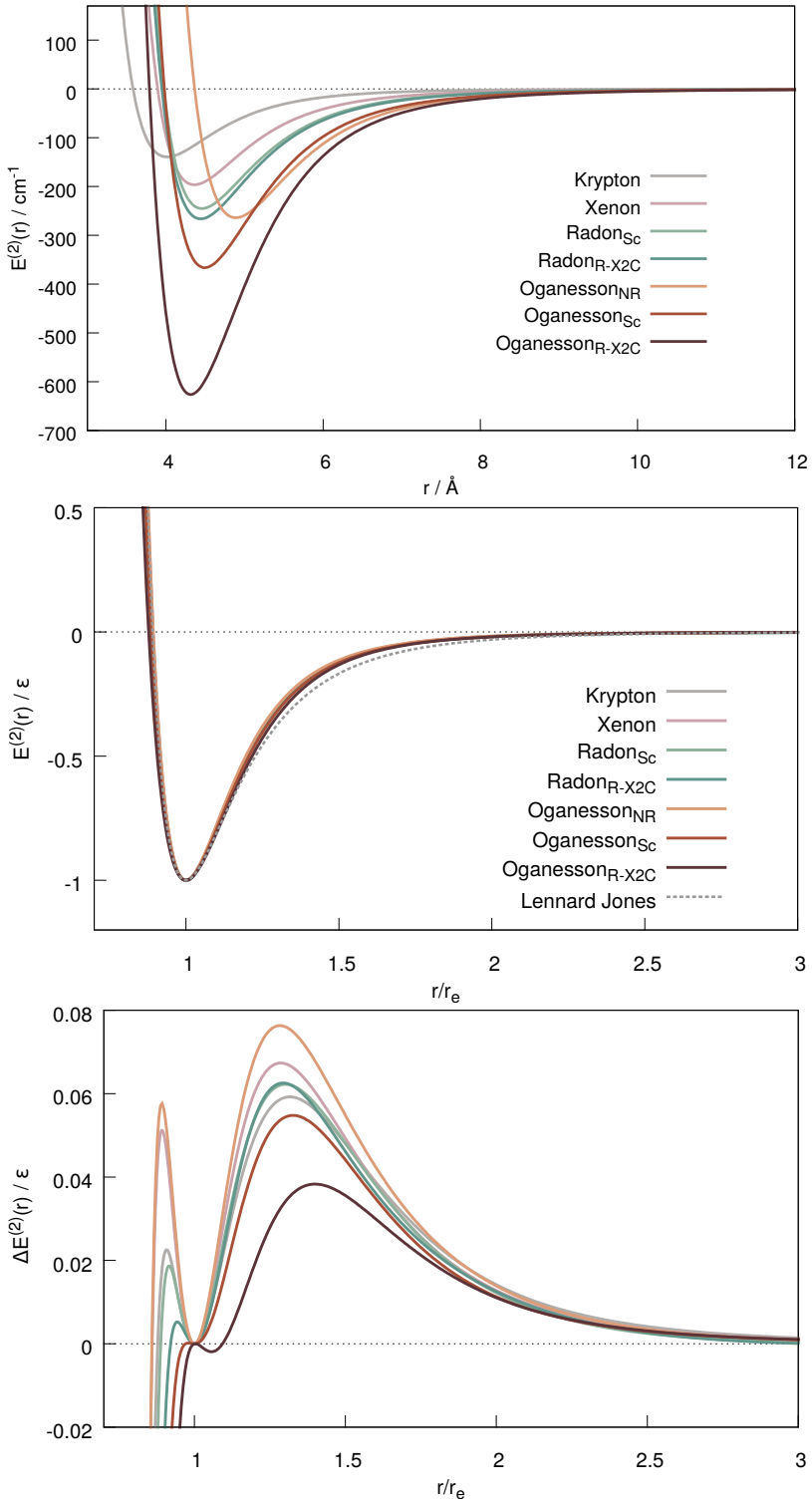

Figure 13.3.: (Top) Two-body ELJ potential energy curves. (Center) Scaled two-body ELJ potential energy curves. (Bottom) Difference between the LJ potential and the scaeld ELJ potentials.

Inflection Point

The inflection point, r_{si}, of the solid state cohesive energy, $E_{coh}(r_s)$ is obtained by solving

$$\frac{d^2 E_{coh}(r_s)}{dr_s^2} = 0 \tag{13.13}$$

For the Lennard-Jones potential, Eq.(13.2), with cohesive energy as given in Eq (13.3), the second-order derivative of the cohesive energy equals to

$$\frac{d^2 E_{coh}^{(2)}}{dr_s^2} = \varepsilon \left[42 L_6 \frac{r_{de}^6}{r_s^8} - 78 L_{12} \frac{r_{de}^{12}}{r_s^{14}} \right] \tag{13.14}$$

and therefore the LJ inflection point, r_{si}, is situated at

$$r_{si} = \left(\frac{13}{7} \right)^{1/6} \left(\frac{L_{12}}{L_6} \right)^{1/6} r_{de} \tag{13.15}$$

Fig. 13.4 demonstrates the location of the inflection point for the LJ potential and the corresponding root-mean-square amplitude of vibration.

Breaking of Symmetry at Inflection Point

Since the first derivative of the energy corresponds to the force, the second derivative corresponds to the change in force strength. As at the inflection point the second derivative is zero, it implies from a classical point of view that beyond the inflection point the restoring forces decrease with increasing deviations from equilibrium. As a result the on-site cohesive energy forms a double well causing the atoms to move away from the equilibrium distance and consequently the symmetry of the bulk system is broken. For example, a simple one-dimensional system of three atoms, for which the interaction is described by the LJ potential, the onsite potential of atom j, due to its interaction with the two neighboring atoms $j-1$ and $j+1$ will develop an increasingly flat-bottomed well as the distance between those two outside atoms increases. When the distance between atom $j-1$ and $j+1$ exceeds $2r_{si}$, the on-site potential will develop a double well. This is demonstrated in Fig. 13.6, the top figure corresponds to the on-site potential of the center atom and the bottom figure demonstrates the corresponding force. This nicely fits the observation of Cotterill [214] who has shown that for simple models the fluctuations beyond the inflection point lead to the formation and growth of defects.

Melting at the Inflection Point

In the previous section it was argued that once the solid-state distance exceeds the distance of the inflection point, the symmetry of the on-site potential is

broken. It will now be demonstrated that upon thermal expansion to the inflection point the solid-liquid phase transition occurs.

The following results are deducted from the MC melting simulations with periodic boundary conditions. It is however important to remember that the solid/liquid phase transition for the periodic systems modeled using MC simulations in the NPT ensemble occurred at the superheated temperature instead of the real melting temperature. This will be further discussed in section 14.

The volume as a function of temperature is obtained from the periodic NPT MC simulations, from which we can deduct the nearest neighbor distance as a function of temperature

$$V = (a_{lat} n_{cells})^3 \tag{13.16}$$

where $a_{lat} = \sqrt{2} r_s$ is the unit cell edge length for fcc cells and the number of atoms in the simulation cell correspond to $N = 4n_{cells}^3$. Fig 13.5 demonstrates the increase in nearest neighbor distance as a function of temperature around the solid liquid phase transition for the simulations with the LJ potential in reduced units. The horizontal dotted line corresponds to r_{si}, the vertical dotted lines correspond to the solid-liquid transition temperature of the different cell sizes. The intersection of the superheated temperature, T_{SH}, with the solid state distance, $r_s(T)$, is indeed very close to the distance where the solid state distance corresponds to the distance at the inflection point, $r_s(T) = r_{si}$. Hence it is demonstrated that the solid/ liquid phase transition occurs when $r_s(T) = r_{si}$, in other words, the classical picture of symmetry breaking at the inflection point is a good approximation to the more accurate quantum picture.

13.3.2. Analytical Melting Temperature

Analytical Relation

The solid melts when (approximately) the root-mean-square displacement (RMSD) of each atom from its equilibrium position, $\langle u^2 \rangle^{1/2}$, equals to l, the length of the vibrational amplitude at the inflection point,

$$l = \langle u^2 \rangle^{1/2} \tag{13.17}$$

From the Debye model at high temperatures, the RMSD can be expressed in terms of temperature T, atomic mass M, and Debye temperature Θ_D [215]

$$\langle u^2 \rangle^{1/2} = \left(\frac{9\hbar T}{M k_B \Theta_D^2} \right)^{1/2} \tag{13.18}$$

In order to derive this equation the potential energy of the crystal is expanded as a Taylor series in the lattice displacements. Due to its complicity, the series

is curtailed at the second-order term. Higher order terms, corresponding to anharmonic terms, are disregarded. Reformulated in terms of temperature T, bulk modulus B and solid state equilibrium distance r_{se}, Eq. (13.18) reads

$$\langle u^2 \rangle^{1/2} = \left(\frac{0.827 k_B T}{r_{se} B} \right)^{1/2} \tag{13.19}$$

This result was introduced by Guinea et al. [212] who used this relation to obtain the scaling relation for the metals

$$T_m = 0.032 E_{coh}/k_B \tag{13.20}$$

where T_M is the melting temperature of pure metals and E_{coh} the cohesive energy and k_B the Boltzmann's constant. The solid line in Fig. 13.1 corresponds to this scaling relation. The scaling factor is in close agreement with the empirical relation obtained by a linear fit to the experimentally obtained datapoint of $T_m = 0.035 E_{coh}/k_B$. This prediction was made possible by the discovery of universality in binding energy relations for metals [212, 216, 217]. However B and r_{se} were taken from experiment and also l was derived from experimental numbers. In this thesis we follow a somewhat different approach since we do not need to use experimental values for the bulk modulus and the solid-state equilibrium distance, nor an approximate value for the vibrational amplitude at the inflection point. Instead l, r_{se} and B are expressed in terms of the ELJ fitting coefficients, making it possible to obtain the temperature at which the solids melts, the superheated melting temperature T_{SH} (as entropy effects are not included here, see below), solely from the ab-initio interaction potential [212],

$$k_B T_{SH} = \frac{l r_{se} B}{0.827} \tag{13.21}$$

In the following section this relation will be applied for LJ potentials after which the two-body ELJ melting temperatures are calculated.

Analytical Lennard-Jones Result

Eq. (13.19) in combination with the expression for the LJ bulk modules, Eq. (13.8), gives a relation between the cohesive energy and superheated temperature for Lennard-Jones type potentials.

$$l = \left(\frac{0.827 k_B T_{SH} r_{de}^2}{\varepsilon L_{12}} \left(\frac{L_6}{L_{12}} \right)^{1/6} \left(\frac{L_{12}}{2L_6} \right)^{5/2} \right) \tag{13.22}$$

As a first approximation, assuming the potential to be harmonic, l is the distance from the solid state equilibrium distance to the inflection point of the

cohesive energe curve, $l \cong r_{si} - r_{se}$. Using Eq. (13.4) and Eq. (13.15), l equals for the fcc lattice

$$\begin{aligned} l &= \left[\left(\frac{13}{7}\right)^{1/6} - 1\right]\left(\frac{L_{12}}{L_6}\right)^{1/6} r_{de} \\ &\cong 0.1056 r_{de} \end{aligned} \tag{13.23}$$

Combining Eq (13.23) and Eq. (13.22) gives

$$k_B T_{SH} = 1.39\varepsilon \tag{13.24}$$

This does not correspond to the superheated melting temperature obtained from the periodic NPT simulations ($T_{SH} = 0.832$) as discussed in section 12. An improved relation is obtained if we compute l for an anharmonic potential instead. In this case l is given by

$$l = \frac{1}{2}(r_{si} - r_{si_2}) \tag{13.25}$$

where r_{si_2} is the opposite location in the repulsive region of the cohesive energy curve corresponding to

$$E_{coh}[r_{si_2}] = E_{coh}[r_{si}] = \frac{13}{7}\left(\frac{L_{12}}{L_6}\right)^{1/6} r_{de} \tag{13.26}$$

solving for r_{si_2} gives

$$r_{si_2} = \left(\frac{13}{9}\right)^{1/6}\left(\frac{L_{12}}{L_6}\right)^{1/6} r_{de} \tag{13.27}$$

such that the length l in the anharmonic approach equals to

$$l = (r_{si} - r_{si_2})/2 = \left(\left(\frac{13}{7}\right)^{1/6} - \left(\frac{13}{9}\right)^{1/6}\right)\left(\frac{L_{12}}{L_6}\right)^{1/6} r_{de} \tag{13.28}$$

By combining Eq. (13.22) and Eq. (13.28) the relation reads for the fcc lattice

$$k_B T_{SH} = 0.851\varepsilon \tag{13.29}$$

As expected the analytical relation results in a temperature that is not equal to the cluster extrapolated melting point, but equals the superheated temperature, as obtained by periodic NPT simulations, instead. Indeed when corrected for superheating the melting temperature corresponds to $T_m = 0.851/(\frac{\ln 2}{3} + 1) = 0.691K$. This is in close agreement with the melting temperature obtained from cluster NVT simulations ($T_m = 0.681$) as well as literature values for the melting temperature of the LJ potential. It also

means that the analytically derived linear correlation between melting temperature and cohesive energy needs to be corrected for superheating. Starting from

$$\frac{\varepsilon}{k_B T_m} = \frac{1}{0.851} \tag{13.30}$$

in combination with $E_{coh}^{LJ} = \frac{1}{2}\frac{\varepsilon L_6^2}{L_{12}}$ and corrected for superheating $T_m = T_{SH}/(\frac{\ln 2}{3} + 1)$ one obtains

$$\frac{E_{coh}^{LJ}}{T_m} = \frac{L_6^2}{2L_{12}} \frac{1}{0.851} \left(\frac{\ln 2}{3} + 1 \right) \cong 12.45 \tag{13.31}$$

for the fcc lattice. The discrepancy between Eqs. (13.11) and (13.31) is not very large, and most likely originates from the approximation in the expression for $\langle u^2 \rangle$ assuming an harmonic potential.

Analytical Melting Temperatures of the Noble Gases

Finally, the two-body melting temperature of the noble gases are computed from the simple relation

$$k_B T_{SH} = \frac{l^2 r_{se} B}{0.827} \tag{13.32}$$

with B computed according to Eq. (13.7), r_{se} by minimizing the cohesive energy, Eq. (13.1), with respect to the solid-state distance and l, the length of the vibrational amplitude at the inflection point. Again, the solid-liquid phase transition temperature needs to be corrected for superheating

$$T_m = \frac{T_{SH}}{(\frac{\ln 2}{3} + 1)} \tag{13.33}$$

Table 13.2 lists the superheated melting temperatures using for l the harmonic and anharmonic lengths, $l_H = r_{si} - r_{se}$ and $l_A = \frac{1}{2}(r_{si} - r_{si_2})$ respectively, as well as the corrected value T_m^A. The for superheated corrected two-body NPT melting temperature $T_{MC}^{2b,NPT}$ is listed for comparison. See also Fig 13.7.

For the elements neon and argon we obtain a good agreement with the melting temperatures obtained from Monte Carlo simulations. However the relation worsens for the heavy noble gases as the analytical relation overestimates the temperature by approximately 5 to 15 percent. Again, this discrepancy can be attributed to the approximation made in the derivation of the analytical expression for the RMSD, but perhaps also points towards limitations of such a simple classical model as each element melts at a distance slightly before (increasing for the heavier ones) the inflection point where the potential energy surface of the solid becomes very flat.

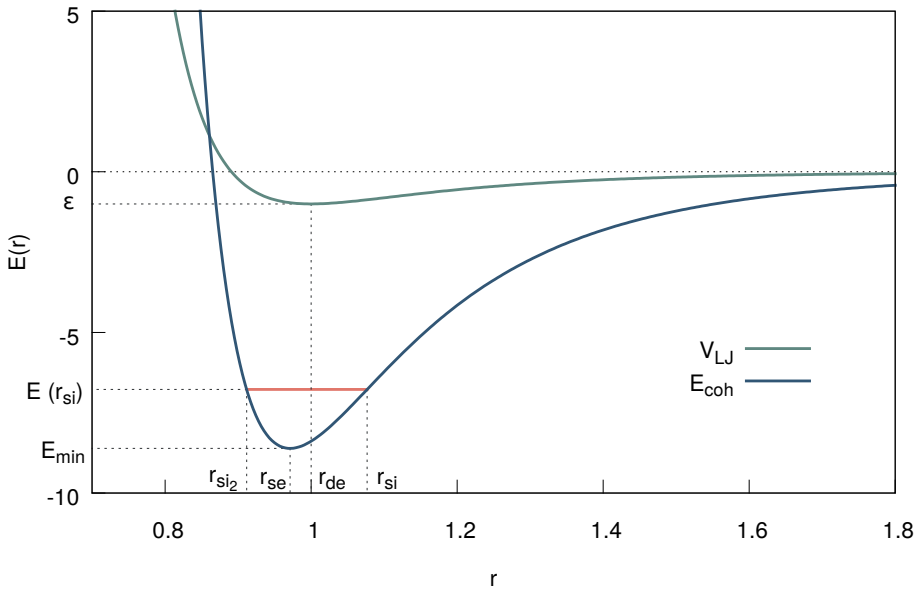

Figure 13.4.: Dimer and solid-state Lennard-Jones energy curves. r_{de} dimer equilibrium distance, r_{se} solid state equilibrium distance and r_{si} solid state inflection point. Red line indicates the root-mean-square amplitude of vibration at the inflection point.

Table 13.2.: Amplitude of vibration at the inflection point, l, assuming harmonic potential l_H and anharmonic potential l_A (in Å). Analytically calculated melting temperatures T_m^H and T_m^A (in K). Corrected for superheating T_{corr}^A, compared to the two-body Monte Carlo results T_{MC}^{2b}.

	l_H	l_A	T_{SH}^H	T_{SH}^A	T_m^A	$T_{MC}^{2b,NPT}$
He	0.64	0.51	13.9	8.62	7.00	4.22
Ne	0.61	0.48	54.3	33.9	27.5	26.9
Ar	0.75	0.59	184.1	115.3	93.6	90.6
Kr	0.80	0.64	258.8	161.9	131.5	124.9
Xe	0.86	0.68	363.3	229.0	186.0	176.6
Rn	0.91	0.72	517.0	327.2	265.8	247.2
Og NR	0.96	0.76	491.2	310.4	252.2	238.8
Og Sc	0.95	0.75	704.8	445.7	362.1	330.4
Og SO	0.98	0.78	1249.0	789.0	640.9	554.4

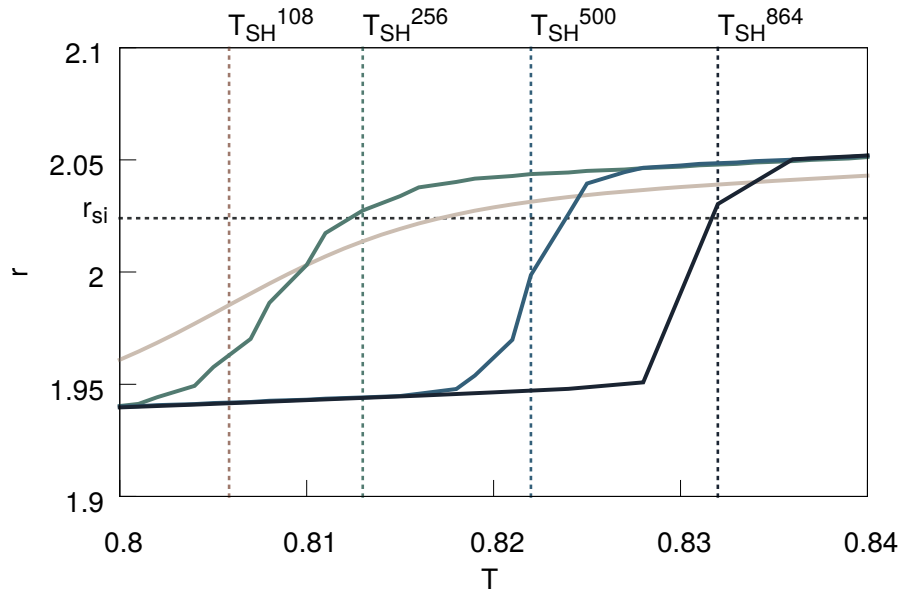

Figure 13.5.: Nearest neighbor distance as a function of temperature around the solid-liquid phase transition for the different simulated cell sizes. Vertical dotted lines correspond to superheated melting temperatures of the cells. The horizontal dotted line corresponds to the solid state inflection point. Reduced units are used.

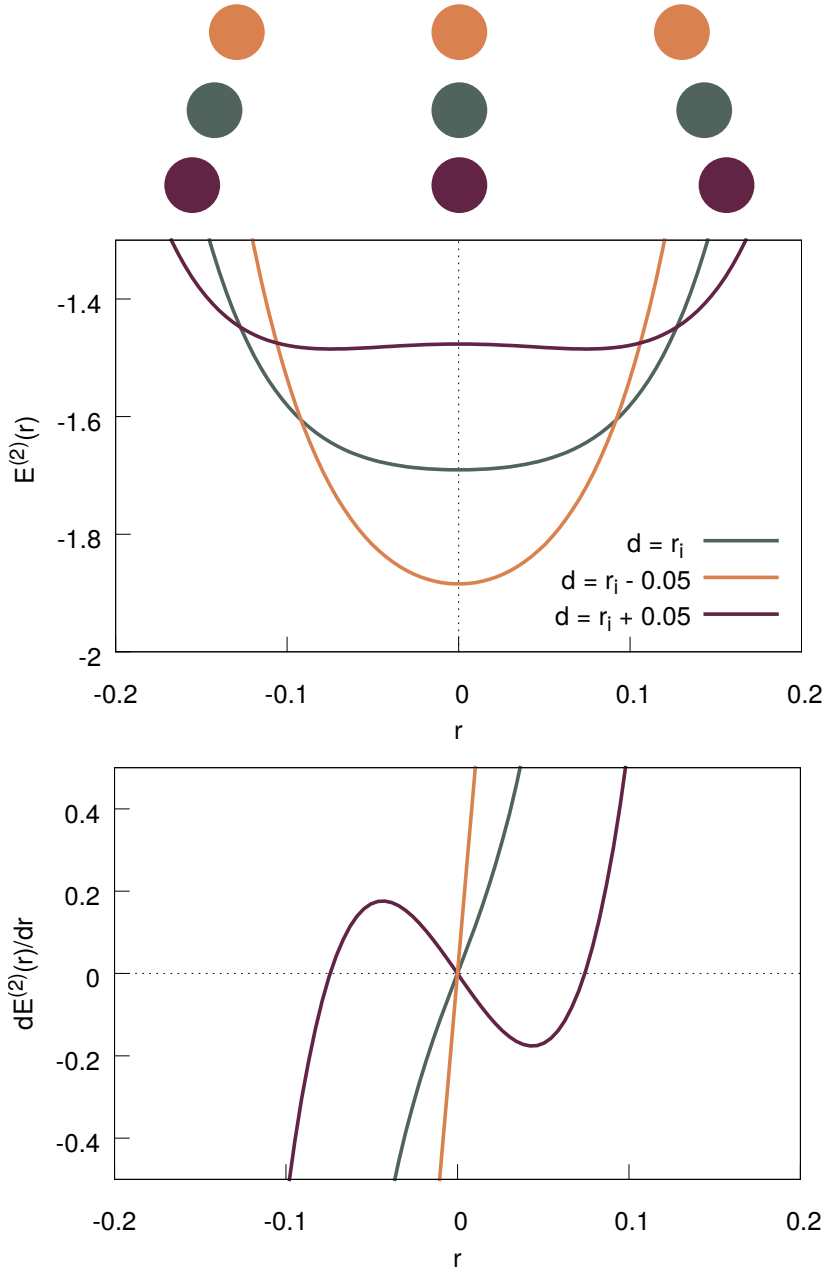

Figure 13.6.: Bifurcation upon expansion for a one dimensional three-atomic system. (Top) Abstract representation of the atom j at the center of atom $j-1$ and $j+1$. (Center) Onsite potential of a single atom j due to its interaction with atom $j-1$ and $j+1$ for distance below, at and above the inflection distance. (Bottom) Corresponding effective on-site forces.

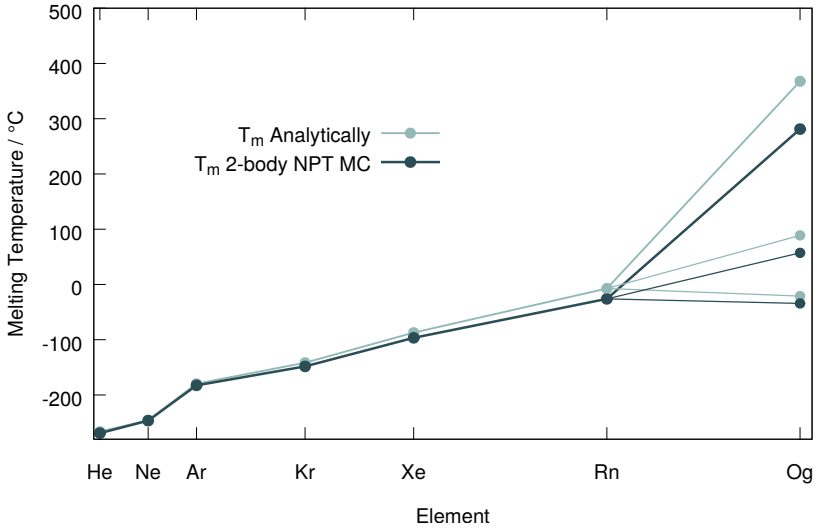

Figure 13.7.: Melting temperatures obtained from two-body NPT MC simulations versus melting temperatures obtained from the analytical formula.

14. Superheating

Superheating (and supercooling), also referred to as the hysteresis phenomenon, is a common problem one often encounters when determining the melting (solidification) temperature. Especially when carrying out melting simulations by employing crystals in periodic boundary conditions, the temperature of the solid-liquid phase transition is often influenced by superheating effects.

It is understood that the elementary mechanism of melting is connected to the formation of vacancies in solids and that melting is initiated from the surface [218–220]. It is thus quite intuitive to argue that for crystals that are in absence of a surface or impurities, the formation of vacancies is suppressed which leads to superheating phenomena. Although in our Monte Carlo studies the superheating effect was present in the periodic simulations, in the cluster simulations we obtained melting before the expected bulk melting temperature including pre-melting for the larger clusters. Indeed, our periodic simulations were performed starting from fcc crystals where impurities and vacancies were initially not present, whereas for the clusters the surface acted as a nucleation site which led to melting initiated from the surface. Hence, throughout this thesis the melting results of the periodic simulations were corrected by a superheating factor as derived by Belonoshko et al. [152]. However, there seems to be a lack of overall understanding exactly why superheating happens and why the superheating correction factor has this value.

We hope to provide some clarity in this chapter on the phenomenon of superheating. First an overview of superheating results in experiment and numerical simulations is given, after which the superheating correction factor is derived according to Belonoshko's et al. method. Then we show that in combination with our analytical melting results, superheating can be understood as an intrinsic character of melting rather then an technical problem that arises from the experiment or simulation method. The reader is also referred to a review in 2007 by Mei and Lu [220].

Superheating in the Experiment

Superheating of solids is usually difficult to obtain in experiments as solids will melt below T_m due to surface pre-melting, nonetheless many experiments have been carried out that tested the limit of superheating. Here we name a few.

One of the earliest studies on superheating was performed by Day and Allen [221] in 1905 who observed 300 K superheating in the tectosilicate albite ($NaAlSi_3O_8$). With a usual melting temperature of 1175 K, this means the albite was superheated by a factor of $\Theta^+ = 0.25$, where $\Theta^+ = T_{SH}/T_m - 1$. As another example, superheated lead with 120 K above the bulk melting temperature of 600.6 K was obtained by Herman et al. [222], corresponding to a superheating factor of $\Theta^+ = 0.2$. Ainslie [223] observed 300 K superheating in quartz. With a melting point of about 1670 K for β-quartz tridymite, this implies that the solid was superheated by a factor $\Theta^+ = 0.18$.

Superheating in Simulations

In contrast to experiment, superheating of solids in melting simulations is (almost) always encountered when simulations are performed with crystals without impurities or a surface. Indeed, as was discussed in Section 9.3, superheating can be avoided by introducing impurities in the sampled crystal. Numerical studies on superheating specifically were for example performed by Luo and Ahrens [224], who studied the superheating and supercooling by molecular dynamics simulations. They found that the highest and lowest temperature achievable in a superheated solid depends on a dimensionless nuclear barrier parameter and heating rate and obtained a maximum of superheating that varied between $\theta^+ = 0.06$ to 0.43. Furthermore, Luo et al. [225] performed shock induce superheating by molecular dynamic simulations and obtained superheating factors varying between Θ^+ of 0.19 to 0.3 and Bouchet et al [226] found a systematically overestimated melting temperature of at least $\Theta^+ = 0.20$ when studying the melting curve of aluminium employing MD simulations.

For embedded particles, as already argued in section 10.5.2, the melting temperature is influenced by the tension of the surface. When an embedded particle is coated by another element this can have a crucial influence on the superheating temperature. For our purposes studies of these kind are not of interest, as they merely underline the relation of melting with the interfacial structure rather than providing information of the superheating mechanism of perfect crystals which are in analogy with our periodic melting simulations.

Superheating is not only observed in large systems, but also in atomic clusters [227] and nanoparticles [228, 229]. (Which is in contrast to the expected lowering in temperature as discussed in section 10.5.2). A review on the superheating in nanoparticles is given by by Hendy and Gaston [230]. In contrast to bulk solids, the superheating in small metallic clusters is most likely due to to changes in the structure and chemical bonding and is therefore also not of interest for our study here.

14.1. The Asymptotic Value of Superheating

The superheating correction factor has been derived by Belonoshko et al. in the asymptotic limit (i.e. in the high pressure limit, $P \to \infty$, the change in volume upon heating goes to zero $\Delta V \to 0$.) [152]. The derivation of the correction factor will allows to better understand the mechanism that prevents a perfect crystals from melting at the presumed melting point.

Starting from MD simulations of a crystal of which the temperature is gradually increased, but the volume held constant (hence the pressure increases), they found that when the temperature approaches T_{SH}, a very small increase in kinetic energy leads to melting, after which the system evolves and drops down to T_m. The total energies at T_m and T_{SH}, at the same volume, are equal and hence one can write

$$U^s(V, T_{SH}) = U^l(V, T_m) \tag{14.1}$$

where U^s and U^l are the inner energy of the solid s and liquid l respectively.

This relation holds for melting curves of all simple solids in the high pressure limit, because in this limit the melting curve as a function becomes flat because of the small difference between the volumes of the liquid and solid. Subtracting the inner energy of a solid at the melting temperature, $U^s(T_m, V)$, on both sides of Eq. (14.1) leads to

$$U^s(T_{SH}, V) - U^s(T_m, V) = U^l(T_m, V) - U^s(T_m, V). \tag{14.2}$$

The inner energy satisfies the identity $U = TS - PV + G$. from the fact that in the high pressure limit $\Delta V = 0, \Delta P = 0$, assuming that the heat capacity of the solid at volume V and the temperature between T_{SH} and T_m is equal to $3k_B$ because of the equipartition theorem, and the entropy difference between a solid and a liquid at the same temperature is equal to $T_m k_B \ln 2$ (because $\Delta S = k_B \ln 2$ is the asymptotic value of the entropy [231] - we will come back to this in section 14.2), the following form is obtained

$$U^s(T_{SH}, V) - U^s(T_M, V) = U^l(T_m, V) - U^s(T_m, V) \tag{14.3}$$

$$C_v(T_{SH} - T_m) = -(P^l - P^s)(V^l - V^s) + T_m(S^l - S^s) \tag{14.4}$$

$$3k_B(T_{SH} - T_m) = 0 + T_m k_B \ln 2 \tag{14.5}$$

for which follows that the superheating correction factor is given by

$$\frac{T_{SH}}{T_m} = 1 + \frac{\ln 2}{3} \approx 1.23105 \tag{14.6}$$

Here the entropy difference between the solid and liquid state has been taken from the asymptotic limit of $\Delta V \to 0$. Showing that the superheating correction factor also approximately holds at ambient conditions is by no means

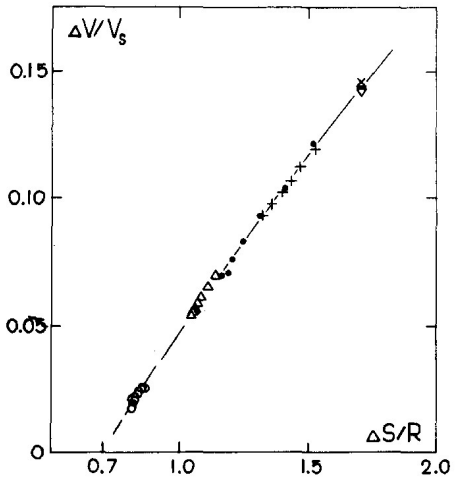

Figure 14.1.: Relation between the relative volume change $\Delta V/V_S$ and the melting entropy $\Delta S/R$ at melting of argon and sodium. Reprinted by permission from Elsevier [232] (1973)

a trivial task and is to our knowledge not proven yet. However, the similarity between the melting temperatures of the cluster results and the periodic simulations of the noble gases and the Lennard Jones potential in reduced units suggest that this correction factor is nevertheless a good approximation.

14.2. Entropy Upon Melting

Belonoshko used the entropy difference between the solid and liquid that was obtained by Stishov to derive the superheating factor. This result by Stishov [232] was obtained by analyzing experimental data of sodium and argon on the change in entropy at melting, $\Delta S/R$, as a function of relative change of volume at melting, $\Delta V/V_s$. The data shows that argon and sodium have clearly the same behavior and the melting entropy of these substance tends to $\ln 2$ when $\Delta V/V_s$ vanishes (See Fig. 14.1). This has also been partially confirmed by Lasocka for a number of metals [233].

At this stage it was not understood why the melting entropy has this value and if it also would hold for other pressures. However, as Stishov mentioned in his article [232], a similar factor was obtained by Lennard-Jones and Devonshire [234, 235] for entropy corresponding to the shuffling of N atoms among $2N$-sites. This article served as an inspiration for Stishov's further work, and indeed two years later Stishov managed to obtain a value of the change in entropy at melting [231, 236]. In order to derive this equality, he considered a system of M indistinguishable particles in a volume V divided into N numbered cells. The ordered state (solid) corresponds to $N = M$, that

is each cell contains a particle as depicted in Fig. 14.2. The partition function of a system of particles whose motion is not restricted by artificial cells is approximated by the probability of only double occupancy of cells. This means that single, double and zero occupied cells are allowed and a cell is be considered doubly occupied when the center of gravity of two particles fall inside it.

The change in entropy in going from a system of single occupancy of cells to a system with the possibility of double occupancy is then given by

$$\frac{\Delta S}{k} = \ln \sum_{M=0}^{N} \frac{N!}{M!\{[(N-M)/2]!\}^2 2^{N-M}} \tag{14.7}$$

the combinatorial factor under the summation sign is the number of ways of distributing M particles and $(N-M)/2$ pairs of particles over N positions. The maximum term correspond to the condition $M = N/2$, which implies that half of the particles exist in the pair state. This leads to the result

$$\Delta S = k \ln\left(2^{3/2N} \cdot 2^{-1/2N}\right) = R \ln 2 \tag{14.8}$$

with $R = kN$ being the gas constant. This is in agreement with the entropy of melting at constant volume taken from experiment.

Tallon and Cotterill [127, 129, 214, 237–239] also worked intensively on the value of the entropy of melting and also argued that the entropy of melting at constant volume equals $\Delta S = R \ln 2$. They made the important observation that the entropy at constant volume value could have its origin in the observed occurrence of bifurcated potential wells or alternatively arises from the localization of two sets of shear modes. Furthermore, they were able to include an additional factor to the entropy when melting does not occur at constant volume. It was argued that when the liquid and crystal at temperature T_m are not at the same volume, the entropy difference may be approximated by noting that the isothermal volume dependence of the entropy is give by $(\partial S/\partial V)_T = \alpha\beta_T$ where α is the volume coefficient of the thermal expansion and β_T is the isothermal bulk modulus. Including this additional term gives for the entropy difference upon melting

$$\Delta S_m = (\partial S/\partial V)_T \Delta V_m + S_0 \tag{14.9}$$

$$= \alpha\beta_T \Delta V_m + R \ln 2 \tag{14.10}$$

where the Maxwell relationship $(\partial S/\partial V)_T = (\partial P/\partial T)_V$ was used

14.3. Superheating as an Intrinsic Character of the System

Another important observation was made by Tallon [240]. He argued that there are different criteria at which the solid *has* to break down. In this case

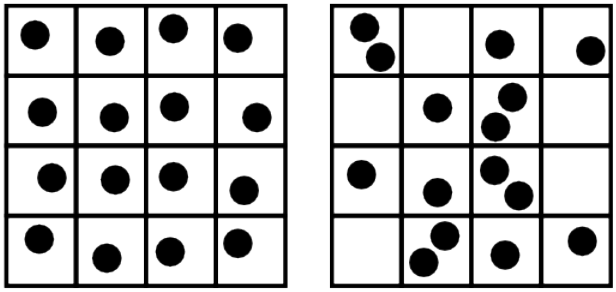

Figure 14.2.: (Left) Approximation of the solid state, (Right) approximation of the liquid state

the melting process is understood as a result of a type of lattice instability at the microscopic level. When a property of the crystal reaches an instability, the crystal has no other choice than melting.

Tallon makes the distinction between different types of instabilities, called catastrophes, which inevitable leads to melting. The entropy catastrophe T_m^s (where the entropy of the solid and the liquid are equal) is understood as an outer bound on the stability limit of the solid, see Fig. 14.3. A hierarchy of inner catastrophes occurs at lower superheating temperatures. For example the isochoric temperature T_m^v (the point at which the crystalline and the liquid phases have the same molar volume or density) represents a catastrophe point as beyond this point the crystal would be more dense then the liquid, and that would be unreasonable. For aluminum it was estimated to be at 1.28 T_m. Another catastrophe point is T_m^r, the point where the solid and the liquid have the same rigidity, which lies for aluminum at 1.24 T_m. Because T_m^r lies below T_m^v the last point is not observable since it is preceded by the rigidity catastrophe. This means that different superheating temperatures could in principle be obtained if other catastrophe points are being suppressed.

Now, let us recall that when deriving the analytical relation for the melting temperature the the solid-liquid phase transition did not appear at the melting temperature, but at a superheated temperature instead. This observation, in combination with the above argument of Tallon, teaches us an important point: Namely, the bifurcation of the on site potential is in this case the catastrophic character that leads to lattice instability and the temperature at which this happens corresponds to the superheating melting temperature. In this microscopic picture, the entropy is not taken into consideration, since we only consider the lattice instability due to symmetry breaking. This situation is in this respect identical to the periodic melting simulations of the crystal, since also in this case the atoms are trapped in their on-site potential and the solid-liquid phase transition will occur when the symmetry of the on-site potential is broken due to lattice vibrations exceeding the inflection point.

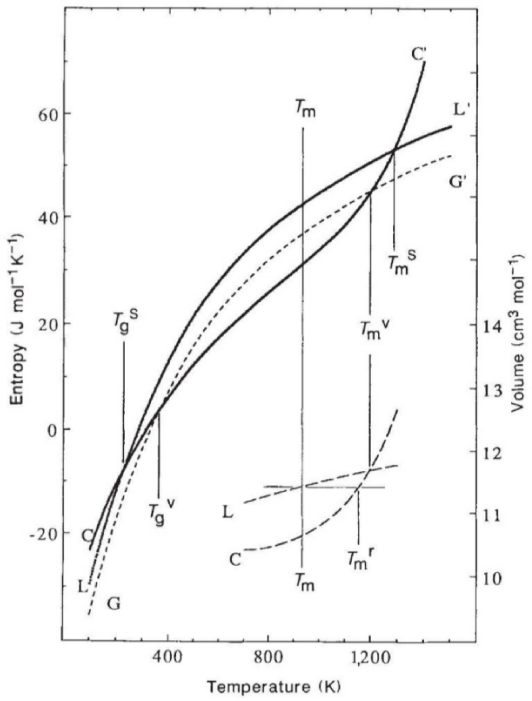

Figure 14.3.: The entropy of liquid (L) and crystalline (C) aluminium as functions of temperature at atmospheric pressure, showing the hierarchy of catastrophes as a succession of stability limits for the crystalline state. Reprinted by permission from Springer Nature [240] (1988)

Thus, our analytical relation is a direct analogy of our periodic simulations, and the correspondence of the analytically calculated melting point with the melting temperature obtained by the Monte Carlo simulations underline their similarity.

14.4. Superheating in the Analytical Results

In the previous chapter we derived an analytical relation between the ELJ fitting coefficients and temperature at which the solid breaks symmetry and melts. The correspondence between the temperature where the lattice instability occurs and the superheated temperature instead of the real melting temperature does not come as a surprise. In fact, it is in agreement with the findings we discussed in this chapter. Here we argued that superheating occurs when the contribution of entropy to the melting transition is not considered, which is the case when a system has no surface (i.e. is periodic) and has no impurities or defects. The analytical expression, Eq. (13.21), reflects

the same problem as the value of the cohesive energy and bulk modulus are computed for a perfect solid. Hence also here the temperature of the solid-liquid phase transition corresponds to the melting temperature of the infinite solid in absence of impurities or defects. The fact that the temperature of lattice instability does not correspond to the melting temperature was already briefly discussed by Maddox [241], who mentions that the Lindemann criterion is not thermodynamically sound since it does not take the free energy of the liquid state into account.

It is also possible to understand the lowering of the melting point due to the existence of a surface and/or impurities from a different perspective: both influence the (local) inflection point. Which implies that the atoms neighboring the surface or voids still melt when the atomic vibrations equal the amplitude of vibrations at the inflection point. However, due the to disturbance of the cohesive energy curve the length of vibrations at the inflection point is altered, hence lowering the transition temperature.

14.5. Final Remarks

Both the analytical relation and the periodic simulation rely on the lattice instability due to the vibrations exceeding the inflection point of the solid state cohesive energy curve. This means that the contribution to the melting temperature from the increase in entropy when going from a solid to a liquid state has not been taken into consideration and as a result the temperature of the solid-liquid phase transition does not correspond to the melting point one would obtain by comparing the free energies. Since we were able to derive the T_{SH} as occurring at the point where the symmetry of the on-site potential is broken, we conclude that the bifurcation is the cause of melting and the disappearance of the shear modulus is a resulting property. This nicely relates the microscopic to the macroscopic picture.

Part VI.

Summary and Conclusion

15. Summary

15.1. Conclusions

In this thesis, Monte Carlo simulations were carried out with the aim of obtaining the melting temperatures for the heavy noble gases. In order to determine the interaction potentials of krypton, xenon, radon and oganesson, highly accurate ab-initio two and three body potentials were developed using relativistic coupled cluster theory. These potentials were fitted to computationally efficient analytical functions, which were employed to calculate the interaction energy during the Monte Carlo melting simulation.

Parallel Tempering Monte Carlo simulations were performed during which random atomic moves were attempted with an acceptance probability based on the Boltzman distribution. 32 temperature trajectories were sampled simultaneously and exchange of configurations of two near-lying temperatures was attempted to increase the computational efficiency and overcome ergodicity problems. After the simulation the multihistogram method was employed to obtain the inner energy, volume, enthalpy and heat capacity as a smooth function of the temperature. The solid-liquid phase transition was then determined from the maximum of the peak in the heat capacity curve.

Two different techniques to obtain the melting temperature are presented in this thesis. First, the melting temperature was studied by simulating finite clusters in the canonical ensemble. Melting simulations were performed for Mackay icosahedral clusters of size $N = 13$, 55, 147, 309, 561, 923 and 1415 atoms considering two-body interactions only, and additional simulations were performed considering two+three-body interactions up to clusters containing 923 atoms. The melting temperatures were determined by extrapolation of the finite cluster results to the bulk value with inverse cluster radius. Two-body melting temperatures were obtained by extrapolation of the clusters $N = 147$ to 1415 and three-body corrections were taken as the difference in melting temperature when extrapolating clusters of size $N = 147$ to 923 including two- versus two+three-body interactions.

Second, the melting temperature was determined by direct sampling of the bulk using cells with periodic boundary conditions in the isobaric-isothermal ensemble at 1 atm pressure. It was demonstrated that the melting temperature converges with cell size to the superheated melting temperature. Hence, two-body melting temperatures were taken from the $N = 864$ cell, and three-body corrections were estimated from the difference in melting temperature

between the two-body only and two+three-body $N = 256$ cell. Upon correction for superheating we achieved excellent agreement with the melting temperature result of the cluster simulations.

There are multiple sources of error involved in calculating the melting temperatures. With regards to the cluster simulation, uncertainties arise from the extrapolation to the bulk temperature whereas for a cell with periodic boundary conditions the number of particles used in the cell and the estimate of the superheating correction factor give rise to errors.

The numerically determined melting temperatures of krypton and xenon are in close correspondence to the experimental values. That is, for krypton a melting temperature of $T_m^p = 109.5$ K and $T_m^c = 111.7$ K was obtained for periodic and cluster simulations respectively, which is approximately 5 K lower then the experimental value of 115.78 K. The melting point of xenon is determined to be $T_m^p = 156.1$ K and T_m^c =161.6 K, which is in close comparison to the experimental value of 161.40 K. The long debated value of radon of 202 K is confirmed by our simulations, namely we obtained a melting temperature of 200 K with both techniques.

Finally, for oganesson simulations were performed at three different levels of relativistic treatment (non-relativistic (NR), scalar relativistic (SR) and fully relativistic (SR+X2C)). Since oganesson with nuclear charge $Z = 118$ is such a heavy element, relativistic effects are expected to have large contributions to the interaction potential. Indeed, we found that upon considering relativistic effects, the interaction between the atoms increases significantly, that is two-body interactions are more attractive whereas the smaller three-body interactions are more repulsive. Consequently, the two-body melting temperatures of the spin-orbit corrected potentials increased with respect to the NR and SR calculations, whereas the three-body correction lowers the melting point by a rather large amount upon inclusion of relativistic effects. As a result the computed melting temperature of oganesson is remarkably high when a fully relativistic treatment for the interactions is considered, i.e. $T_m^p = 324$ K $T_m^c = 320$ K in comparison to $T_m^p = 268.3$ and $T_m^c = 269.8$ for the SR level and $T_m^p = 220.7$ K and $T_m^c = 229.1$ K for the NR potential. This implies that oganesson is a solid at ambient conditions. For oganesson the SR+X2C three-body contribution is extremely large and therefore four-body forces are also expected to have a significant contribution to the melting point. However, these are of attractive type and therefore the given melting temperatures should be interpreted as a lower bound to the correct melting temperature.

In the final part of this thesis an analytical relation between the two-body interaction potential and the melting temperature is developed. It is shown that the temperature of the solid-liquid phase transition is related to the point where upon expansion, the symmetry in the atomic interaction as a function of nearest neighbour distance is broken, i.e., a bifurcation of the on-site po-

tential occurs. This was demonstrated numerically by studies on the Lennard-Jones potential in reduced units in combination with an analytical expression for the cohesive energy as a function of the nearest neighbor distance.

The knowledge that a solid-liquid phase transition occurs upon bifurcation of the onsite potential has already been speculated on in the past. What had not been shown before, is that the analytical form of the cohesive energy and bulk modulus, in combination with a previously derived expression for the lattice vibrations as a function of bulk modules and solid state equilibrium distance, enables us to relate the melting temperature to lattice vibrations and to obtain an analytical expression for the solid-liquid phase transition. Interestingly, the analytically calculated temperature of the solid-liquid phase transition is in correspondence with the superheated temperature. This result is not surprising as entropic contributions are not considered when the temperature of the solid-liquid phase transition is related to the lattice instability upon symmetry breaking. This insight makes us realize that the less well understood phenomenum of superheating is an intrinsic character of the solid, instead of a problematic component of the melting process.

15.2. Future developments

In future work, we intend to study the melting of oganesson by means of free energy density functional and ab-initio calculations to confirm its melting point and to test the reliability of dispersion corrected density functionals allowing us to go beyond the three-body interaction. Further work should also include the study of the lighter noble gases, helium and neon. For this a MC algorithm that includes quantum effects needs to be developed. In the past, quantum delocalization has been included in the melting study of neon employing quantum-corrected potentials in the simulation [154], however, we wish to turn to a more accurate treatment using quantum Monte Carlo methods. Furthermore, it would be interesting to see if the analytical relation between the melting point and interaction potential can be extended to a form such that also higher order interactions are included, or alternatively if the relation can be expressed in terms of an effective potential such that the analytical relation can be extended to systems for which the many expansion breaks down such as metallic systems. Also the next logical step is to simulate the liquid-to-gas phase transition, which is inherently difficult because of the sudden large change in volume and therefore has rarely been attempted in the past.

Appendices

MASSEY UNIVERSITY
GRADUATE RESEARCH SCHOOL

STATEMENT OF CONTRIBUTION
DOCTORATE WITH PUBLICATIONS/MANUSCRIPTS

We, the candidate and the candidate's Primary Supervisor, certify that all co-authors have consented to their work being included in the thesis and they have accepted the candidate's contribution as indicated below in the *Statement of Originality*.

Name of candidate:	Odile Smits
Name/title of Primary Supervisor:	Peter Schwerdtfeger
Name of Research Output and full reference:	
A relativistic coupled-cluster interaction potential and rovibrational constants for the xenon dimer	
In which Chapter is the Manuscript /Published work:	5,7,8,11
Please indicate:	
• The percentage of the manuscript/Published Work that was contributed by the candidate:	50
and	
• Describe the contribution that the candidate has made to the Manuscript/Published Work:	
Fitting of the ab-initio potentials to analytical functions Figures are made by candidate Contributions to writing of manuscript	
For manuscripts intended for publication please indicate target journal:	
Candidate's Signature:	
Date:	22 February 2019
Primary Supervisor's Signature:	
Date:	22 February 2019

(This form should appear at the end of each thesis chapter/section/appendix submitted as a manuscript/ publication or collected as an appendix at the end of the thesis)

MASSEY UNIVERSITY
GRADUATE RESEARCH SCHOOL

STATEMENT OF CONTRIBUTION
DOCTORATE WITH PUBLICATIONS/MANUSCRIPTS

We, the candidate and the candidate's Primary Supervisor, certify that all co-authors have consented to their work being included in the thesis and they have accepted the candidate's contribution as indicated below in the *Statement of Originality*.

Name of candidate:	Odile Smits
Name/title of Primary Supervisor:	Peter Schwerdtfeger
Name of Research Output and full reference:	
Solid Oganesson via a Many-Body Interaction Expansion Based on Relativistic Coupled-Cluster Theory and from Plane-Wave Relativistic Density Functional Theory	
In which Chapter is the Manuscript /Published work:	5,7,8,11
Please indicate:	
• The percentage of the manuscript/Published Work that was contributed by the candidate:	40
and	
• Describe the contribution that the candidate has made to the Manuscript/Published Work:	
Fitting of the ab-initio potentials to analytical functions Figures were made by candidate Contributions to writing of manuscript	
For manuscripts intended for publication please indicate target journal:	
Journal of physical chemistry	
Candidate's Signature:	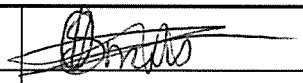
Date:	22 February 2019
Primary Supervisor's Signature:	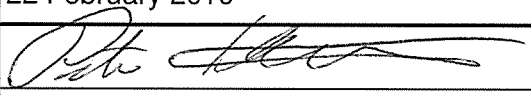
Date:	22 February 2019

(This form should appear at the end of each thesis chapter/section/appendix submitted as a manuscript/ publication or collected as an appendix at the end of the thesis)

MASSEY UNIVERSITY
GRADUATE RESEARCH SCHOOL

STATEMENT OF CONTRIBUTION
DOCTORATE WITH PUBLICATIONS/MANUSCRIPTS

We, the candidate and the candidate's Primary Supervisor, certify that all co-authors have consented to their work being included in the thesis and they have accepted the candidate's contribution as indicated below in the *Statement of Originality*.

Name of candidate:	Odile Smits
Name/title of Primary Supervisor:	Peter Schwerdtfeger
Name of Research Output and full reference:	
A HundredYearOld Experiment Reevaluated: Accurate AbInitio MonteCarlo Simulations of the Melting of Radon	
In which Chapter is the Manuscript /Published work:	5,7,8,11
Please indicate:	
• The percentage of the manuscript/Published Work that was contributed by the candidate:	90
and	
• Describe the contribution that the candidate has made to the Manuscript/Published Work:	
Fitting of the ab-initio potentials to analytical functions Calculation of melting temperatures Figures were made by candidate, Contributions to writing of manuscript	
For manuscripts intended for publication please indicate target journal:	
Candidate's Signature:	
Date:	22 February 2019
Primary Supervisor's Signature:	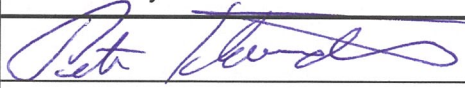
Date:	22 February 2019

(This form should appear at the end of each thesis chapter/section/appendix submitted as a manuscript/ publication or collected as an appendix at the end of the thesis)

Bibliography

[1] B. W. Gray and W. Ramsay, Zeitschrift für Physikalische Chemie **70**, 116 (1910).

[2] W. M. Haynes, *Crc handbook of chemistry and physics* (CRC press, 2014).

[3] Y. T. Oganessian, V. K. Utyonkov, Y. V. Lobanov, F. S. Abdullin, A. N. Polyakov, R. N. Sagaidak, I. V. Shirokovsky, Y. S. Tsyganov, A. A. Voinov, G. G. Gulbekian, S. L. Bogomolov, B. N. Gikal, A. N. Mezentsev, S. Iliev, V. G. Subbotin, A. M. Sukhov, K. Subotic, V. I. Zagrebaev, G. K. Vostokin, M. G. Itkis, K. J. Moody, J. B. Patin, D. A. Shaughnessy, M. A. Stoyer, N. J. Stoyer, P. A. Wilk, J. M. Kenneally, J. H. Landrum, J. F. Wild, and R. W. Lougheed, Phys. Rev. C **74**, 044602 (2006).

[4] Y. T. Oganessian, Pure Appl. Chem. **78**, 889 (2006).

[5] P. J. Karol, R. C. Barber, B. M. Sherrill, E. Vardaci, and T. Yamazaki, Pure and Applied Chemistry **88**, 155 (2016).

[6] S. Giuliani, Z. Matheson, W. Nazarewicz, E. Olsen, P.-G. Reinhard, J. Sadhukhan, B. Schuetrumpf, N. Schunck, and P. Schwerdtfeger, Reviews of Modern Physics **91**, 011001 (2019).

[7] C. S. Nash, The Journal of Physical Chemistry A **109**, 3493 (2005).

[8] D. C. Rapaport and D. C. R. Rapaport, *The art of molecular dynamics simulation* (Cambridge university press, 2004).

[9] D. P. Landau and K. Binder, *A guide to monte carlo simulations in statistical physics* (Cambridge university press, 2014).

[10] E. Pahl, F. Calvo, L. Koci, and P. Schwerdtfeger, Angewandte Chemie International Edition **47**, 8207 (2008).

[11] E. Pahl, F. Calvo, and P. Schwerdtfeger, International Journal of Quantum Chemistry **109**, 1812 (2009).

[12] F. Senn, J. Wiebke, O. Schumann, S. Gohr, P. Schwerdtfeger, and E. Pahl, The Journal of Chemical Physics **140**, 044325 (2014).

[13] V. Bocchetti and H. T. Diep, The Journal of Chemical Physics **138**, 104122 (2013).

[14] J. Wiebke, E. Pahl, and P. Schwerdtfeger, Angewandte Chemie International Edition **52**, 13202 (2013).

[15] P. Jerabek, B. Schuetrumpf, P. Schwerdtfeger, and W. Nazarewicz, Physical Review Letters. **120**, 053001 (2018).

[16] T. Helgaker, P. Jorgensen, and J. Olsen, *Molecular electronic-structure theory* (John Wiley & Sons, 2014).

[17] M. Reiher and A. Wolf, *Relativistic quantum chemistry: the fundamental theory of molecular science* (John Wiley & Sons, 2014).

[18] A. Szabo and N. S. Ostlund, *Modern quantum chemistry: introduction to advanced electronic structure theory* (Courier Corporation, 2012).

[19] F. Jensen, *Introduction to computational chemistry* (John wiley & sons, 2017).

[20] G. D. Purvis III and R. J. Bartlett, The Journal of Chemical Physics **76**, 1910 (1982).

[21] K. Raghavachari, G. W. Trucks, J. A. Pople, and M. Head-Gordon, Chemical Physics Letters **157**, 479 (1989).

[22] P. Pyykkö, Chemical Reviews **88**, 563 (1988).

[23] W. H. E. Schwarz, E. M. van Wezenbeek, E. J. Baerends, and J. G. Snijders, Journal of Physics B **22**, 1515 (1989).

[24] W. H. E. Schwarz, P. Schwerdtfeger, J. G. Snijders, and E. J. Baerends, Journal of Physics B **23**, 3225 (1990).

[25] J. Autschbach, S. Siekierski, M. Seth, P. Schwerdtfeger, and W. H. E. Schwarz, Journal of Computational Chemistry **23**, 804 (2002).

[26] K. G. Dyall and K. Fægri Jr, *Introduction to relativistic quantum chemistry* (Oxford University Press, 2007).

[27] W. Liu, Molecular Physics **108**, 1679 (2010).

[28] J. Sikkema, L. Visscher, T. Saue, and M. Iliaš, The Journal of Chemical Physics **131**, 124116 (2009).

[29] C. Chang, M. Pelissier, and P. Durand, Physica Scripta **34**, 394 (1986).

[30] E. Van Lenthe, R. Van Leeuwen, E. Baerends, and J. Snijders, International Journal of Quantum Chemistry **57**, 281 (1996).

[31] L. L. Foldy and S. A. Wouthuysen, Physical Review **78**, 29 (1950).

[32] M. Douglas and N. M. Kroll, Annals of Physics **82**, 89 (1974).

[33] B. A. Hess, Physical Review A **32**, 756 (1985).

[34] B. A. Hess, Physical Review A **33**, 3742 (1986).

[35] K. G. Dyall, Theoretical Chemistry Accounts **115**, 441 (2006).

[36] F. B. Van Duijneveldt, J. G. van Duijneveldt-van de Rijdt, and J. H. van Lenthe, Chemical Reviews **94**, 1873 (1994).

[37] S. F. Boys and F. d. Bernardi, Molecular Physics **19**, 553 (1970).

[38] T. Dunning Jr, The Journal of Chemical Physics **90**, 1007 (1989).

[39] W. Kutzelnigg and J. D. Morgan III, The Journal of Chemical Physics **96**, 4484 (1992).

[40] R. N. Hill, The Journal of Chemical Physics **83**, 1173 (1985).

[41] A. Halkier, T. Helgaker, P. Jørgensen, W. Klopper, H. Koch, J. Olsen, and A. K. Wilson, Chemical Physics Letters **286**, 243 (1998).

[42] A. G. Csaszar, W. D. Allen, Y. Yamaguchi, and H. Schaefer, *Ab initio determination of accurate ground electronic state potential energy hypersurfaces for small molecules* (John Wiley & Sons: London, 2000).

[43] W. Klopper, Molecular Physics **99**, 481 (2001).

[44] P. Jerabek, O. Smits, E. Pahl, and P. Schwerdtfeger, Molecular Physics, 1 (2017).

[45] O. R. Smits, P. Jerabek, E. Pahl, and P. Schwerdtfeger, Angewandte Chemie International Edition **57**, 9961 (2018).

[46] P. Jerabek, O. R. Smits, J.-M. Mewes, K. A. Peterson, and P. Schwerdtfeger, The Journal of Physical Chemistry A **123**, PMID: 31017443, 4201 (2019).

[47] B. Jager, R. Hellmann, E. Bich, and E. Vogel, The Journal of Chemical Physics **144**, 114304 (2016).

[48] H.-J. Werner, P. J. Knowles, G. Knizia, F. R. Manby, M. Schütz, P. Celani, W. Györffy, D. Kats, T. Korona, R. Lindh, A. Mitrushenkov, G. Rauhut, K. R. Shamasundar, T. B. Adler, R. D. Amos, A. Bernhardsson, A. Berning, D. L. Cooper, M. J. O. Deegan, A. J. Dobbyn, F. Eckert, E. Goll, C. Hampel, A. Hesselmann, G. Hetzer, T. Hrenar, G. Jansen, C. Köppl, Y. Liu, A. W. Lloyd, R. A. Mata, A. J. May, S. J. McNicholas, W. Meyer, M. E. Mura, A. Nicklass, D. P. O'Neill, P. Palmieri, D. Peng, K. Pflüger, R. Pitzer, M. Reiher, T. Shiozaki, H. Stoll, A. J. Stone, R. Tarroni, T. Thorsteinsson, and M. Wang, *MOLPRO, version 2015.1, A package of ab initio programs*, 2015.

[49] H. J. Werner, P. J. Knowles, G. Knizia, F. R. Manby, and M. Schütz, Wiley Interdisciplinary Reviews: Computational Molecular Science **2**, 242 (2012).

[50] C. Hampel, K. A. Peterson, and H. J. Werner, Chemical Physics Letters **190**, 1 (1992).

[51] M. J. O. Deegan and P. J. Knowles, Chemical Physics Letters **227**, 321 (1994).

[52] S. F. Boys and F. Bernardi, Mol. Phys. **19**, 553 (1970).

[53] D. H. Bross and K. A. Peterson, in *Thom h. dunning, jr.* (Springer, 2015), pp. 19–30.

[54] A. Wolf, M. Reiher, and B. A. Hess, The Journal of Chemical Physics **117**, 9215 (2002).

[55] M. Reiher and A. Wolf, The Journal of Chemical Physics **121**, 2037 (2004).

[56] M. Reiher and A. Wolf, The Journal of Chemical Physics **121**, 10945 (2004).

[57] D. Peng and M. Reiher, Theoretical Chemistry Accounts **131**, 1081 (2012).

[58] M. Kállay, Z. Rolik, J. Csontos, I. Ladjánszki, L. Szegedy, B. Ladóczki, G. Samu, K. Petrov, M. Farkas, P. Nagy, D. Mester, and B. Hégely, *MRCC, a Quantum Chemical Program Suite.*

[59] Z. Rolik, L. Szegedy, I. Ladjánszki, B. Ladóczki, and M. Kállay, The Journal of Chemical Physics **139**, 094105 (2013).

[60] M. Kállay and J. Gauss, The Journal of Chemical Physics **123**, 214105 (2005).

[61] M. Kállay and J. Gauss, The Journal of Chemical Physics **129**, 144101 (2008).

[62] Y. J. Bomble, J. F. Stanton, M. Kállay, and J. Gauss, The Journal of Chemical Physics **123**, 054101 (2005).

[63] DIRAC, a relativistic ab initio electronic structure program, Release DIRAC15 (2015), written by R. Bast, T. Saue, L. Visscher, and H. J. Aa. Jensen, with contributions from V. Bakken, K. G. Dyall, S. Dubillard, U. Ekstroem, E. Eliav, T. Enevoldsen, E. Fasshauer, T. Fleig, O. Fossgaard, A. S. P. Gomes, T. Helgaker, J. Henriksson, M. Ilias, Ch. R. Jacob, S. Knecht, S. Komorovsky, O. Kullie, J. K. Laerdahl, C. V. Larsen, Y. S. Lee, H. S. Nataraj, M. K. Nayak, P. Norman, G. Olejniczak, J. Olsen, Y. C. Park, J. K. Pedersen, M. Pernpointner, R. Di Remigio, K. Ruud, P. Salek, B. Schimmelpfennig, J. Sikkema, A. J. Thorvaldsen, J. Thyssen, J. van Stralen, S. Villaume, O. Visser, T. Winther, and S. Yamamoto (see http://www.diracprogram.org).

[64] L. Visscher, E. Eliav, and U. Kaldor, The Journal of Chemical Physics **115**, 9720 (2001).

[65] K. G. Dyall, Theoretical Chemistry Accounts **108**, 365 (2002).

[66] J. Sikkema, L. Visscher, T. Saue, and M. Iliaš, The Journal of Chemical Physics **131**, 124116 (2009).

[67] W. Cencek, G. Garberoglio, A. H. Harvey, M. O. McLinden, and K. Szalewicz, The Journal of Physical Chemistry A **117**, 7542 (2013).

[68] A. Stone, *The theory of intermolecular forces* (Oxford University Press, Oxford, 2013).

[69] H. Margenau, N. R. Kestner, and D. Ter Haar, *Theory of intermolecular forces* (Elsevier Science, 1971).

[70] H. Casimir and D. Polder, Physical Review **73**, 360 (1948).

[71] M. Born and J. E. Mayer, Zeitschrift für Physik **75**, 1 (1932).

[72] R. Jaquet, in *Potential energy surfaces* (Springer, 1999), pp. 97–175.

[73] P. Schwerdtfeger, N. Gaston, R. P. Krawczyk, R. Tonner, and G. E. Moyano, Physical Review B **73**, 064112 (2006).

[74] W. Bade, The Journal of Chemical Physics **27**, 1280 (1957).

[75] G. Mie, Annalen der Physik **316**, 657 (1903).

[76] F. Simon and C. von Simson, Zeitschrift für Physik **25**, 160 (1924).

[77] S. C. Wang, Phys. Zeit **28**, 663 (1927).

[78] J. E. Lennard-Jones, Proceedings of the Royal Societey A **106**, 463 (1924).

[79] J. E. Lennard-Jones, Proc. R. Soc. Lond. A **129**, 598 (1930).

[80] J. Lennard-Jones, Nature **128**, 462 (1931).

[81] R. Eisenschitz and F. London, Zeitschrift für Physik **60**, 491 (1930).

[82] H. R. Hassé, in Mathematical proceedings of the cambridge philosophical society, Vol. 26, 4 (Cambridge University Press, 1930), pp. 542–555.

[83] R. Ahlrichs, R. Penco, and G. Scoles, Chemical Physics **19**, 119 (1977).

[84] R. A. Aziz and H. Chen, The Journal of Chemical Physics **67**, 5719 (1977).

[85] R. Aziz, V. Nain, J. Carley, W. Taylor, and G. McConville, The Journal of Chemical Physics **70**, 4330 (1979).

[86] B. Jäger, R. Hellmann, E. Bich, and E. Vogel, Molecular Physics **107**, 2181 (2009).

[87] R. Hellmann, B. Jäger, and E. Bich, The Journal of Chemical Physics **147**, 034304 (2017).

[88] K. Tang and J. Toennies, The Journal of Chemical Physics **66**, 1496 (1977).

[89] A. Dalgarno and J. Lewis, Proceedings of the Physical Society. Section A **69**, 57 (1956).

[90] R. Bell, Journal of Physics B: Atomic and Molecular Physics **3**, 751 (1970).

[91] A. J. Thakkar, H. Hettema, and P. E. Wormer, The Journal of Chemical Physics **97**, 3252 (1992).

[92] L. Bruch and I. J. McGee, The Journal of Chemical Physics **59**, 409 (1973).

[93] O. Novaro and V. Beltrán-López, The Journal of Chemical Physics **56**, 815 (1972).

[94] P. Loubeyre, Physical review letters **58**, 1857 (1987).

[95] B. Axilrod and E. Teller, The Journal of Chemical Physics **11**, 299 (1943).

[96] M. Doran, Journal of Physics B: Atomic and Molecular Physics **7**, 558 (1974).

[97] A. Kumar and W. J. Meath, Molecular Physics **54**, 823 (1985).

[98] A. Kumar and A. J. Thakkar, The Journal of Chemical Physics **132**, 074301 (2010).

[99] L.-Y. Tang, Z.-C. Yan, T.-Y. Shi, J. F. Babb, and J. Mitroy, The Journal of Chemical Physics **136**, 104104 (2012).

[100] M. Neumann and M. Zoppi, Physical Review B **62**, 41 (2000).

[101] P. Schwerdtfeger and A. Hermann, Physical Review B **80**, 064106 (2009).

[102] K. Tang and J. P. Toennies, The Journal of Chemical Physics **74**, 1148 (1981).

[103] J. M. Waldrop, B. Song, K. Patkowski, and X. Wang, The Journal of Chemical Physics **142**, 204307 (2015).

[104] A. Kumar and W. J. Meath, Mol. Phys. **54**, 823 (1985).

[105] U. Hohm and K. Kerl, Molecular Physics **69**, 803 (1990).

[106] W. Cencek, K. Patkowski, and K. Szalewicz, The Journal of Chemical Physics **131**, 064105 (2009).

[107] J. Dunham, Physical Review **41**, 721 (1932).

[108] K. P. Huber and G. Herzberg, NIST chemistry webBook, NIST standard reference database, 20899 (2000).

[109] D. Freeman, K. Yoshino, and Y. Tanaka, The Journal of Chemical Physics **61**, 4880 (1974).

[110] A. Wüest, U. Hollenstein, K. De Bruin, and F. Merkt, Canadian journal of chemistry **82**, 750 (2004).

[111] M. Hanni, P. Lantto, N. Runeberg, J. Jokisaari, and J. Vaara, The Journal of Chemical Physics **121**, 5908 (2004).

[112] Z.-Y. Tu, W.-L. Wang, R.-Z. Li, C.-J. Xia, and L.-B. Li, Chemical Physics Letters **655**, 55 (2016).

[113] A. Shee, S. Knecht, and T. Saue, Physical Chemistry Chemical Physics **17**, 10978 (2015).

[114] O. Kullie and T. Saue, Chem. Phys. **395**, Recent Advances and Applications of Relativistic Quantum Chemistry, 54 (2012).

[115] A. Shee, S. Knecht, and T. Saue, **17**, 10978 (2015).

[116] C. S. Nash, The Journal of Physical Chemistry A **109**, 3493 (2005).

[117] D. E. Freeman, K. Yoshino, and Y. Tanaka, The Journal of Chemical Physics **61**, 4880 (1974).

[118] A. Wüest, U. Hollenstein, K. G. de Bruin, and F. Merkt, Can. J. Chem. **82**, 750 (2004).

[119] P. Attard, Phys. Rev. A **45**, 5649 (1992).

[120] G. J. M. Koper and H. Reiss, J. Phys. Chem. **100**, 422 (1996).

[121] E. J. Meijer and D. Frenkel, The Journal of Chemical Physics **94**, 2269 (1991).

[122] F. Lindemann, Phys. Z. **11**, 609 (1910).

[123] R. Etters and J. Kaelberer, Physical Review A **11**, 1068 (1975).

[124] R. Etters and J. Kaelberer, The Journal of Chemical Physics **66**, 5112 (1977).

[125] R. Berry, T. Beck, H. Davis, and J. Jellinek, in *Advances in chemical physics*, Vol. 70 (Wiley New York, 1988), p. 35.

[126] M. Born, The Journal of Chemical Physics **7**, 591 (1939).

[127] J. Tallon, W. Robinson, and S. Smedley, Nature **266**, 337 (1977).

[128] R. Cotterill, Journal of Crystal Growth **48**, 582 (1980).

[129] R. M. Cotterill and J. L. Tallon, Faraday Discussions of the Chemical Society **69**, 241 (1980).

[130] S.-N. Luo, A. Strachan, and D. C. Swift, The Journal of Chemical Physics **120**, 11640 (2004).

[131] L. Zheng, S.-N. Luo, and D. L. Thompson, The Journal of Chemical Physics **124**, 154504 (2006).

[132] F. Perakis, K. Amann-Winkel, F. Lehmkühler, M. Sprung, D. Mariedahl, J. A. Sellberg, H. Pathak, A. Späh, F. Cavalca, D. Schlesinger, A. Ricci, A. Jain, B. Massani, F. Aubree, C. J. Benmore, T. Loerting, G. Grübel, L. G. M. Pettersson, and A. Nilsson, Proceedings of the National Academy of Sciences **114**, 8193 (2017).

[133] S. Phillpot, J. Lutsko, D. Wolf, and S. Yip, Physical Review B **40**, 2831 (1989).

[134] G. F. Velardez, S. Alavi, and D. L. Thompson, The Journal of Chemical Physics **120**, 9151 (2004).

[135] J. R. Morris, C. Wang, K. Ho, and C. Chan, Physical Review B **49**, 3109 (1994).

[136] S. Yoo, S. S. Xantheas, and X. Cheng, Chemical Physics Letters **481**, 88 (2009).

[137] U. R. Pedersen, F. Hummel, G. Kresse, G. Kahl, and C. Dellago, Physical Review B **88**, 094101 (2013).

[138] K. G. Steenbergen, E. Pahl, and P. Schwerdtfeger, The Journal of Physical Chemistry Letters **8**, 1407 (2017).

[139] W. G. Hoover and F. H. Ree, The Journal of Chemical Physics **47**, 4873 (1967).

[140] D. Frenkel and A. J. Ladd, The Journal of Chemical Physics **81**, 3188 (1984).

[141] G. Grochola, The Journal of Chemical Physics **120**, 2122 (2004).

[142] O. Sugino and R. Car, Physical review letters **74**, 1823 (1995).

[143] G. A. de Wijs, G. Kresse, and M. J. Gillan, Physical Review B **57**, 8223 (1998).

[144] D. Alfè, M. Gillan, and G. Price, The Journal of Chemical Physics **116**, 6170 (2002).

[145] D. Alfe, L. Vočadlo, G. Price, and M. Gillan, Journal of Physics: Condensed Matter **16**, S973 (2004).

[146] L.-F. Zhu, B. Grabowski, and J. Neugebauer, Physical Review B **96**, 224202 (2017).

[147] F. Dorner, Z. Sukurma, C. Dellago, and G. Kresse, Physical Review Letters. **121**, 195701 (2018).

[148] N. Metropolis, A. W. Rosenbluth, M. N. Rosenbluth, A. H. Teller, and E. Teller, The journal of chemical physics **21**, 1087 (1953).

[149] D. Bouzida, S. Kumar, and R. Swendsen, Physical Review A **45**, 8894 (1992).

[150] R. H. Swendsen, Physics Procedia **15**, 81 (2011).

[151] R. H. Swendsen and J.-S. Wang, Physical review letters **57**, 2607 (1986).

[152] A. B. Belonoshko, N. Skorodumova, A. Rosengren, and B. Johansson, Physical Review B **73**, 012201 (2006).

[153] S. Valkealahti and M. Manninen, Journal of chemical physics **106**, 1888 (1997).

[154] E. Pahl, F. Calvo, L. Ko??i, and P. Schwerdtfeger, Angewandte Chemie - International Edition **47**, 8207 (2008).

[155] F. Senn, J. Wiebke, O. Schumann, S. Gohr, P. Schwerdtfeger, and E. Pahl, The Journal of Chemical Physics **140**, 44325 (2014).

[156] A. M. Ferrenberg and R. H. Swendsen, Physical review letters **61**, 2635 (1988).

[157] A. M. Ferrenberg and R. H. Swendsen, Physical Review Letters **63**, 1195 (1989).

[158] A. Ghoufi, F. Goujon, V. Lachet, and P. Malfreyt, Journal of Chemical Physics **128** (2008) 10.1063/1.2904460.

[159] T. Bereau and R. H. Swendsen, Journal of Computational Physics **228**, 6119 (2009).

[160] C. H. Bennett, Journal of Computational Physics **22**, 245 (1976).

[161] R. S. Berry, T. L. Beck, H. L. Davis, and J. Jellinek, Evolution of Size Effects in Chemical Dynamics, Part **2**, 1 (1988).

[162] K. Binder and D. P. Landau, Physical Review B **30**, 1477 (1984).

[163] Y. Imry, Physical Review B **21**, 2042 (1980).

[164] P. Buffat and J.-P. Borel, Physical review A **13** (1976).

[165] P. Pawlow, Zeitschrift für Physikalische Chemie **65**, 545 (1909).

[166] R. Defay and I. Prigogine, *Surface tension and adsorption* (Wiley, 1966).

[167] F. Baletto and R. Ferrando, Reviews of modern physics **77**, 371 (2005).

[168] H. Reiss and I. B. Wilson, Journal of Colloid Science **3**, 551 (1948).

[169] K.-J. Hanszen, Zeitschrift für Physik **157**, 523 (1960).

[170] J. R. Sambles, Proceedings of the Royal Society A: Mathematical, Physical and Engineering Sciences **324**, 339 (1971).

[171] Y. G. Chushak and L. S. Bartell, Journal of Physical Chemistry B **105**, 11605 (2001).

[172] R. Kofman, P. Cheyssac, A. Aouaj, Y. Lereah, G. Deutscher, T. Ben-David, J. M. Penisson, and A. Bourret, Surface Science **303**, 231 (1994).

[173] R. Garrigos, P. Cheyssac, and R. Kofman, Zeitschrift für Physik D Atoms, Molecules and Clusters **12**, 497 (1989).

[174] G. A. Breaux, R. C. Benirschke, T. Sugai, B. S. Kinnear, and M. F. Jarrold, Physical Review Letters **91**, 215508 (2003).

[175] K. Steenbergen and N. Gaston, Physical Review B **88**, 161402 (2013).

[176] K. G. Steenbergen and N. Gaston, Physical Chemistry Chemical Physics **15**, 15325 (2013).

[177] T. L. Hill, The Journal of Chemical Physics **36**, 3182 (1962).

[178] D. Frantz, The Journal of Chemical Physics **115**, 6136 (2001).

[179] J. P. Doye, D. J. Wales, and M. A. Miller, The Journal of Chemical Physics **109**, 8143 (1998).

[180] J. Neirotti, F. Calvo, D. L. Freeman, and J. Doll, The Journal of Chemical Physics **112**, 10340 (2000).

[181] F. Calvo, J. Neirotti, D. L. Freeman, and J. Doll, The Journal of Chemical Physics **112**, 10350 (2000).

[182] J. P. Doye and F. Calvo, The Journal of Chemical Physics **116**, 8307 (2002).

[183] C. Predescu, P. A. Frantsuzov, and V. A. Mandelshtam, The Journal of Chemical Physics **122**, 154305 (2005).

[184] J. Doye and D. Wales, Zeitschrift für Physik D Atoms, Molecules and Clusters **40**, 466 (1997).

[185] W. H. Press, B. P. Flannery, S. A. Teukolsky, W. T. Vetterling, et al., *Numerical recipes*, 1989.

[186] E. G. Noya and J. P. Doye, The Journal of Chemical Physics **124**, 104503 (2006).

[187] D. Wales, J. Doye, A. Dullweber, M. Hodges, F. Naumkin, F. Calvo, J. Hernández-Rojas, and T. Middleton, *The cambridge cluster database*, 2001.

[188] B. F. Figgins and B. L. Smith, The Philosophical Magazine: A Journal of Theoretical Experimental and Applied Physics **5**, 186 (1960).

[189] E. R. Dobbs and G. O. Jones, Reports on Progress in Physics **20**, 516 (1957).

[190] J. C. G. Calado and L. A. K. Staveley, Fluid Phase Equilibria **3**, 153 (1979).

[191] G. Albuquerque, M. N. Da Ponte, and L. Staveley, Cryogenics **20**, 416 (1980).

[192] D. R. Sears and H. P. Klug, Chemical Physics **37**, 3002 (1962).

[193] A. Eatwell and B. Smith, Philosophical Magazine **6**, 461 (1961).

[194] A. J. Leadbetter and H. E. Thomas, Transactions of the Faraday Society **61**, 10 (1965).

[195] A. G. Ferreira and L. Q. Lobo, Journal of Chemical Thermodynamics **41**, 809 (2009).

[196] W. Herreman, Cryogenics **20**, 133 (1980).

[197] A. Grosse, Journal of Inorganic and Nuclear Chemistry **27**, 509 (1965).

[198] F. J. Allen and R. Moore, Journal of the American Chemical Society **53**, 2522 (1931).

[199] W. Keesom, J. Mazur, and J. Meihuizen, Physica **2**, 669 (1935).

[200] M. P. Freeman and G. Halsey Jr, The Journal of Physical Chemistry **60**, 1119 (1956).

[201] K. D. Hill, in Aip conference proceedings, Vol. 1552, 1 (AIP, 2013), pp. 198–203.

[202] W. Ramsay and M. W. Travers, Philosophical Transactions of the Royal Society of London. Series A, Containing Papers of a Mathematical or Physical Character **197**, 47 (1901).

[203] G. Kane, The Journal of Chemical Physics **7**, 603 (1939).

[204] F. Paneth and E. Rabinowitsch, Berichte der deutschen chemischen Gesellschaft (A and B Series) **58**, 1138 (1925).

[205] J. Hansen and L.Verlet, Physical Review **184** (1969).

[206] A. J. C. Ladd and L. V. Woodcock, Molecular Physics **36**, 611 (1978).

[207] R. Agrawal and D. A. Kofke, Molecular physics **85**, 23 (1995).

[208] M. A. Barroso and A. L. Ferreira, The Journal of Chemical Physics **116** (2002) 10.1063/1.1464828.

[209] A. Ahmed and R. J. Sadus, The Journal of Chemical Physics **131**, 174504 (2009).

[210] Y. KataoKa and Y. Yamada, Journal of Computer Chemistry, Japan **13**, 257 (2014).

[211] R. Berry and B. Smirnov, Low Temperature Physics **35**, 256 (2009).

[212] F. Guinea, J. H. Rose, J. R. Smith, and J. Ferrante, Applied Physics Letters **44**, 53 (1984).

[213] J. E. Jones, A. E. Ingham, and S. Chapman, Proceedings of the Royal Society of London. Series A, Containing Papers of a Mathematical and Physical Character **107**, 636 (1925).

[214] R. Cotterill, Physica Scripta **18**, 37 (1978).

[215] J. M. Ziman, *Principles of the Theory of Solids*, 2nd ed. (Cambridge University Press, 1972).

[216] J. H. Rose, J. Ferrante, and J. R. Smith, Physical Review Letters **47**, 675 (1981).

[217] J. R. Smith, J. Ferrante, and J. H. Rose, Physical Review B **25**, 1419 (1982).

[218] J. W. Frenken and J. Van der Veen, Physical review letters **54**, 134 (1985).

[219] J. W. Frenken, P. M. Marée, and J. F. van der Veen, Physical Review B **34**, 7506 (1986).

[220] Q. Mei and K. Lu, Progress in Materials Science **52**, 1175 (2007).

[221] A. L. Day, E. T. Allen, and J. P. Iddings, *The isomorphism and thermal properties of the feldspars*, 31 (Carnegie Institution of Washington, 1905).

[222] J. Herman and H. Elsayed-Ali, Physical review letters **69**, 1228 (1992).

[223] N. Ainslie, J. Mackenzie, and D. Turnbull, The Journal of Physical Chemistry **65**, 1718 (1961).

[224] S.-N. Luo, T. J. Ahrens, T. Çağın, A. Strachan, W. A. Goddard III, and D. C. Swift, Physical Review B **68**, 134206 (2003).

[225] S.-N. Luo and T. J. Ahrens, Physics of the Earth and Planetary Interiors **143**, 369 (2004).

[226] J. Bouchet, F. Bottin, G. Jomard, and G. Zérah, Physical Review B - Condensed Matter and Materials Physics **80**, 1 (2009).

[227] C. M. Neal, A. K. Starace, and M. F. Jarrold, Physical Review B **76**, 054113 (2007).

[228] D. Vollath and F. Fischer, Journal of Nanoparticle Research **11**, 1485 (2009).

[229] J. Zhong, Z. Jin, and K. Lu, Journal of Physics: Condensed Matter **13**, 11443 (2001).

[230] K. D. Sattler, *Handbook of nanophysics: nanoparticles and quantum dots* (CRC press, 2016).

[231] S. M. Stishov, Physics-Uspekhi **17**, 625 (1975).

[232] S. Stishov, I. Makarenko, V. Ivanov, and A. Nikolaenko, Physics Letters A **45**, 18 (1973).

[233] M. Lasocka, Physics Letters A **51**, 137 (1975).

[234] J. E. Lennard-Jones and A. Devonshire, Proceedings of the Royal Society of London. Series A. Mathematical and Physical Sciences **169**, 317 (1939).

[235] J. E. Lennard-Jones and A. Devonshire, Proceedings of the Royal Society of London. Series A. Mathematical and Physical Sciences **170**, 464 (1939).

[236] S. M. Stishov, Soviet Physics Uspekhi **31**, 52 (1988).

[237] J. L. Tallon, Physics Letters A **76**, 139 (1980).

[238] J. L. Tallon and W. H. Robinson, Physics Letters A **87**, 365 (1982).

[239] J. L. Tallon, Physics Letters A **87**, 361 (1982).

[240] J. L. Tallon, Nature **342**, 658 (1989).

[241] J. Maddox, Nature **323**, 577 (1986).